ANALYSIS OF POWDER COMPACTION PROCESS THROUGH EQUAL CHANNEL ANGULAR EXTRUSION

A Dissertation

by

ANSHUL KAUSHIK

Submitted to the Office of Graduate Studies of
Texas A&M University
in partial fulfillment of the requirements for the degree of

DOCTOR OF PHILOSOPHY

December 2007

Major Subject: Mechanical Engineering

ANALYSIS OF POWDER COMPACTION PROCESS

THROUGH EQUAL CHANNEL ANGULAR EXTRUSION

A Dissertation

by

ANSHUL KAUSHIK

Submitted to the Office of Graduate Studies of
Texas A&M University
in partial fulfillment of the requirements for the degree of

DOCTOR OF PHILOSOPHY

Approved by:

Chair of Committee,	Arun Srinivasa
Committee Members,	Ibrahim Karaman
	Anastasia Muliana
	Jay R Walton
Head of Department,	Dennis O'Neal

December 2007

Major Subject: Mechanical Engineering

ABSTRACT

Analysis of Powder Compaction Process Through Equal Channel Angular Extrusion. (December 2007)

Anshul Kaushik, B.E., Osmania University, India;

M.S., Texas A&M University, College Station

Chair of Advisory Committee: Dr. Arun Srinivasa

A thermodynamic framework was presented for the development of powder constitutive models. The process of powder compaction through Equal Channel Angular Extrusion (ECAE) at room temperature was modeled using the finite element analysis package ABAQUS. The simulation setup was used to conduct a parametric study involving varying the process parameters of ECAE, aimed at aiding the process design.

Two powder compaction models, the Gurson model and the Duva and Crow model, were used to test their efficacy in modeling this process. The thermodynamic framework was applied to derive the constitutive equations of the Duva and Crow model. Modeling parameters like friction coefficients, interaction conditions were determined by comparing the simulations for solid billet and an empty can with actual experimental runs for loads, shear angle and workpiece

geometry. The simulations using the two powder constitutive models showed no significant difference in the stress in the powder during the extrusion.

The results obtained from the 3-D simulations were also compared to experiments conducted to compact copper powder with a size distribution of 10μm to 45μm. It was found through experiments that the powder does not fully consolidate near the outer corner of the workpiece after the first ECAE pass and the results from the simulations were used to rationalize this phenomenon. Modifications made to the process by applying a back pressure during the simulations resulted in a uniformly compacted powder region.

Further, simulations were carried out by varying the process parameters like the crosshead velocity, the friction coefficient between the walls of the die and the can, can dimensions and material, shape of the can cross section etc and the effect of each of these parameters was quantified by doing a sensitivity analysis.

To

Papa, Ma and Shailey

ACKNOWLEDGEMENTS

I would like to take this opportunity to offer my heartfelt thanks to a number of people without whose help and support this work would never have been possible. I must start with my advisor Dr. Arun Srinivasa, for providing me with an opportunity to work with him. He has always guided me through my work and at the same time given me enough freedom to learn and produce original ideas. Thank you, sir, for being as patient with me as you were.

I would like to thank Dr. Imrahim Karaman for his input throughout this work. Meetings with him gave me an insight into the workings of the process and helped me immensely in the modeling work. I would also like to thank Dr. Anastasia Muliana and Dr. Jay Walton for serving on my committee. I would also like to thank the supercomputing facility at Texas A&M University, where most of the simulations ran.

My parents have provided me with countless opportunities for which I am extremely grateful. The love that my sister and I share in my life is invaluable to me. Nothing I say here can do justice to the continuous and unending support I get from my family. I must also thank a few friends who have been with me through the ups and downs in my life. Thank you very much Purna and Mini.

I would also take this opportunity to thank my lab-mates over the 5 years - Seemant, Nandagopalan, Praveen, Satish and Pritha. My numerous discussions with them helped me think better and analyze problems with a broader prospective.

It gives me immense pleasure to thank the numerous friends who have come in my life at various stages to make it wonderful. Thank you Shruti, Raghu, Saradhi, Suchi, Ritu, Vijay, Neethi, Abhilasha and Anjana. I shall always remember the good times I had with you all.

TABLE OF CONTENTS

CHAPTER Page

CHAPTER Page

LIST OF FIGURES

Page

Page

Page

Page

Page

Page

Page

LIST OF TABLES

Page

CHAPTER I

INTRODUCTION

I.1. Fine-grained materials

The ability to make materials that have the optical mix of mechanical properties has been the focus o large amount of research in the materials community. For example one would like to create materials that combine very high tensile strength with very high ductility. Typically however, such a combination has been elusive if not impossible to achieve. This is because in general these two requirements are mutually contradictory. For example, it is generally known that materials that exhibit high ductility also tend to have low yield strength and vice versa.

Recently there has been intensive research on the possibility of creating nano-crystalline materials. These are materials whose grain sizes are in the 100-200 nm scale. See for example the recent review article by Meyer et al. (2006). It has been observed and theorized that such materials would have ideal combination of high ductility and high yield strength. However, manufacturing such materials in bulk has not been easy.

This dissertation follows the style of International Journal of Plasticity.

Possible approaches to making such fine grained materials include inert gas condensation (Gleiter, 1989), mechanical alloying (Suryanarayana, 2001), electro-deposition (Erb, 1995), High pressure torsion (Zhilyaev et al., 2003) etc.

These processes can be classified into two broad kinds. 1: Starting with nano-grained crystals and compacting/ sintering them into the bulk material, and 2: starting with a coarse grained material and inducing grain subdivision by severe plastic deformation. Both these methods suffer from some fundamental limitations. A typical powder compaction process at room temperature creates porosity and other internal defects which prevent the material from achieving its full strength. On the other hand, compaction at elevated temperatures creates grain coalesces and in many cases results in bimodal grain distribution i.e, islands of large grains size surrounded by much smaller grains. These large grains lower the tensile strength of the material by a significant factor.

Severe Plastic Deformation (SPD) techniques such as HPT typically tend to impart non-uniform deformations throughout the body and it is not possible to create bulk samples with any of these methods. Recently, a new SPD process, Equal channel angular extrusion has emerged as a promising candidate for the creation of bulk nano-structured materials.

I.2. ECAE

Equal Channel Angular Extrusion (ECAE) was developed as a method to produce optimum effects of plastic deformations fine-grained materials (Segal, 1995). It is effectively a method to produce a large amount of shear deformation in a material by passing it around a corner. A typical ECAE die consists of two channels of equal cross section, intersecting at an angle 'Φ' (Segal, 1995) as shown in Figure 1. The work piece is placed in one of the channels and forced to pass into the second channel using a plunger. As the billet passes through, it is severely deformed in shear within a small region at the intersection of the two channels.

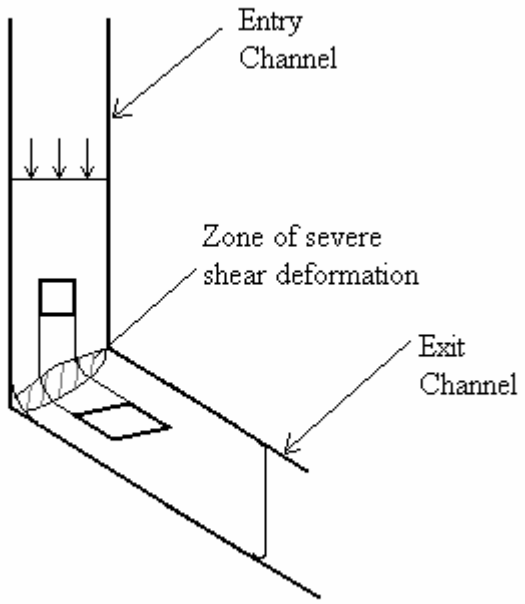

Fig 1. A schematic of the Equal Channel Angular Extrusion (ECAE) process showing the deformation of a square element after the extrusion.

One of the main advantages of ECAE over conventional extrusion is that the cross section of the material undergoing extrusion remains the same after the process, thus enabling repeated extrusions of the same work piece to obtain larger accumulated plastic strains (Zhu and Lowe, 2000). Furthermore, the work piece experiences a near-uniform shear strain throughout. Also, ECAE requires lower loads than conventional extrusion to achieve the same amount of plastic deformation as shown by Segal in his work in 1995. The mechanical properties and microstructure of several materials undergoing ECAE have been extensively studied and thoroughly summarized in a recent review by Valiev and Langdon (2006).

The original ECAE process as envisaged by Segal was focused on the deformation of the bulk materials. However, recently, this process has been shown as an effective method to consolidate metallic powders (Parasiris et al., 2000; Matsuki et al., 2000; Kim et al., 2003; Robertson et al., 2003; Haouaoui et al., 2004; Karaman et al., 2004; Senkov et al., 2004; Senkov et al., 2005; Xia and Wu, 2005; Karaman et al., 2007) and hence shows promise as a method to produce ultra fine grained materials in bulk. In this process, the billet is replaced by a can filled with powder as shown schematically in Figure 2, which is passed through the ECAE die to undergo compaction and shear in one step. This process has been applied to the compaction of copper powders to create nano-grained copper powder by Karaman et al (2007). Their results show that it is possible to create nano-grained copper with

grain sizes in the range of 50-300 nm by compacting nano-sized powder (in the 100-150 nm range). The extruded bulk material created through nano powders showed high yield strength of upto 800 MPa through 4 passes of ECAE when compared to annealed copper which shows yield strength of upto 200 MPa. Compacted microcrystalline powder (size in the 75micron range) showed increased yield strengths of upto 500 MPa.

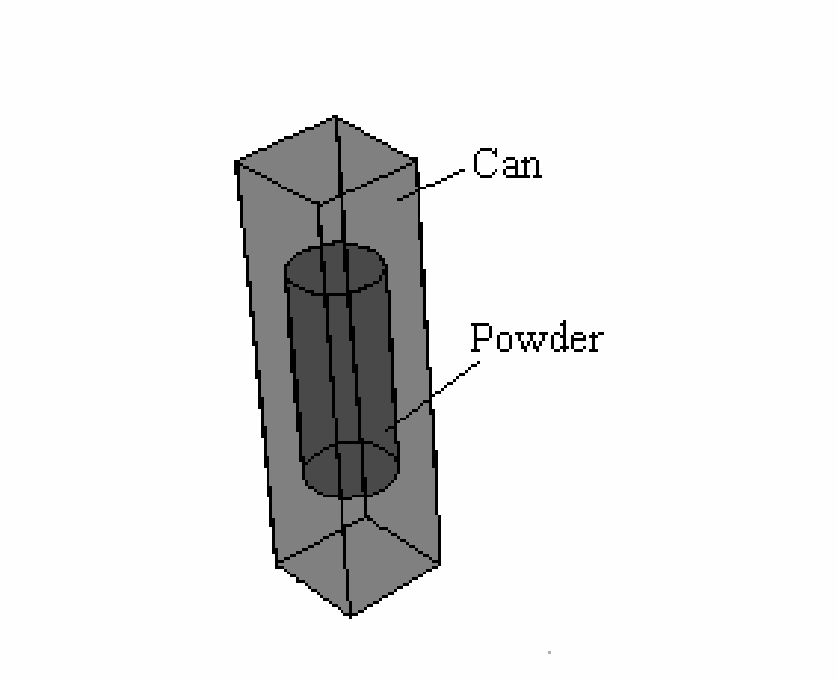

Fig 2. Schematic showing the prepared ECAE can with the powder.

While these preliminary experiments have shown the potential of ECAE as a viable method for creating nano-cryatalline materials, not much is understood about the process by which the compaction occurs. Due to this, it has been extremely hard to control the deformation process in order to achieve grain morphologies in a

repeatable manner. For example, while generally recognized that ECAE gives uniform shear strains, it has been found that the compaction is not uniform throughout the cross section. Given the fact that the compaction is strongly affected by normal forces, these observations suggest that the normal stresses are not necessarily uniform in the cross section and this in turn has a significant effect on the degree of compaction. It is typically assumed that the material of the can should closely match that of the powder in powder to get increased compaction. However no studies have been done on the influence of the can material on the compaction process. Given the fact that the can material is prohibitively expensive, one would like to optimize the dimensions of the can in order to lower the cost of the process while yielding uniform compaction at the same time. Hence it is critical to design the compaction process effectively, and to study the impact of various parameters such as the rate of displacement of the press, friction, back pressure etc. This design process can be greatly assisted by the use of a simulation tool which could predict the mechanical response of the powder material undergoing ECAE compaction. This is the focus of this dissertation.

I.3. Literature review

I.3.1. Powder compaction through ECAE

The process of powder compaction through ECAE has been pioneered and extensively used at Texas A & M to consolidate powders since 1995. Work on compaction of Al 6061 powder was carried out by Pearson (1997) and Zapata (1998) in their respective master's thesis works at Texas A & M. A study of extrusion of WC blended with Co at high temperatures was done by Parasiris et al., (2000) and Parasiris and Hartwig, (2000). Al 6061 powder was extruded through a 90 degree die under warm conditions to achieve full density and tensile strength comparable to that of wrought material by Hartwig et al., (2001). Other powders and powder mixtures that have been consolidated by using this process are Nanostructured Titanium Silicide at high temperatures (Kaculi et al. 2003), Cu blended with Ag, Sn-8Cu blended with Al2O3 and SiO2 (Hartwig et al., 2003), microcrystalline SS and amorphous Cu and Zr based alloys (Robertson et al. 2003 and Karaman et al. 2004). A detailed study of compaction of micro and nano sized copper powder with different can materials undergoing multiple passes was done by Haouaoui et al (2004) and more recently in Karaman et al. (2007).

Xia and Wu (2005) studied the compaction of pure Aluminum through ECAE with the application of back pressure. Matsuki et al. (2000) studied the compaction of Aluminum powder alloys while Senkov et al. (2004) studied the compaction of semi amorphous Aluminum Alloys at room temperatures.

Nagasekhar and Tick-Hon (2004) studied compaction of Magnesium Boride (MgB_2) powder in circular tubes extruded at temperatures ranging from room temperatures to 500 C. Kim et al. (2003) studied the compaction of copper and Aluminum alloys at room temperature. Most of these studies focus on achievement of full densification, microstructure development and mechanical property enhancement.

I.3.2. Powder compaction models

In recent years, keeping in pace with the development of powder forming technology, many powder compaction models and consolidation mechanisms have been proposed to suitably model the various methods like sintering, Hot isostatic pressing, extrusion and cladding processes (Gurson, 1977; Duva and Crow 1992; Wilkinson and Ashby, 1975; Tvergaard, 1981; Carroll, 1986; Kim and Carroll, 1987; Kim and Suh, 1990; Delo and Piehler, 1999).

Subramanian and Sofronis (2002) developed a constitutive potential to model the compaction of cylindrical powders during pressure sintering. This potential was developed for particles made of a material undergoing power-law creep with non-linearly evolving boundaries and undergoing interparticle mass diffusion.

Bakhshiani et al. (2002) developed a model based on large strain plasticity for powder materials. Perez-Foguet et al (2003) developed a density dependent plasticity model for hyperelastic-plastic materials considering the large deformation behavior of the powder.

Most of the powder compaction models describe the densification of the powders in 2 stages. Stage 1 where the powder particles share small areas of contact with their neighbors and the voids are connected. In this stage, as compressive load is applied, the particles move relative to each other and their areas of contact increase with load leading to stage 2 where the voids are isolated and surrounded by the solid material. These models include the influence of hydrostatic pressure on the yield surface and use the relative density as a hardening parameter.

Typically these models specially the ones with large deformation formulation focus mainly on the behavior of compaction for materials that are already fairly compacted with relative densities in the range of 0.8. There are very few models that look into the whole range of compaction starting with fairly low relative density. One such model that deals with powder compaction for powders starting from stage 1 is the Duva and Crow model, see for example Carmai and Dunne (2004) and Carmai and Dunne (2005). Another commonly used model for studying the densification behavior of powders is the Gurson model. Though the actual working range of the Gurson model is only above relative densities of over 0.9, it will be used in this work and the results will be compared with the Duva and Crow model in order to evaluate the differences in the predicted values of those properties that are of relevance to this work.

I.3.3. ECAE modeling

Modeling the processing of bulk metal and polymers through ECAE has been carried out in detail in the last decade. A theoretical estimate of the shear strain developed during an ECAE pass was made using the slip-line field theory by Segal et al in 1981. In the same work, the effect of friction on the deformation pattern in ECAE was investigated. More recently, Iwahashi et al. (1997) proposed a new formulation to calculate the shear strain during ECAE, which considered the separation of the work piece from the die at the outer corner.

Yun (1996) used commercial finite element codes to numerically model ECAE. His work focused on perfectly plastic and work hardening materials and showed the relevance and efficacy of the finite element method to model the ECAE process.

Finite Element simulation of the ECAE process was first published in a journal by Prangnell (1997). This paper presented the extent of strains that took place in the specimen during ECAE for various friction values and die angles. It showed that the deformation occurring was homogeneous for most of the billet but was inhomogeneous at the ends, and that this inhomogeneity depends on the die angle.

Sue et al. (1999) worked on the behavior of Polycarbonate plate undergoing ECAE. They created a 2-D finite element model for non-linear behavior for the polymer material. Their models correlated well with the experimental findings. The

concluded that for the ECAE to work well on the polymers, the extrusion should be done at temperatures just below the glass transition temperature of the polymer material.

Bowen et al. (2000) studied the deformation behavior during ECAE through finite element simulations and experiments. Their results included the strain predictions for different points along a section in the billet. They showed that the effective strain is lesser at the outer corner of the extrusion and maximum at the inner. They also included the effects of friction and multiple passes on the deformation behavior.

Kim et al. (2000) showed, through simulations, that the formation of corner gap during ECAE depends on the material model used. The gap is larger for a strain hardening material than for a perfectly plastic material. The also showed that a bigger corner gap reduces the strain in the outer part of the billet and also decreases the average strain. In a later work Kim et al. (2001) the authors attributed the lower strains obtained in the outer section to the higher flow rate of the in the outer part compared to the inner part. They also split the load displacement curve during ECAE into 5 parts and attributed the major cause of the load to the stages that cause the load.

Liu et al. (2000) simulated the results for changing channel extrusion. Their results showed that the hydrostatic pressures and true strains obtained using the changing channel extrusion, where the die size increased at each bend before finally

going to the original inlet size, were all higher than those obtained using a constant channel extrusion.

Semiatin and DeLo (2000) used a sliding bottom die in their simulations and compared the results to a stationary bottom. They showed that the sliding bottom arrangement, along with back pressure prevented the separation of the bottom of the billet from the die. They also commented on the non-uniform strain at the ends and along the outer section of the billet. Their simulations showed that the stresses are mostly compressive in the shear zone. They also predicted the number of passes a billet can undergo before fracture of top layers. In another work Semiatin et al. (2000) which focused on ECAE experiments with hard to work materials like pure Titanium, 4340 steel and Ti-6Al-4V, the authors also presented simulations carried out for these materials using non-isothermal conditions for hot extrusions.

Srinivasan (2001) carried out simulations for various die angles and outer fillet radii. The magnitude of maximum strain depends on the die angle and the fillet radius, which also influences the strain distribution. Multiple passes will increase the strain difference among different regions, thus limiting the use of having larger number of multiple passes at larger channel angle instead of lesser passes at smaller angles. He also showed that the fillet radius contributes to bending of the outer end of the workpiece.

Stoica and Liaw (2001) presented a survey of work done on modeling and experimentation in ECAE. They also attempted to categorize the deformation that the material undergoes during the extrusion. Suh et al. (2001) showed through

simulations that the increase in fillet on the outer corner reduces the effective strain in the outer section of the billet.

Kim et al. (2002) worked on ECAE simulations using hardening dependent on both the strain and the strain rate. Their results included the effect of the mesh size on the simulation results. They showed that a coarser mesh size incorrectly predicts the gaps between the die and the workpiece at the corner and the exit section. The strain rate decreases with the Die angle and with the fillet radius of the outer corner. The distribution of the strain rate along the section in the shear band was documented.

Luis et al. (2002) simulated the ECAE and the Equal Channel Angular Drawing (ECAD) processes for various die angles, fillet radii and friction conditions, and compared these simulation results with their experimental results. They documented the plastic strains at various points along the billet for both ECAE and ECAD. They also determined, experimentally, the hardness along various points which increased with the number of passes. They showed that the strains obtained through ECAE are higher than those obtained through ECAD. In another work, Perez et al. (2003a) they confirmed that ECAE is more suitable to obtain finer grain structures than ECAD through experiments on Aluminum. The authors used similar simulations to study the response of Al-Mn alloys which is documented in Perez et al. (2003b). Later, Luis-Perez et al (2004) conducted study to determine the plastic strains obtained in ECAE using various die angle and

friction conditions. They concluded that higher friction values lead to better filling of the corners and higher deformation values, but require higher loads.

Rosochowski and Olejnik (2002) showed through experiments and simulations, the effect of a second turn in ECAE in the same die instead of the usual process of removing the die and passing it through the die again. Their findings showed that a second turn caused better filling of the corners, doubled the plastic strain and more than doubled the loads. They concluded that for effective use of the second bend, the offset distance should be at least 1.5 times the channel thickness and to avoid stress concentration during the process, a fillet radius of at least 0.2 times the channel thickness should be applied at the corners.

Baik et al. (2003) used a dislocation based hardening model, which accounted for dislocation density evolution and variation of the average cell size, for the material (Aluminum) undergoing ECAE. Their results showed that there is considerable increase in hardening between the 1^{st} and the 2^{nd} passes but not for the 3^{rd} and subsequent passes. They showed that a finer grain structure forms in the bulk of the material than the periphery and this difference decreases with increase in number of passes.

Beyerlein et al (2003) used a Visco-plastic self consistent material model, which treats each grain, which has a distinct orientation and volume fraction, as an ellipsoidal visco-plastic inclusion interacting with the effective medium represented by the average response of all the grains. Using this model, the authors predicted

the shear stress, the average grain size, the number of splits, and the grain size distribution for different paths and number of passes.

Oh and Kang (2003) carried out simulations to study the effects of friction, material properties and back pressure. Their results showed that high strength materials give more uniform distribution of strain than low strength materials, but require higher power for the process. The tensile stresses were higher with friction.

Pei et al (2003) studied the variation of temperature along the workpiece during ECAE through simulations and compared the results to experiments. They used the Johnson-Cook model in the simulations. Their simulations showed that high temperatures are obtained in the shear zone. They also showed that both the material and pressing speed have an effect on the temperature rise.

Yang and Lee (2003) created a 2-D ECAE model to study the effect of channel angles, the corner radius and number of passes. They calculated the strains along the section of the billet for various cases. They correctly predicted that to carry out simulations of multi pass ECAE processes which include 90 degree rotation of the billet about its axis, a 3-D simulation would be required.

Li et al. (2004) carried out Finite element simulations for perfectly plastic and strain hardening materials undergoing ECAE to study the formation of plastic zone and loads for variety of geometric parameters. They predicted the deformation in the billet head for different corner fillet radii. Though a lot of the results presented in this work were already presented in previous works, some significant output of this paper was the study of development of the plastic shear zone for

different corner fillet radii and material properties. They showed that low values of friction had little effect on the development of the PDZ. Regarding the work load, the authors concluded that larger fillet radii required lower loads.

Nagasekhar et al. (2004) used finite element simulations to find optimal tool angles to carry out ECAE. They showed that tool angle of 0 degrees was closest to simple shear but produced larger strain distribution and severe stress concentration at the outer corner. They also concluded that tool angles of 20 and 28 degrees gave higher non-uniformity in strains than 10 degrees tool angle. Thus they concluded that 10 degree tool angle is optimal for producing uniform shears and least dead zone.

In spite of the amount of experimental work done on powder compaction through ECAE, the published literature on modeling of the powder compaction process through ECAE is very little. Finite Element analysis of metallic powders undergoing ECAE has been carried out in previous work by Yoon and Kim (2006). These 2-D simulations, without a can, are not adequate to capture the true nature of a powder compaction through ECAE because the can has a huge effect on the mechanics of compaction. Through their simulations, they showed that that hydrostatic pressure is first developed in the entry channel which assists the compaction and then simple shear is generated as the sample passes through the channel.

It is clear that to accurately model the powder compaction process through ECAE, it is necessary to select a powder consolidation model which predicts the

response of the powder under hydrostatic loads with shear stresses. The next section gives a brief on the current powder compaction models available and the ones that were selected in this work.

I.4. Objective and scope

I.4.1. Objective

The objective of this dissertation is to model the powder compaction process through ECAE using a large deformation viscoplastic formulation, the resulting differential equations being solved by the finite element method. The resulting simulation will be used to model the influence of various parameters for example friction, back pressure, rate of extrusion, can material, Dimensions of the can, etc on the eventual compaction of the powder. Furthermore, different constitutive models will be compared for the purpose of evaluating their relative efficacy in modeling the compaction process.

I.4.2. Scope

Following the work of Duva and Crow (1992) and Gurson (1977), we have specialized two broadly used models for the purpose of simulating the powder compaction process through ECAE. The software package ABAQUS will be used as the tool to carry out the finite element solution for this problem. For this purpose, the user subroutines VUMATs are developed for incorporating the constitutive

models for the powder in 2-D and 3-D. The parameters like the interaction conditions were validated through comparisons of the simulation results with the experiments carried out by Karaman and co-workers at Texas A&M.

A comparison of the two powder models will be carried out through two dimensional simulations. A systematic study of the mesh dependence will be carried out in 2-D. A mass scaling procedure was used in the simulations and the result of this mass scaling on the response of the materials will be investigated. The effect of multiple passes on the densification behavior will be studied through 2-D simulations.

Once the optimal simulation conditions have been determined, these conditions will be used in the full scale 3-D simulation. These 3-D finite element simulations are used to make a parametric study of the effect of the following design variables to determine the optimal extrusion conditions

1. Friction: Friction coefficient between the die and the can is determined to be an important parameter in the compaction behavior. We assume that there is dry friction between the can and the die and will study the effect of the dry friction coefficient ranging from 0 to 0.08.
2. Back Pressure: One of the interesting effects in ECAE is the pressurization of the workpiece at the exit channel. This phenomenon will be studied to determine its effect on both the uniformity and extent of compaction.
3. Dimensions of the can: We study the effect of overall length of the can, the thickness of the lateral walls and the thickness of the base. The first of these

plays an important role the volume of the powder that can be extruded. The second pertains to both increasing the cross sectional dimension of the extruded powder as well as lowering the amount of can material needed. The third pertains to role of the can in constraining the powder at the exit end.

4. Can material: The effect of using Copper as the can material versus using nickel as the can material will be studied.
5. Extrusion rate or speed of extrusion: We study the effect of extrusion rate on both the amount of plastic deformation that was obtained as well as the amount of compaction that was obtained.
6. Finally the effect of a can of circular cross section vs. a square cross section was studied.

I.5. Outline of the dissertation

In chapter II, we develop the constitutive behavior of the powder material, first by using classical solutions for porous media and then go on to develop the model using a thermodynamic framework.

In chapter III, the implementation of the powder model developed in chapter II for use with ABAQUS/ explicit using the user subroutines VUMATs is explained. This implementation is done using a large deformation formulation and uses an Euler integration scheme. The results for validation runs done over a single element to compare the two powder models are presented in this chapter.

In chapter IV, the other parameters which need to be modeled in order to complete the simulations like the constitutive model for the can, the interaction conditions between the can and the die, back pressure etc are discussed. Using these simulation conditions, the interaction conditions are found by comparing the simulations for a bulk Copper billet with experimental results. The geometric features of the extruded can and loads required to extrude the billet are compared to determine the friction coefficient. Comparisons are also made for the simulations for an empty can extruded through ECAE.

The results obtained from the 2-D and 3-D simulations are presented in chapter V. The results for 2-D simulations include the comparison of the two powder models used in this work, the effect of mesh density and mass scaling on the results obtained from the simulations. 3-D simulation results include comparisons with the experimental runs done at Texas A & M University. The effects of varying the parameters like friction, back pressure, dimensions of the can, can material, crosshead velocity and shape of the can are presented in this chapter.

CHAPTER II

DEVELOPMENT OF A THERMODYNAMICALLY CONSISTENT MODEL FOR THE POWDER COMPACTION PROCESS

Consider a body B occupying a reference configuration K_0. A typical particle in the body occupies $\underset{\sim}{X}$ in K_0. As the body is deformed, let its current configuration be K_t and the location of the particle which was at $\underset{\sim}{X}$ is now at $\underset{\sim}{x}$. As usually used in Continuum mechanics, we define the mapping $\underset{\sim}{\chi}$ as

$$\underset{\sim}{x} = \underset{\sim}{\chi}(\underset{\sim}{X}, t) \tag{2.1}$$

and the deformation gradient through

$$\underset{\sim}{F} = \frac{d\underset{\sim}{\chi}}{d\underset{\sim}{X}} \tag{2.2}$$

The velocity of the particle is denoted by $\underset{\sim}{v}$ and is defined as

$$\underset{\sim}{v} = \frac{d\underset{\sim}{\chi}}{dt} \tag{2.3}$$

The gradient of the velocity $\underset{\sim}{v}$ wrt the current coordinates $\underset{\sim}{x}$ is denoted by $\underset{\sim}{L}$ and let

$$\underset{\sim}{D} = \frac{1}{2}(\underset{\sim}{L} + \underset{\sim}{L}^T) \tag{2.4}$$

be the symmetric part of the velocity gradient, also referred to as rate of deformation tensor.

Let $\underset{\sim}{\sigma}$ be the Cauchy stress tensor. The equations of motion of the system in component form are given by

$$\rho \dot{v}_i = \sigma_{ij,j} \tag{2.5}$$

where ρ is the current density of the material and the superposed dot is the material time derivative. For the materials and processes under consideration, the inertial terms in the equations of motion are generally negligible and so we neglect them in equation (2.5).

Furthermore, since the material under consideration is a porous material we would like to introduce the notion of the relative density of the porous material. In order to do this, we take ρ_r to be the density of the fully compacted material (i.e, a material without pores) when it is in a stress free state. Let ρ_0 be the density of the material at time t_0. Then the relative density of the material which will be denoted by RD in this work is defined by

$$RD = \frac{\rho}{\rho_r} \tag{2.6}$$

By using the conservation of mass, and assuming that there is no self diffusion, we can show that

$$RD = \frac{1}{J}\frac{\rho_0}{\rho_r} \tag{2.7}$$

where $J = \det(\underset{\sim}{F})$.

In this chapter we discuss the development of a thermodynamically consistent model for the compaction of powders, starting with the classical work done on porous media for nonlinearly viscous materials and going on to the development of the Duva and Crow model.

As a motivation, we consider the problem of a sphere, made of a nonlinearly viscous material with a hole in the center, under hydrostatic pressure, as shown in Figure 3 is solved first followed by the development of a model involving deviatoric stresses in the material. This serves as a simple test case and illustrates the central features of the subsequent models that will be developed later.

II.1. Solution to the sphere with a hole made of an exponentially creeping material under hydrostatic pressure

The solution of densification of a sphere with a void made of an exponentially creeping material was first presented by Wilkinson and Ashby (1975). Consider a spherical cell made up of an isotropic creeping material with a spherical inclusion as shown in Figure 3. Considering spherical symmetry, we shall assume a solution of the form $\underset{\sim}{v} = v_r \underset{\sim}{e}_r$ and hence the only nonzero components of the velocity gradient will be L_{rr} and $L_{\theta\theta}$. Neglecting inertial and body forces, the problem may be summarized by the following equations setup in spherical coordinates.

a) Equilibrium

$$\frac{d\sigma_r}{dr}+\frac{2}{r}\left(\sigma_r-\sigma_\theta\right)=0 \tag{2.8}$$

b) Compatibility

$$\frac{d}{dr}(rL_{\theta\theta})=L_{rr} \tag{2.9}$$

c) Incompressibility of matrix material

$$L_{rr}=-2L_{\theta\theta} \tag{2.10}$$

d) Boundary conditions

$$\begin{aligned}\sigma_r\left(a\right)&=-P_i\\ \sigma_r\left(b\right)&=-P_e\end{aligned} \tag{2.11}$$

e) Constitutive equation

$$L_{rr}=SA(\left|\sigma_r-\sigma_\theta\right|)^n \tag{2.12}$$

where σ is the cauchy stress, *A* and *n* are material constants and S is the sign of the applied stress, positive in tension and negative in compression..

Considering a cell of inner radius *a* and outer radius *b*, the relative density is given by

$$RD=1-\left(\frac{a^3}{b^3}\right) \tag{2.13}$$

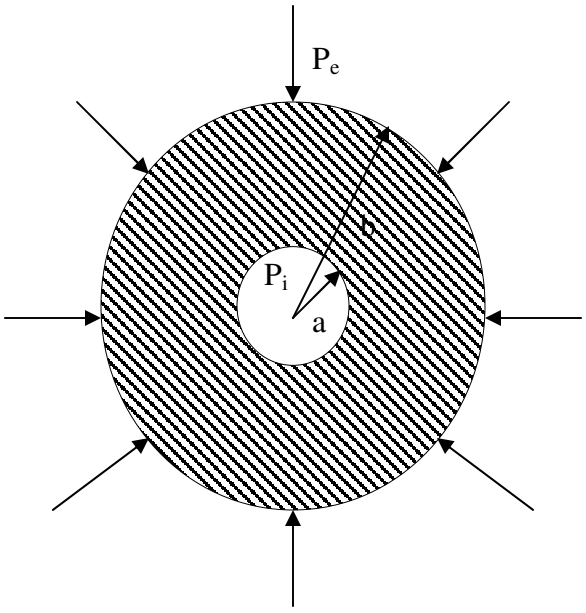

Fig 3. A unit cell for a porous material made of a creeping material (shaded region) with external radius b and an inclusion of radius a. External pressure P_e and internal pressure P_i is applied to the walls of the cell.

Also it should be seen that due to spherical symmetry, $L_{\theta\theta}(r)$ is defined as

$$L_{\theta\theta}(r) = \frac{\dot{r}}{r}$$

The form for the velocity gradient can be obtained by substituting (2.10) into (2.9) and integrating. This yields the form

$$L_{\theta\theta} = -\frac{L_{rr}}{2} = \frac{K}{r^3} \tag{2.14}$$

where K is to be evaluated. Substituting this form into the constitutive equation (2.12) and applying the result to the equilibrium equation (2.8), we obtain

$$d\sigma_r = -\frac{2S}{r}\left(-\frac{2K}{SAr^3}\right)^{1/n} dr \tag{2.15}$$

integrating this in the limit from *a* to *b* and solving for *K* gives

$$K = -\frac{SA}{2}\frac{(ab)^3}{\left(b^{3/n} - a^{3/n}\right)^n}\left(\frac{3}{2}\frac{|\Delta P|}{n}\right)^n \tag{2.16}$$

Now $R\dot{D}$ can be evaluated by differentiating (2.13) to obtain

$$R\dot{D} = 3\frac{a^3}{b^3}\left(\frac{\dot{b}}{b} - \frac{\dot{a}}{a}\right) \tag{2.17}$$

Now we know that $\dot{b}/b = \dot{\varepsilon}_\theta(b)$ and $\dot{a}/a = \dot{\varepsilon}_\theta(a)$. Substituting the value of K from (2.16) into (2.14) to evaluate $L_{\theta\theta}(a)$ and $L_{\theta\theta}(b)$ and substituting in (2.17) to obtain $R\dot{D}$ as

$$R\dot{D} = \frac{3}{2}SA\frac{RD(1-RD)}{\left[1-(1-RD)^{1/n}\right]^n}\left(\frac{3}{2}\frac{|\Delta P|}{n}\right)^n \tag{2.18}$$

The densification rate suggested by the solution to this problem has been found to compare favorably with experimental results by Wilkinson and Ashby in 1975. The densification rate given by (2.18) is used as a benchmark in more elaborate models that include the effects of deviatoric stress in the densification process.

II.2. Model including the effects of deviatoric stress on densification

Cocks (1989) developed a general lower bound expression for the strain rate potential of a porous body undergoing an assumed deformation rate field. The work assumed the material to be a non-linearly creeping material. The analysis was

carried out for one of the unit cells i.e., a sphere of unit volume with a spherical void with volume equivalent to the volume fraction of the voids in the body as shown in Figure 4.

The development assumed the base material of the material matrix to have a constitutive behavior given by the expression

$$L_{ij} = \frac{\partial \phi}{\partial \sigma_{ij}} \tag{2.19}$$

where ϕ is defined through

$$\phi = \frac{1}{n+1} \dot{\varepsilon}_0 \sigma_0 \left(\frac{\sigma_e}{\sigma_0} \right)^{n+1} \tag{2.20}$$

and $\dot{\varepsilon}_0$ and σ_0 are material constants.

A global strain rate potential for the porous body Φ was developed, which gave the volume average of the potentials for each microscopic element in the matrix. The stresses Σ_{ij} applied to the porous material and the strain rates developed $\dot{E}_{ij}$ as a result of the stresses are related through the expression

$$\dot{E}_{ij} = \frac{\partial \Phi}{\partial \Sigma_{ij}} \tag{2.21}$$

where Φ is given by the relation

$$\Phi = \frac{\dot{\varepsilon}_0 \sigma_0}{n+1} \left(\frac{S_{cocks}}{\sigma_0} \right)^{n+1} \tag{2.22}$$

and S_{cocks} is the global equivalent stress.

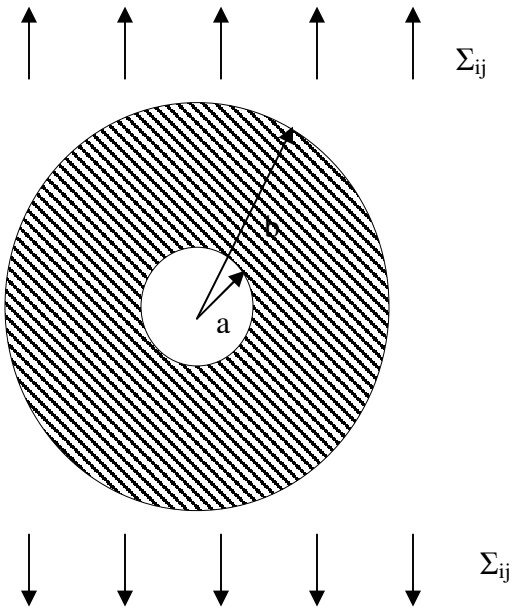

Fig 4. A unit cell for a porous material made of a creeping material (shaded region) with external radius b and an inclusion of radius a. An external stress field Σ_{ij} is applied to the unit cell which results in a strain rate field of $\dot{E}_{ij}$.

Using the convexity of the strain rate potential ϕ and (2.20), the lower bound of the global strain rate potential Φ was obtained and from this result, the global equivalent stress for the porous body was developed. In our notation, the global equivalent stress is given as

$$S_{cocks}^2 = \frac{\left(1+\frac{2}{3}(1-RD)\right)\sigma_e^2 + \left(\frac{9}{4}\frac{2n}{n+1}\frac{1-RD}{2-RD}\right)\sigma_m^2}{RD^{2n/(n+1)}} \qquad (2.23)$$

It was observed that for pure hydrostatic loads, the densification rates given by the strain rate potential (2.22) did not compare well with those given by (2.18).

II.3. Duva and Crow model

Duva and Crow (1992) took the form of the strain rate potential given in (2.22) and developed the strain rate potential which compared well with (2.18) in the hydrostatic limit and took the form of (2.23) for the effective stress. The equivalent strain rate potential proposed by Duva and Crow is given by the expression

$$\phi = \frac{\dot{\varepsilon}_0 \sigma_0}{n+1}\left(\frac{S_{DC}}{\sigma_0}\right)^{n+1} \tag{2.24}$$

where

$$S_{DC}^2 = \frac{\left(1+2/3(1-RD)\right)}{RD^{2n/(n+1)}}\sigma_e^2 + \left(\frac{3}{2n}\right)^2\left(\frac{n(1-RD)}{(1-(1-RD)^{1/n})^n}\right)^{2/(n+1)}\sigma_m^2 \tag{2.25}$$

which we will write in a compact notation as

$$S_{DC}{}^2 = a\sigma_e^2 + b\sigma_m^2 \tag{2.26}$$

where

$$a = \frac{1+(2/3)(1-RD)}{RD^{2n/(n+1)}} \tag{2.27}$$

and

$$b = \left(\frac{3}{2n}\right)^2\left(\frac{n(1-RD)}{(1-(1-RD)^{1/n})^n}\right)^{2/(n+1)} \tag{2.28}$$

The plastic strain rate is defined through

$$\underset{\sim}{D}_P = \frac{\partial \phi}{\partial \underset{\sim}{\sigma}} = AS_{DC}^{n-1}\left(\frac{3}{2}a\underset{\sim}{\tau} + \frac{1}{3}b\sigma_m \underset{\sim}{I}\right) \tag{2.29}$$

The model introduces the relative density dependent parameters *a* and *b* so that the effect of pressure on the measure of yield stress vanishes when the powder is fully consolidated. The variation of *a* and *b* with the relative density is shown in the Figure 5.

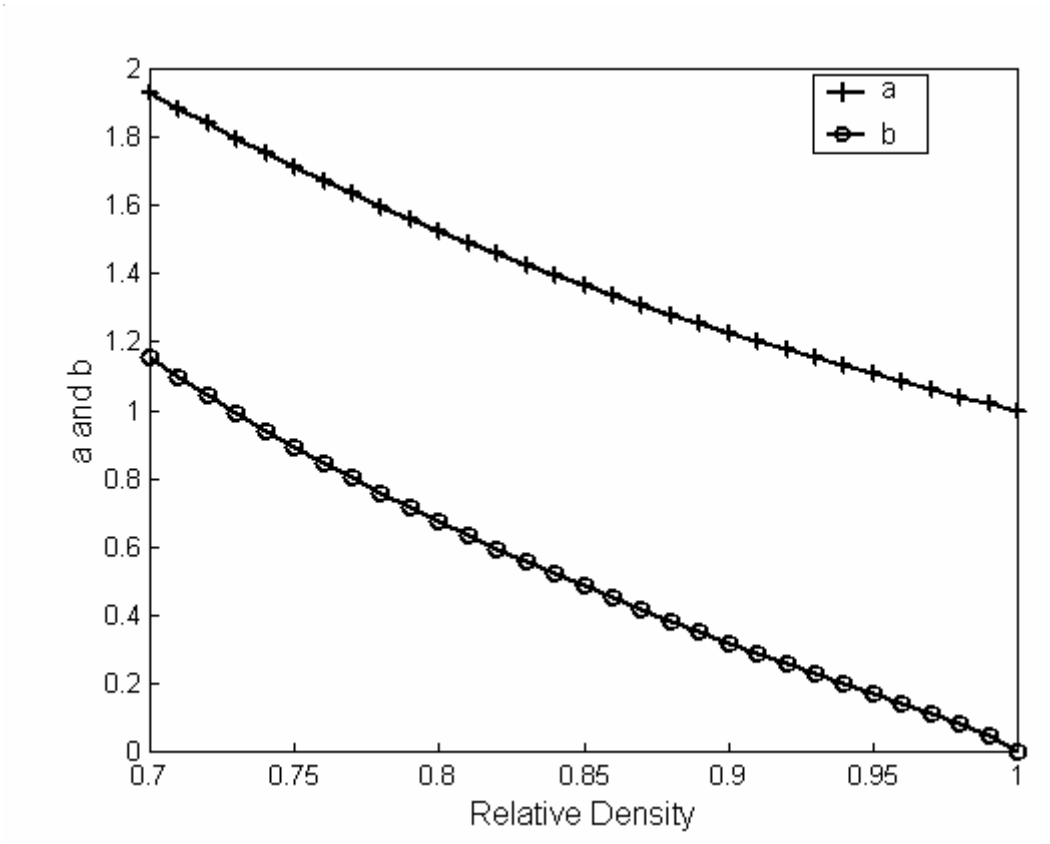

Fig 5. Variation of variables *a* and *b* with relative density. It can be noted that *a* goes to 1 and *b* goes to 0 as relative density goes to 1 giving the Von Mises criterion.

II.4. Development of the constitutive model within the thermodynamic framework

The key point to be noted is that these models are not based on thermodynamic framework and that they do not consider elasticity. We now turn our attention to a thermodynamically consistent framework for this model. The starting point for such a thermodynamic framework is the reduced energy dissipation relation (Truesdell and Noll, 1992) which takes the form

$$\underset{\sim}{\sigma} \cdot \underset{\sim}{D} - \rho\dot{\psi} = \xi \geq 0 \tag{2.30}$$

where, ψ is the Helmholtz potential of the body and ξ is the rate of dissipation. The above equation represents a statement of the second law of thermodynamics for isothermal processes and states that the difference between the stress power and the rate of energy storage per unit mass is dissipated as heat. Conventionally, this equation has been used to restrict the values of constitutive parameters once the constitutive equations for the stress have been chosen. However, Rajagopal and Srinivasa (2005) have shown that it is possible to use this equation to restrict classes of processes given constitutive equations for the Helmholtz potential and the rate of dissipation. Specifically, these authors suggest that materials are not only characterized by the way in which they store energy (i.e, by the form of Helmholtz potential) but also by the possible dissipation mechanisms. Furthermore, they suggest that the material responds in such a way as to maximize the rate of dissipation subject to the requirement that (2.30) be met. In this work, we follow this approach a thermodynamically consistent framework for models that are

similar to the Duva and Crow or the Gurson models. Based on the assumption that the elastic deformations of the material are in the small strain range, we assume that the stored energy ψ is of the form,

$$\psi = \frac{1}{2E}\left\{(1+\upsilon)\sigma_{ij}^{*}\sigma_{ij}^{*} - \upsilon\sigma_{kk}^{*}\sigma_{ll}^{*}\right\} \tag{2.31}$$

where $\underset{\sim}{\sigma}^{*} = \underset{\sim}{R}^{T}\underset{\sim}{\sigma}\underset{\sim}{R}$ is a rotated stress tensor. Now differentiating (2.31) to obtain $\dot{\psi}$, we get

$$\dot{\psi} = \frac{1}{E}\left\{(1+\upsilon)\dot{\sigma}_{ij}^{*} - \upsilon\dot{\sigma}_{kk}^{*}\delta_{ij}\right\}\sigma_{ij}^{*} \tag{2.32}$$

Now we can evaluate $\dot{\sigma}_{ij}^{*}$ and obtain

$$\dot{\underset{\sim}{\sigma}}^{*} = \dot{\underset{\sim}{R}}^{T}\underset{\sim}{\sigma}\underset{\sim}{R} + \underset{\sim}{R}^{T}\dot{\underset{\sim}{\sigma}}\underset{\sim}{R} + \underset{\sim}{R}^{T}\underset{\sim}{\sigma}\dot{\underset{\sim}{R}} \tag{2.33}$$

which on further evaluation gives

$$\dot{\underset{\sim}{\sigma}}^{*} = -\underset{\sim}{\Omega}\underset{\sim}{\sigma}^{*} + \underset{\sim}{R}^{T}\dot{\underset{\sim}{\sigma}}\underset{\sim}{R} + \underset{\sim}{\sigma}^{*}\underset{\sim}{\Omega} \tag{2.34}$$

where $\underset{\sim}{\Omega}$ is the spin tensor defined through $\underset{\sim}{\Omega} = \dot{\underset{\sim}{R}}\underset{\sim}{R}^{T}$ where $\underset{\sim}{R}$ is the rigid body rotation in the polar decomposition of the deformation gradient tensor $\underset{\sim}{F}$. Substituting (2.34) into (2.32) and back substituting it into (2.30) we get,

$$\sigma\cdot\left[\underset{\sim}{D} - \frac{\rho}{E}\left\{(1+\upsilon)\overset{\nabla}{\sigma} - \upsilon tr(\overset{\nabla}{\sigma})\underset{\sim}{I}\right\}\right] = \xi \tag{2.35}$$

where $\overset{\nabla}{\sigma}$ is given by $\overset{\nabla}{\sigma} = \dot{\sigma} - \underset{\sim}{\Omega}\cdot\underset{\sim}{\sigma} + \underset{\sim}{\sigma}\cdot\underset{\sim}{\Omega}$.

If we define a tensor D_p as

$$\underset{\sim}{D}_{P} = \underset{\sim}{D} - \frac{\rho}{E}\left\{(1+\upsilon)\overset{\nabla}{\sigma} - \upsilon tr(\overset{\nabla}{\sigma})\underset{\sim}{I}\right\} \tag{2.36}$$

then we can rewrite (2.35) as

$$\underset{\sim}{\sigma} \cdot \underset{\sim}{D}_P = \xi \tag{2.37}$$

It is possible to interpret (2.36) as an additive decomposition of the rate of deformation tensor into elastic and plastic parts. However, strictly speaking it is not necessary to do so because none of the constitutive parameters introduced up to now depend on new parameters. This approach is in direct contrast to a more conventional one using the $F = F_e F_P$ decomposition, such as that utilized by Perez-Foguet et al (2003). To complete the development of the constitutive theory, we need to propose a constitutive equation for D_P. In order to accomplish this, we follow the procedure advocated by Rajagopal and Srinivasa (2005) and propose a constitutive equation for ξ of the form,

$$\xi = \hat{\xi}(RD, \underset{\sim}{D}_P) \tag{2.38}$$

where RD is defined by (2.7). We now demand that for given values of $\underset{\sim}{\sigma}$ and RD, the value of D_p is such that it maximizes ξ subject to the constraint that (2.37) be met. In order to carry out the maximization, we define the auxiliary function

$$\Phi = \xi - \lambda[\underset{\sim}{\sigma} \cdot \underset{\sim}{D} - \xi] \tag{2.39}$$

and differentiating this Φ by D_p we obtain,

$$\underset{\sim}{\sigma} = \eta \frac{\partial \xi}{\partial \underset{\sim}{D}_p} \tag{2.40}$$

where η is given by $\eta = \dfrac{1-\lambda}{\lambda}$

The value of η can be obtained by satisfying the constraint (2.37) resulting in

$$\eta = \frac{\xi}{\frac{\partial \xi}{\partial \underset{\sim}{D}_p} \cdot \underset{\sim}{D}_p} \tag{2.41}$$

In order to derive the actual constitutive model for the Duva and Crow model, we first split the $\underset{\sim}{D}_P$ into a purely deviatoric part and a mean normal part.

$$\underset{\sim}{D}_p = \underset{\sim}{\gamma}_P + \frac{1}{3} tr(\underset{\sim}{D}_p)\underset{\sim}{I} \tag{2.42}$$

We now assume that ξ is of the form

$$\xi = \alpha \{S\}^n \tag{2.43}$$

where

$$S^2 = \hat{a}(RD)\underset{\sim}{\gamma}_P \cdot \underset{\sim}{\gamma}_P + \hat{b}(RD) tr(\underset{\sim}{D}_P)^2 \tag{2.44}$$

and α is a material constant. This implies that the stress from (2.40) that

$$\underset{\sim}{\sigma} = \eta \frac{\partial \xi}{\partial S} 2\left(\hat{a}(RD)\underset{\sim}{\gamma}_P + \hat{b}(RD) tr(\underset{\sim}{D}_P)\underset{\sim}{I}\right) \tag{2.45}$$

which implies

$$\underset{\sim}{\sigma} = \bar{\eta}\left(\hat{a}(RD)\underset{\sim}{\gamma}_P + \hat{b}(RD) tr(\underset{\sim}{D}_P)\underset{\sim}{I}\right) \tag{2.46}$$

which can be inverted to obtain

$$\underset{\sim}{D}_P = \frac{1}{\bar{\eta}}\left[\frac{1}{\hat{a}}\underset{\sim}{\tau} + \frac{1}{3\hat{b}}\sigma_m \underset{\sim}{I}\right] \tag{2.47}$$

which is comparable to the velocity gradient proposed in (2.29). The coefficients $\hat{a}$ and $\hat{b}$ can be obtained in terms of the coefficients *a* and *b* defined through (2.27) and (2.28).

To calculate the value of $\overline{\eta}$, we start with the fact that

$$\underset{\sim}{\tau} = \overline{\eta}(a(RD)\underset{\sim}{\gamma}_P) \tag{2.48}$$

and

$$\sigma_m = \overline{\eta}(tr(\underset{\sim}{D}_P)) \tag{2.49}$$

From the fact that ξ can be expressed as

$$\xi = \underset{\sim}{\tau} \cdot \underset{\sim}{\gamma} + \sigma_m tr(D_P) \tag{2.50}$$

we get

$$\xi = \overline{\eta}(S^2) \tag{2.51}$$

Therefore, from (2.51) and (2.43), we get

$$\overline{\eta} = \alpha S^{n-2} \tag{2.52}$$

Substituting this form for $\overline{\eta}$, we can get the exact form of the model proposed by Duva and Crow given by the equation (2.29).

CHAPTER III

IMPLEMENTATION OF MATERIAL MODELS IN FINITE ELEMENT SOFTWARE ABAQUS

The constitutive model discussed in the chapter II is implemented into ABAQUS/ Explicit using the user subroutine VUMAT. VUMAT is the user subroutine written in FORTRAN programming language and is used to implement user defined material constitutive behavior in ABAQUS/ Explicit. With the use of this feature, a constitutive model of any complexity can be implemented with a finite element model and can be used with any compatible element type in ABAQUS. The structure also allows the user to input multiple user material subroutines in the same model. The user has the freedom to define any solution dependent state variables which are updated with the solution at each step. A schematic showing the interaction between the material subroutine and the software package is shown in Table 1.

In the large deformation analysis the data is transferred at each integration point. Deformation gradient tensor at the current time instant, $\underset{\sim}{F}(t)$, Cauchy stress at the current instant $\underset{\sim}{\sigma}$ and any user defined state variables (in our case, for instance the symmetric part of the plastic velocity gradient $\underset{\sim}{D}$ and the relative density RD), at the current instant are input from ABAQUS into the VUMAT. It also sends an estimate of the total deformation gradient at the next time

instant $\underset{\sim}{F}(t+\Delta t)$. The VUMAT then evaluates these values to estimate the values of F^e, T, D^p and RD at the next time instant $t+\Delta t$ and returns it to ABAQUS. This process is continued till the solution converges at $t+\Delta t$.

Table 1. Flow of data between ABAQUS and the VUMAT

ABAQUS	
• Solves the equilibrium equation at the current time step • Carries out the large deformation analysis to evaluate deformation gradient	
$\underset{\sim}{F}(t)$, $\underset{\sim}{F}(t+\Delta t)$ $\underset{\sim}{\sigma}(t)$, $s(t)$	$\underset{\sim}{\sigma}(t+\Delta t)$ $s(t+\Delta t)$
VUMAT	
• Carries out explicit integration to evaluate the following quantities at $t+\Delta t$ $\dot{\underset{\sim}{F}}$, $\underset{\sim}{L}$, $\underset{\sim}{D}$, RD, $\underset{\sim}{D}^p$, $\underset{\sim}{D}^e$, $\underset{\sim}{\sigma}$	

III.1. VUMAT for the Duva and Crow model

In this section we develop the numerical scheme based on an explicit first order Euler integration method for the implementation of the Duva and Crow model into a VUMAT.

The Green-Naghdi stress rate proposed by the Duva and Crow model is given by

$$\overset{\nabla}{\underset{\sim}{\sigma}} = 2\mu \underset{\sim}{D}^{e} + \lambda tr(\underset{\sim}{D}^{e})\underset{\sim}{I} \tag{3.1}$$

where $\underset{\sim}{D}^{el}$ is given, as defined through equation (2.36)

$$\underset{\sim}{D}^{e} = \underset{\sim}{D} - \underset{\sim}{D}^{p} \tag{3.2}$$

and the increment in stress is given by

$$\Delta\underset{\sim}{\sigma} = (\overset{\nabla}{\underset{\sim}{\sigma}} + \underset{\sim}{\Omega}\underset{\sim}{\sigma} - \underset{\sim}{\sigma}\underset{\sim}{\Omega})\Delta t \tag{3.3}$$

where $\underset{\sim}{\Omega}$ is the spin tensor defined through $\underset{\sim}{\Omega} = \dot{\underset{\sim}{R}}\underset{\sim}{R}^{T}$ where $\underset{\sim}{R}$ is the rigid body rotation in the polar decomposition of the deformation gradient tensor $\underset{\sim}{F}$.

The plastic strain rate $\underset{\sim}{D}^{p}$ can be determined from the stain rate potential by differentiating it with respect to the stress $\underset{\sim}{\sigma}$ which gives,

$$\underset{\sim}{D}^{p} = \frac{\partial\phi}{\partial\underset{\sim}{\sigma}} = AS^{n-1}\left(\frac{3}{2}a\underset{\sim}{\tau} + \frac{1}{3}b\sigma_{m}\underset{\sim}{I}\right) \tag{3.4}$$

where A is defined by

$$A = \frac{\dot{\varepsilon}_{0}}{\sigma_{0}} \tag{3.5}$$

The dilatation rate is given by $tr(\underset{\sim}{D}^{p})$ and the rate of change of relative density is given by

$$\dot{R}D = -RDtr(\underset{\sim}{D}^{p}) \tag{3.6}$$

A complete code of the VUMAT and explanation of the implementation is given in appendix A.

III.2. Validation of the VUMAT for the Duva and Crow model using the Gurson model

In order to use the Duva and Crow model effectively, it is necessary to estimate the constants A and the creep exponent 'n'. To do this, we make comparisons between the Gurson model and the current model in the range where the Gurson model is known to be accurate, at relative density of 0.9.

These tests were conducted for single elements undergoing compression and simple shear. The solution parameters like stress, plastic strain and relative density were compared.

III.2.1. Compression and shear test results

For the compression test, the single element was given a homogeneous compression in the Y direction. The compaction behavior and the Mises stress in the element obtained from both the models is shown in Figures 6, 7, 8 and 9.

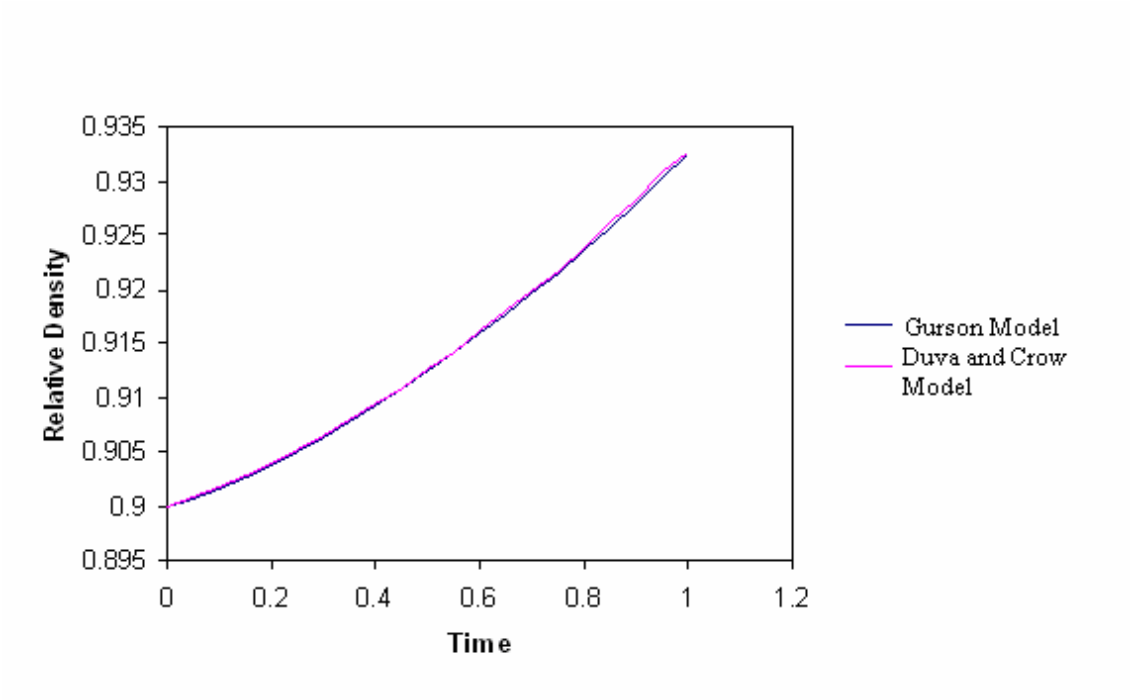

Fig 6. Compaction behavior obtained for compression test.

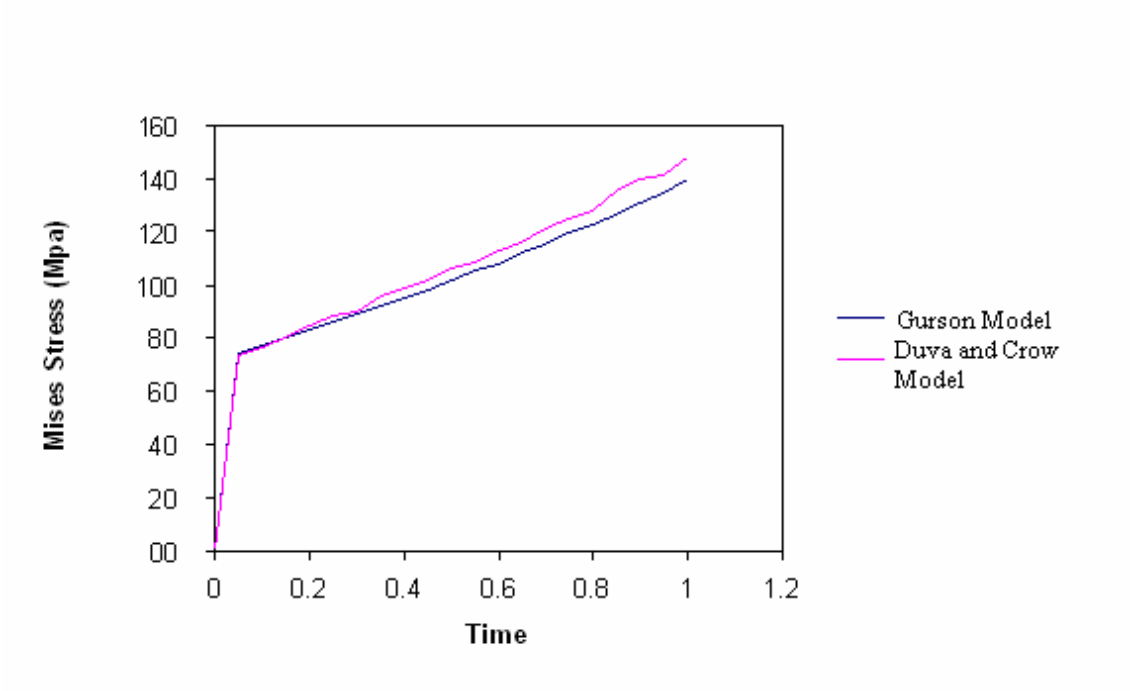

Fig 7. The Mises stress obtained for the compression tests.

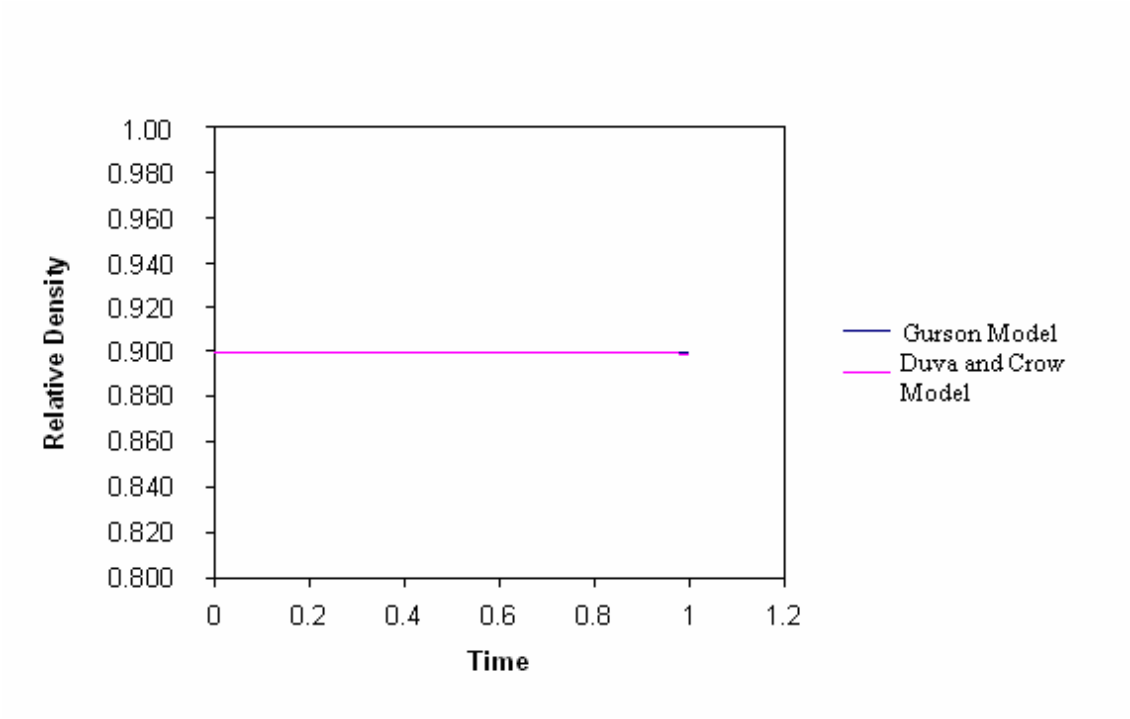

Fig 8. Compaction behavior obtained for shear test.

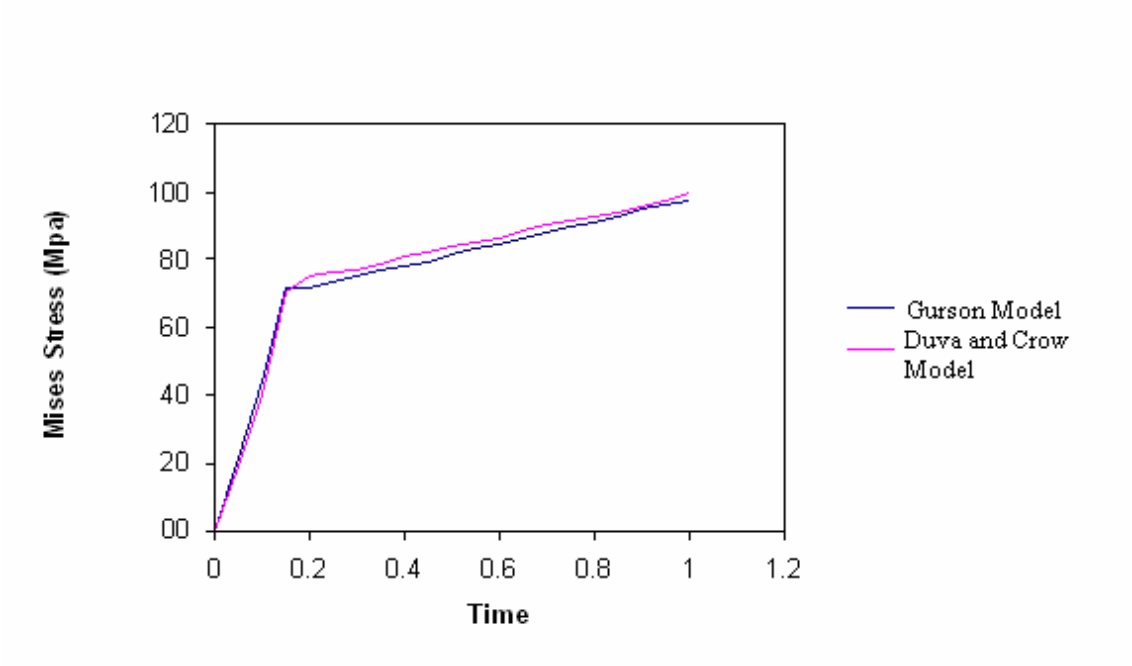

Fig 9. The Mises stress obtained for the compression tests.

From these tests, the values of the constant A and n were found as $A = 1.1 \times 10^{-21}$ and n=2. These values are now used in the simulations which use the Duva and Crow model.

III.2.2. Response of the element under homogeneous deformation using Duva and Crow model

Next, the response obtained from this model when applied to the powder undergoing the ECAE process needs to be studied. For this purpose, the displacement information, for one element, obtained from the full simulation which used the Gurson model for the powder medium is considered. The chosen element

is fully consolidated at the end of the simulation. The response obtained from both the models is compared. Parameters compared include Relative Density and components of the stress. The results are shown here.

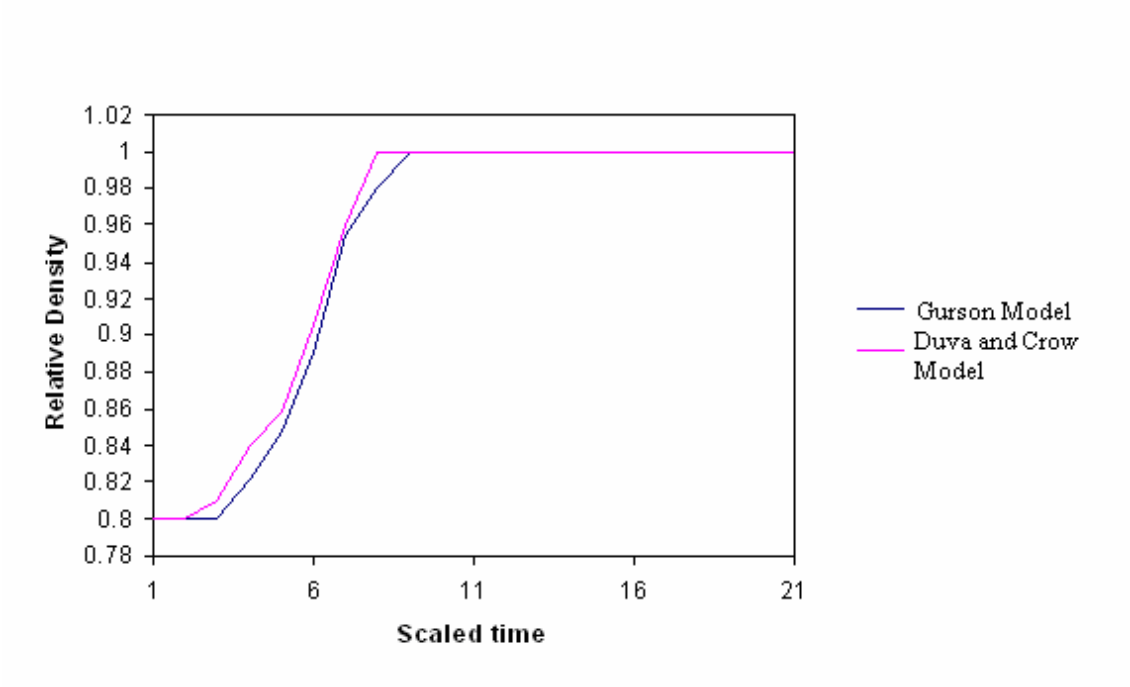

Fig 10. Relative Density (RD) vs. scaled time for a material undergoing homogeneous deformation obtained from an ECAE simulation.

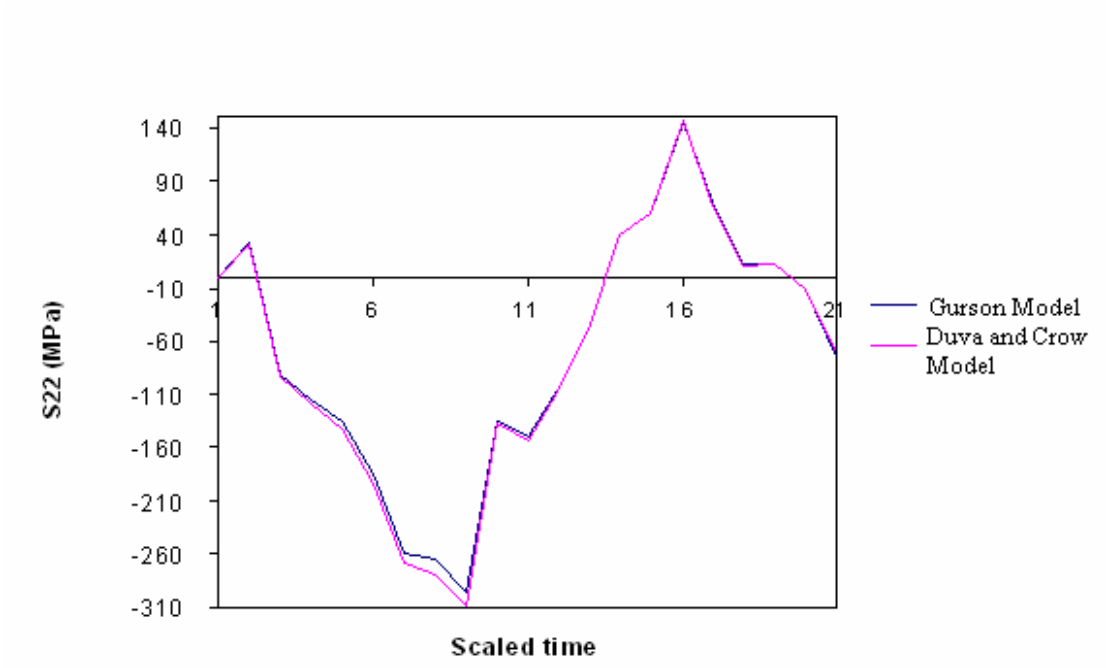

Fig 11. Stress (S22) vs. scaled time for a material undergoing homogeneous deformation obtained from an ECAE simulation.

From Figure 10, it can be seen that the response with the D&C model starts consolidating sooner than the Gurson model. From Figure 11 we observe that the response of the Gurson model is softer than the D&C model. After the material is fully dense, the stress response of both the models is very similar. This is because both models have the same elastic-plastic response for fully dense material.

CHAPTER IV

SIMULATION OF THE ECAE PROCESS

In this chapter certain key parameters involved with the ECAE process have been identified and the models used to simulate them through ABAQUS are explained.

IV.1. Properties of the can

The can is a block with a square cross section of side 1 inch and length of 4 inches. A circular hole of variable size can be drilled through this can leaving a length of 1 inch at the bottom intact. The circular hole is filled with powder and the top is closed using a plug of the same material as the can. This can is pushed into the die with the intact end in first.

A Mises type surface is used to model the metallic can in ABAQUS. It is defined by giving the values of uniaxial yield stress as a function of uniaxial plastic strain. Abaqus used isotropic hardening to model the yield surface from the given uniaxial stress strain data. An associative flow rule is then used to determine the plastic deformation rate, which is in the direction normal to the yield surface.

The strength of the material used for the can will have an effect on the compaction of the powder as shown through experimental works by Karaman et al. (2007). In this paper 2 different can materials viz. Copper and Nickel were chosen to compact copper powder. An attempt will be made to simulate the effect of the

can material on the compaction behavior of the powder. The can used in the simulations were made of 2 different materials, Copper and Nickel. The uniaxial stress strain data used for these materials to model their yield surface is given in table 2.

Table 2. Mechanical properties of the can materials

Material	Young's modulus (GPa)	Initial yield stress (MPa)	Yield stress at plastic strain =1
Copper	128	80	300
Nickel	206	300	500

The size of the hole can be detrimental to the compaction behavior of the powder inside and this phenomenon is verified in this dissertation. Also the effect of the length of the can on the compaction behavior is determined.

IV.2. Interaction conditions

Two interaction conditions need to be specified for any surface pair in contact viz. normal conditions and tangential conditions. The normal contact conditions used in this work is hard contact condition. One of the surfaces, (usually the one with stiffer material) is specified as the master surface and the other is specified as the slave. This condition makes sure that the nodes of the slave surface do not penetrate the elements of the master surface. Most commonly the pressure-clearance relation is defined by a zero pressure when surfaces are not in contact and when in contact, any amount of pressure can be applied between them to constrain

the motion of the slave nodes. The surfaces separate if the contact pressure reduces to zero. Separated surfaces come into contact when the clearance between them reduces to zero.

The tangential conditions are modeled using one of the two conditions, frictionless or dry (coulomb) friction. The basic concept of the Coulomb friction model is to relate the maximum allowable frictional (shear) stress across an interface to the contact pressure between the contacting bodies and the friction coefficient μ defined between the surfaces. In the Coulomb friction model, two contacting surfaces can carry shear stresses up to a certain magnitude across their interface before they start sliding relative to one another; this state is known as sticking. When the magnitude of shear stress exceeds the specified value, the surfaces can start moving relative to one other. This condition is known as slip.

Two key interactions need to be modeled in these simulations, viz. the interactions between the can and the die and between the can and the powder. The interaction between the can and the powder is modeled using hard contact and forcing the condition that the powder sticks to the can material. In the tangential direction, frictionless contact is assumed. This seems reasonable because macroscopically, there is very little relative motion between the can and the micron size powder.

Friction conditions between the walls of the can and the die depend on factors like the lubrication used, the type of rolling condition used at the wall etc. Special conditions on the die walls are usually used to reduce the friction between

the die and the workpiece. An example of this is shown in Figure 12. In the simulations carried out in this work, a similar rolling condition was used on the bottom face and on the two lateral faces. The friction conditions used in the simulations are shown in Figure 13.

Friction directly affects the loads that need to be applied to extrude the workpiece. It has also been shown in the past that friction affects the microstructure and the strains developed in the workpiece undergoing ECAE in works like those by Prangnell (1997), Bowen et al. (2000), Luis et al. (2002) and Oh and Kang (2003). It is critical to determine the appropriate friction conditions to model the process accurately. In this work, the friction conditions were determined by comparing the simulation results with experimental results for a bulk copper billet and a hollow can. This is explained in detail later in section 4.7.

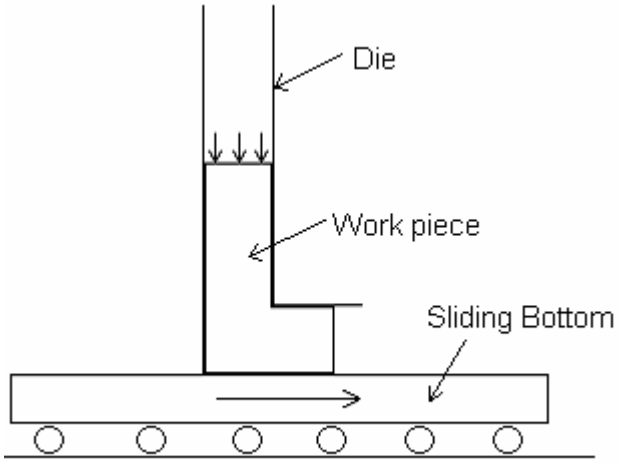

Fig 12. Special die configurations to reduce friction during ECAE.

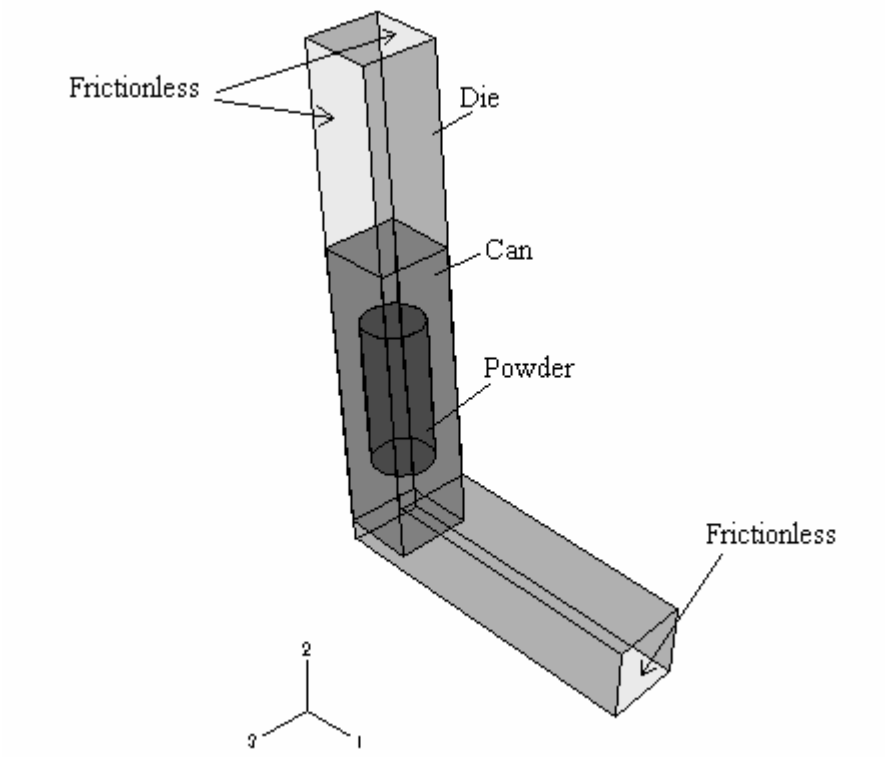

Fig 13. 3-D Schematic of the ECAE die with a can and powder. The surfaces where the die walls slide with the can are shaded lighter in color and marked frictionless.

IV.3. Back pressure

Back pressure technique is a modification to the ECAE process where a counter pressure is applied to the leading edge of the workpiece as it emerges out of the exit channel, as shown in Figure 14. This method has been used to achieve better workability and more uniform microstructures in bulk billets as presented by Stolyarov and Lapovok (2003) and Stolyarov et al., (2003). Simulations using back pressure have been performed and have shown that back pressure produces higher and more uniform shear strains in bulk materials (Oruganti et al., 2005). In the

simulations conducted here, back pressure is applied by using a pressure loading condition in the appropriate direction on the elements on the leading edge of the extruded workpiece which emerge from the exit channel.

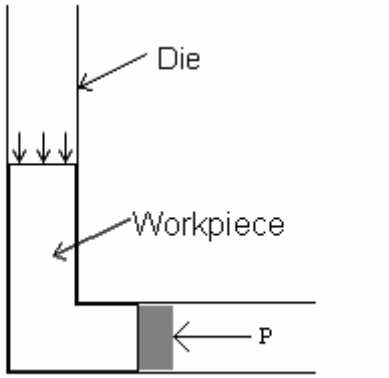

Fig 14. Schematic showing ECAE with back pressure.

IV.4. Initial powder density

The initial density of the powder in the can depends on the filling procedure used and any preprocessing done to the powder before it undergoes ECAE. In recent works, Karaman et al (2007) have shown the effects of various filling techniques like manual tapping of the powder, hand pressing during filling and cold isostatic pressing. The different filling techniques used will result in different initial powder densities. The effect of having different initial powder densities will be studied in this dissertation.

In this work, the powder is assumed to have a uniform distribution of density. An initial relative density of 0.65 is used in this work .

IV.5. Crosshead velocity

The typical crosshead velocities are in the range 2.5mm/s. In the FEM simulations, because of the mass scaling, there is a corresponding time scale which makes the simulation crosshead velocity several times than the actual rates. In this work, three different velocities viz. 0.5 mm/s, 2.5 mm/s and 10mm/s were studied.

IV.6. Multiple passes

A key advantage of ECAE is that the cross section of the workpiece does not change after the extrusion. Thus it can be extruded again through the same die multiple times to accumulate higher and higher plastic strains. This process has been shown as an effective way to achieve smaller grain sizes in bulk materials. During powder compaction through ECAE, it has been shown as an effective means to achieve full compaction. A comprehensive study by Karaman et al. (2006) has shown that a 2 pass ECAE to consolidate powders not only gives better consolidation but also considerably affects the material characteristics of the consolidated solid. The effect of 2 passes will be studied here through 2-D simulations. The die designed to simulate the multiple passes is shown in Figure 15. In the first step the top surface is given a downward velocity and in the second step, the surface to the left is given a horizontal velocity to the right. This motion is equivalent to rotating the workpiece by 180^0 about its central axis and passing it through the die again for the second pass.

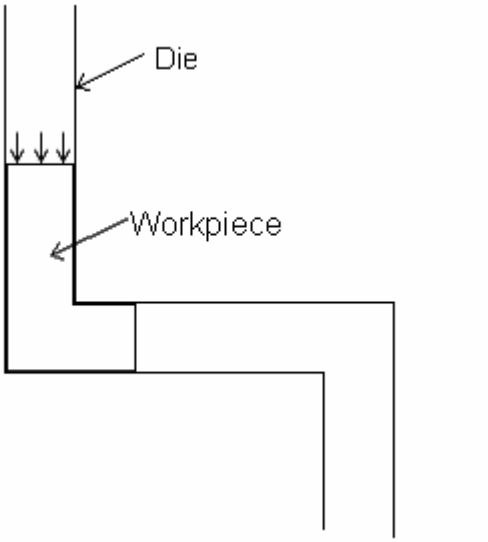

Fig 15. Die design for 2-Pass ECAE with 180^0 rotation of the workpiece about the longitudinal axis.

IV.7. Validation using experimental results

A key step is to validate the finite element model with the experiments, to assure that the boundary conditions (such as the friction coefficients, the contact conditions etc) and the constitutive model for the solid material are reasonable. These validations were performed for the extrusions with a solid billet. A copper billet with an original rectangular grid inscribed at the center of the billet after splitting the billet longitudinally into two was extruded through ECAE. The corner angles this gird made after the extrusion were compared to the angle made by the simulated elements of the mesh. In addition, the major geometric parameters such as final length, shape and the punch load etc were compared. Another step in the validation was to extrude an empty can (without the powder) and compare the

experimental shapes to the simulations. With these steps, the boundary conditions were optimized and it was determined that the boundary conditions and constitutive equations for the solid material described earlier were reasonable.

IV.7.1. Bulk billet

The first step in validating the finite element model with the experiments is comparing the experimental results with the model for a solid billet. Figure 16 shows the extruded solid billet with an original square grid and Figure 17 shows the same result form the simulations. Figure 18 shows the load curve for this extrusion process observed during the experiments and the load data from the simulation is shown in Figure 19. To determine the friction condition accurately, the load estimate from the finite element simulation was compared to the actual load from experiments for a range of friction values. The loads compared favorably at friction value of 0.08. This value of friction between the walls of the die and the can will be used for all further simulations.

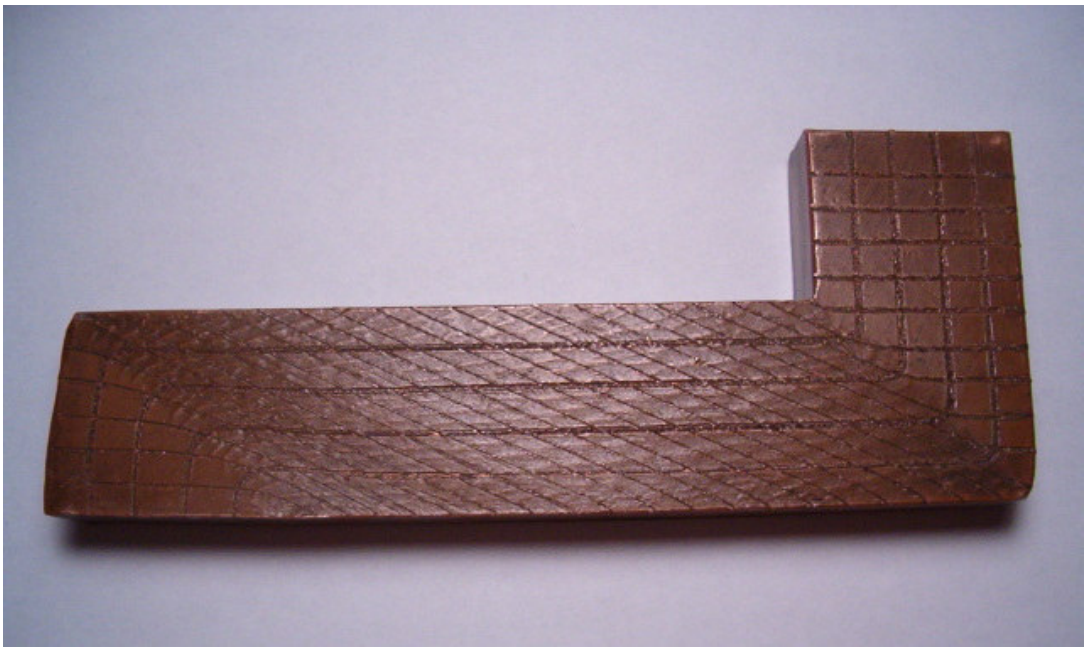

Fig 16. Extruded copper billet with an initial square grid inscribed on it.

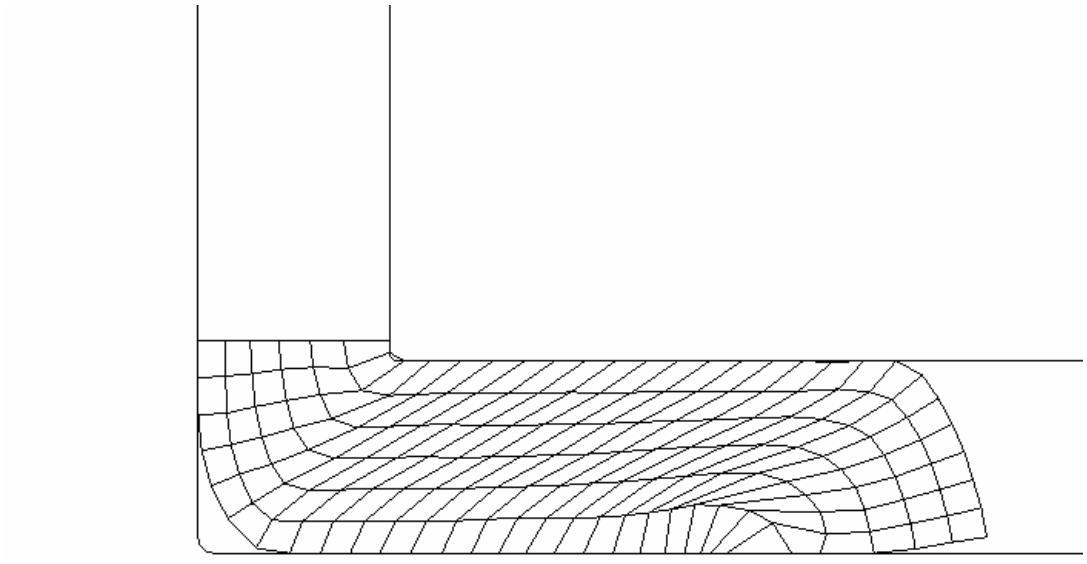

Fig 17. Simulation result for copper billet.

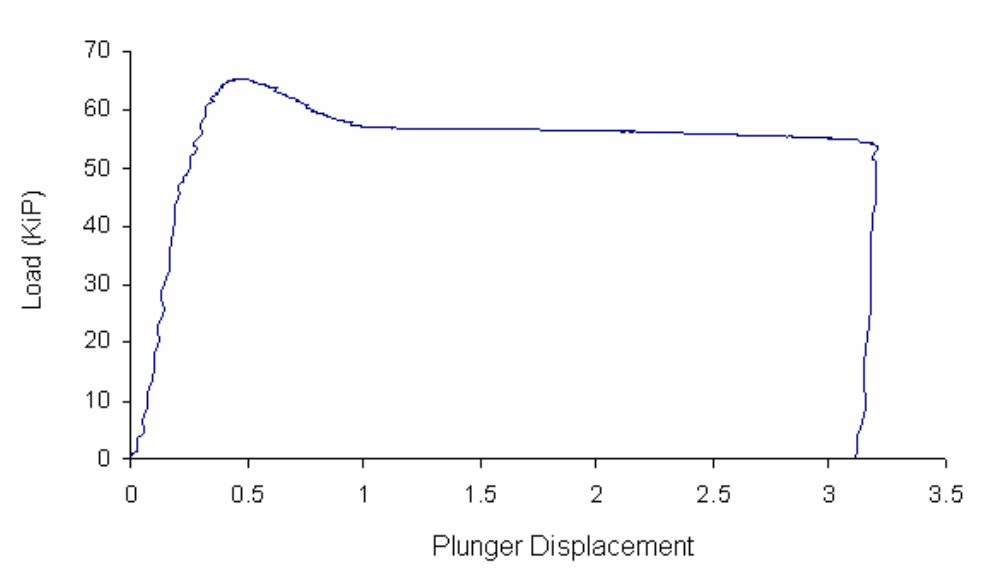

Fig 18. Experimental data (Load in KiP on Y axis, displacement of plunger in inches on X axis).

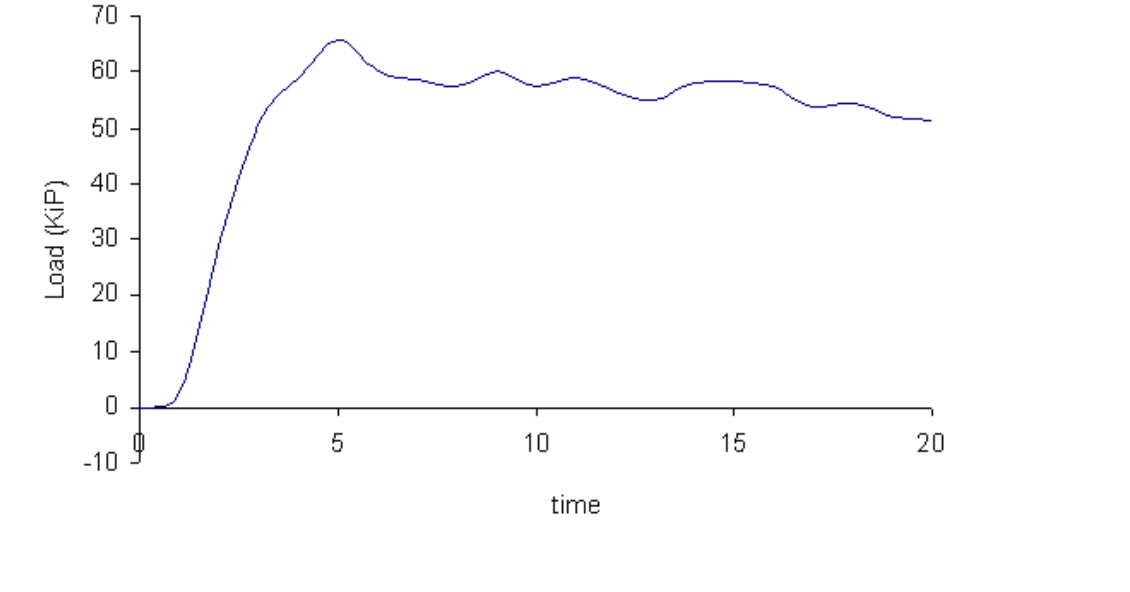

Fig 19. Simulation data (Load in KiP on Y axis, displacement of plunger in inches on X axis).

IV.7.2. Hollow can

Another step in validating the interaction conditions between the can and the die was to extrude a hollow Copper can (without the powder in it) through the die. The aim of this exercise was to be able to compare the deformation observed in the extruded hollow can through the finite element model. Figure 20 shows the cross section of the extruded copper can from the experiment. It was seen that the hollow can buckles after the bottom portion of the can has passed through creating a trough on the bottom as seen in Figure 21. This deformation was also observed in the simulations. Figure 22 shows the cross section obtained from the finite element simulation. Also the final size of the hollow in the can was comparable.

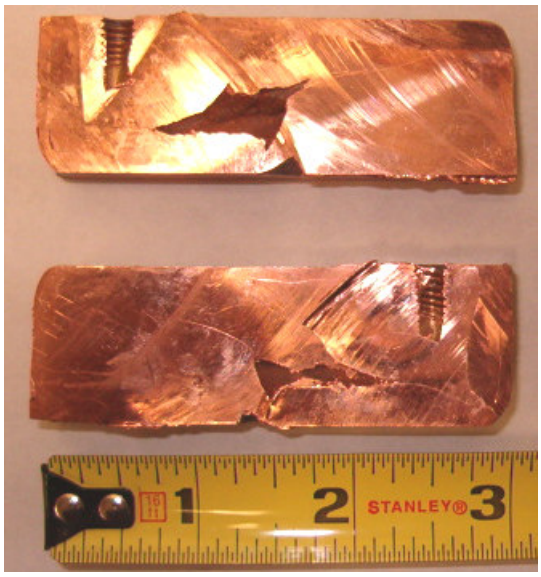

Fig 20. Cross section of an empty can after 1 pass.

Fig 21. Bottom of can showing the indentation.

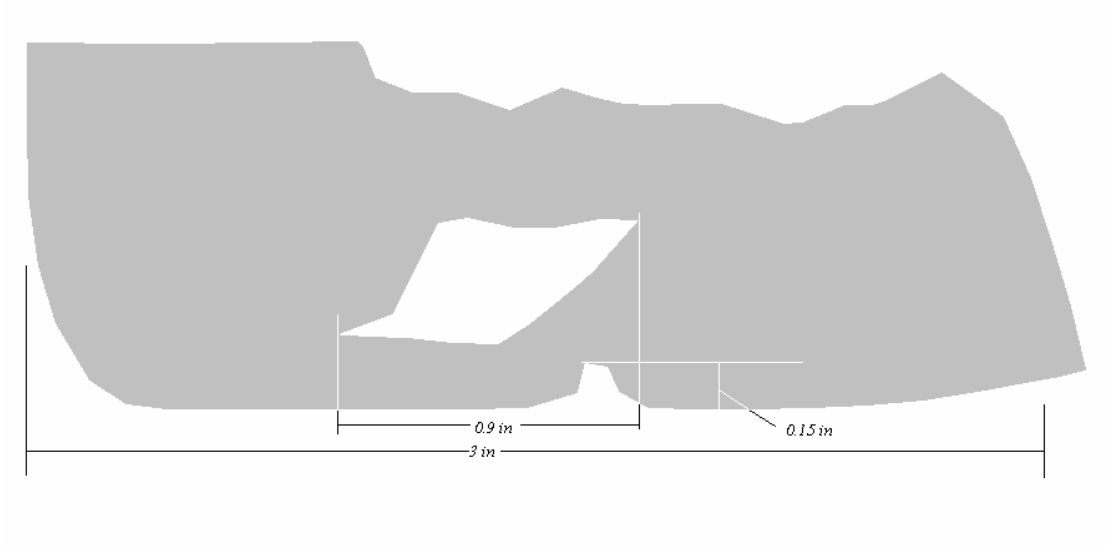

Fig 22. Picture to show the geometry of an extruded hollow can obtained through the simulations.

CHAPTER V

RESULTS

V.1. 2-D simulation results

The main purpose of the 2-D simulations was to study the efficacy of the powder material constitutive models to model the ECAE process under relatively simple simulation conditions. In these simulations, we started with a powder of relative density of 0.8. The key results discussed in this section are the comparison of the kinematics and the stresses obtained from the 2 constitutive models as the work piece is extruded.

Figures 23 A and B show that both models predict almost full densification is achieved near the inner corner of the intersecting channels. The densification profile and the final shape of the work piece are similar for both models. It should be noted that in Figure 23-A, void volume fraction is plotted whereas in Figure 23-B, Relative density is plotted (It should be noted that the color codes in both the figures correspond to same relative density). To further study the stress states in the material and compare them for the two constitutive theories, we select an element from the mesh which is about at the center of the work piece. For this element, we track its volume, the relative density and the stresses as it undergoes the extrusion. Figure 24 shows the sequence of the configurations of the work piece as it passes through the die. The element that is selected for analysis is marked as a dark spot.

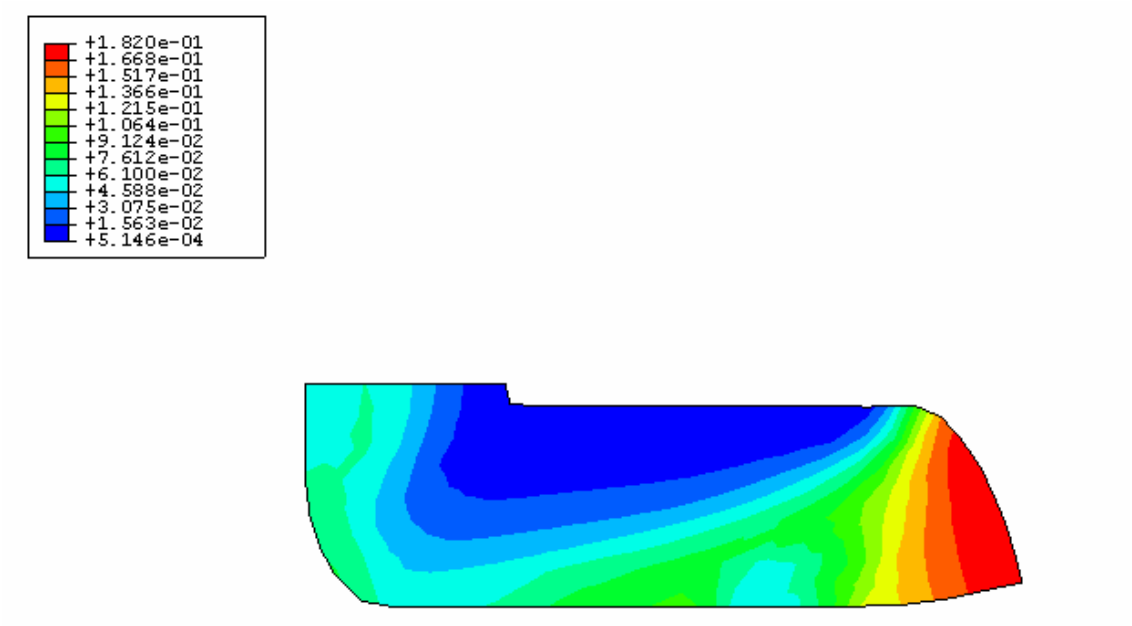

A

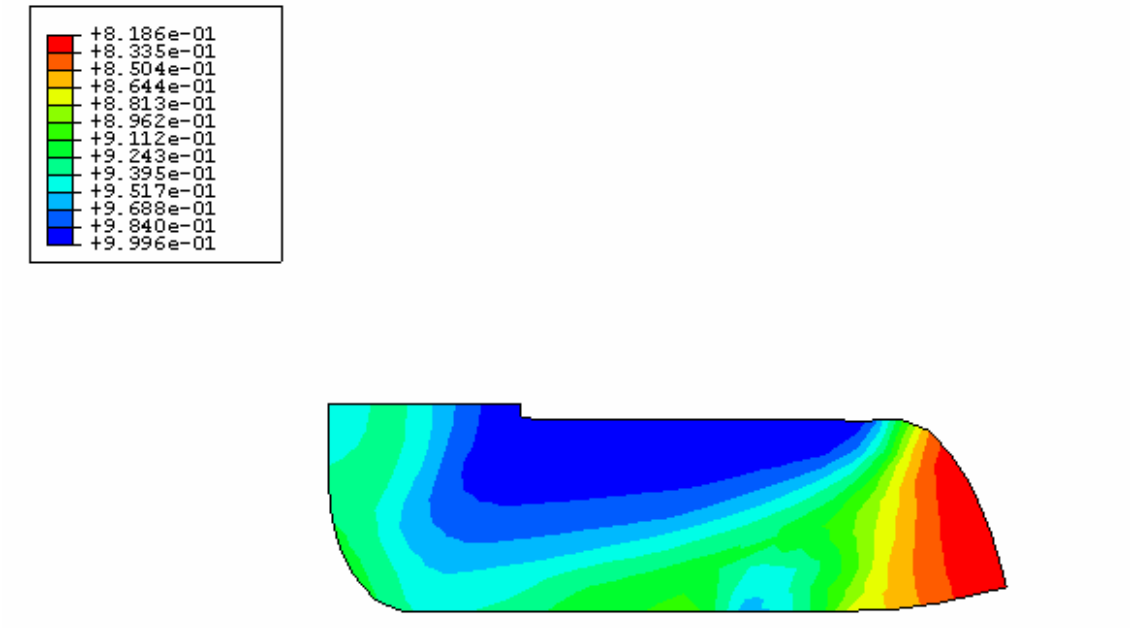

B

Fig 23. Contours and final shape of the extruded porous work piece. A) Contours for void volume fraction using the Gurson model, B) contours for the relative density using the Duva and Crow model.

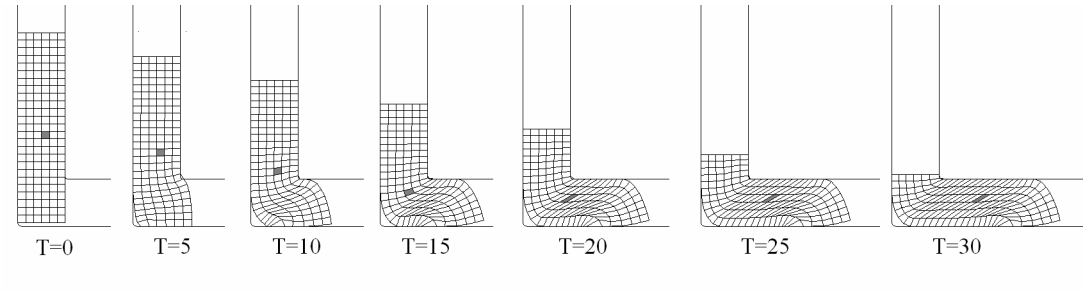

Fig 24. Sequence of the shape evolution of 2-D powder medium during the ECAE predicted using Duva and Crow model (selected element is marked dark). T=0 is the initial state of the workpiece and T=30 is fully extruded.

From Figure 25A, we can see that the volume of the element decreases continuously until it passes through the corner completely. Once it passes through the corner, there is no change in the volume after the powder enters the exit channel and the material does not consolidate further as also seen from Figure 25B. The reason for consolidation before entering the bend is clear from Figures 26A and 26B where we can see that a high hydrostatic pressure is built in the material before it enters the shear zone.

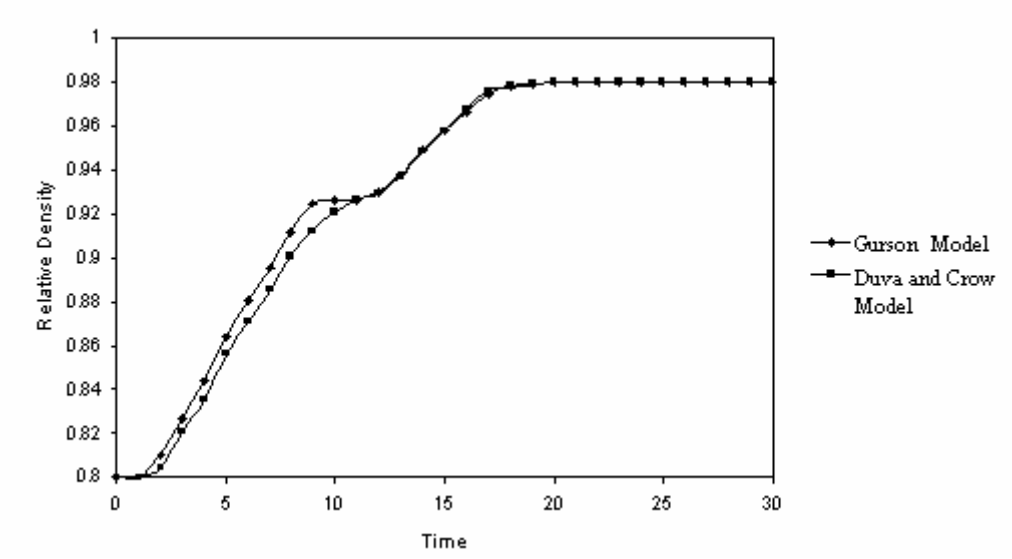

A

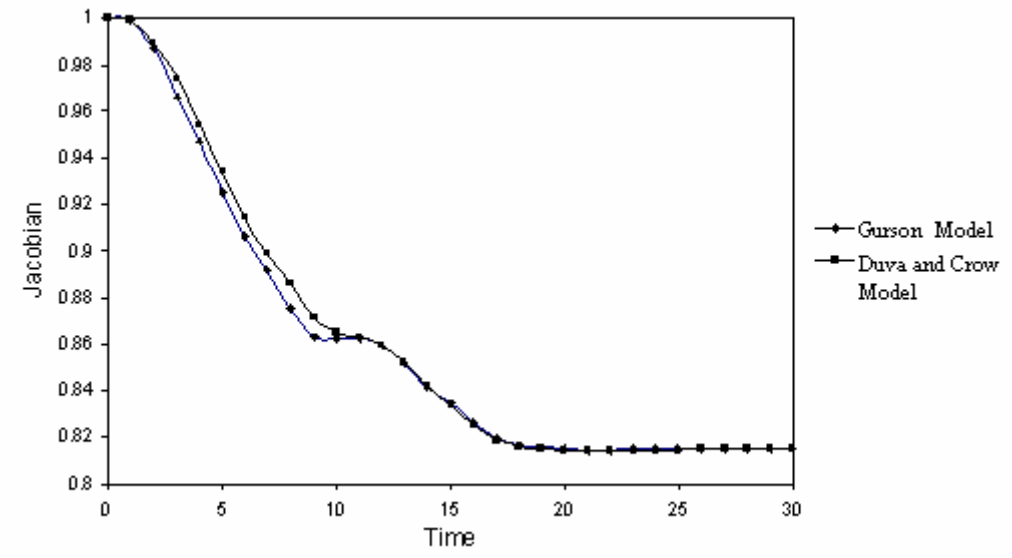

B

Fig 25. A) Volume of the selected element with initial volume scaled to 1, B) relative density of the selected element plotted against process time. It can be seen that most of the change in volume takes place before the element enters the bend (T<10) and no consolidation takes place after it has passes through (T>20).

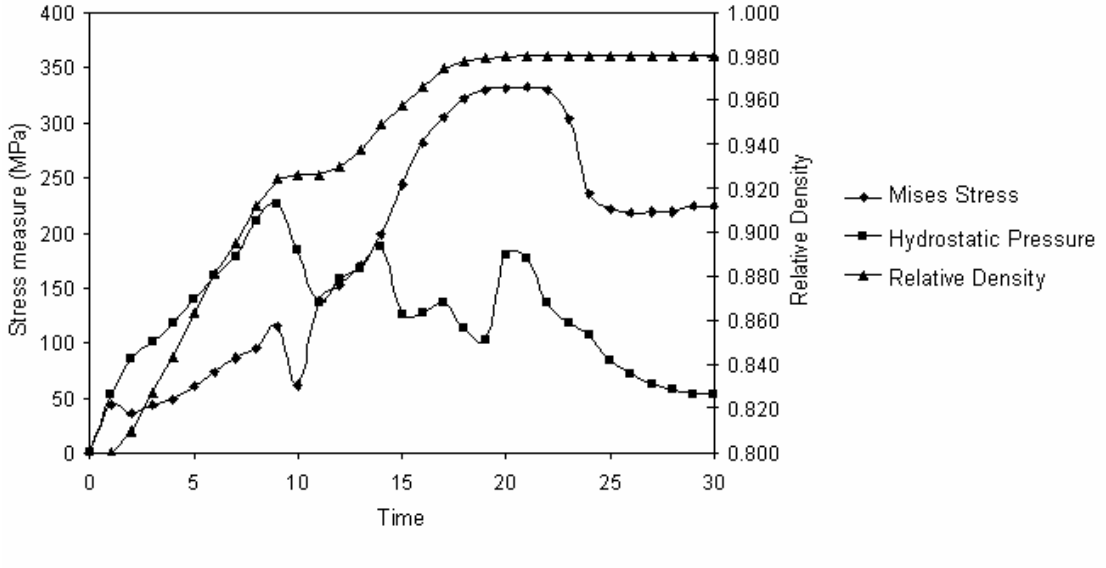

A

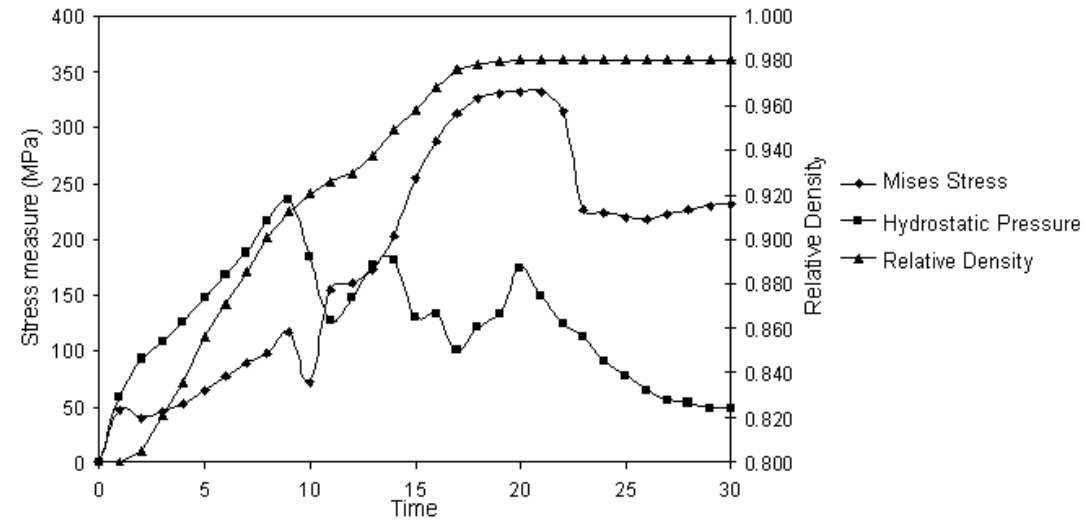

B

Fig 26. Mises stress, hydrostatic pressure (negative mean normal stress) and relative density obtained using A) Gurson model and B) Duva and Crow model plotted against process time. It can be seen that a high hydrostatic pressure is developed before the element passes through the bend, resulting in most of the consolidation.

From these figures, it is clear that both models predict similar stress response for the powder. Although there are subtle differences in the stress and relative density predictions, the stresses conditions in the material leading to consolidation are the same.

In the previous literature, Yoon and Kim (2006) had shown through simulations that the powder solidifies fully before it enters the corner and the deformation in the corner is simple shear. On the other hand, our 2-D simulations show that the powder does not fully compact before it enters the entry channel especially around the bottom portion of the work piece. This result is encouraging because the experiments showed similar uncompacted region in the bottom region of the powder compact.

V.1.1. Effect of mesh density

To study the effect of mesh density on the deformation of the powder medium, three different meshing densities were used viz. 150 elements (6x25) 360 elements (9x40) and 600 elements (12x50). The key region to be observed in this analysis is the region of interaction between the can and the die at the sharp corners. These are the corners where the nodes of the die can penetrate the elements of the workpiece. Therefore it is critical to mesh the workpiece in such a manner that the effect of the die penetration is felt to the minimum.

Figures 27-A and 27-B show a comparison of the two deformed meshes for the two extreme cases of mesh densities. It can be seen that the non-uniformity in

the deformation on the lower end is confined to a smaller area when the finer mesh is used. Figures 28-A and 28-B show the region of the inner corner zoomed in for both the coarse and the fine mesh respectively. It can be sees that for the coarse mesh, a fine gap is formed near the inner corner which is minimized in the fine mesh case.

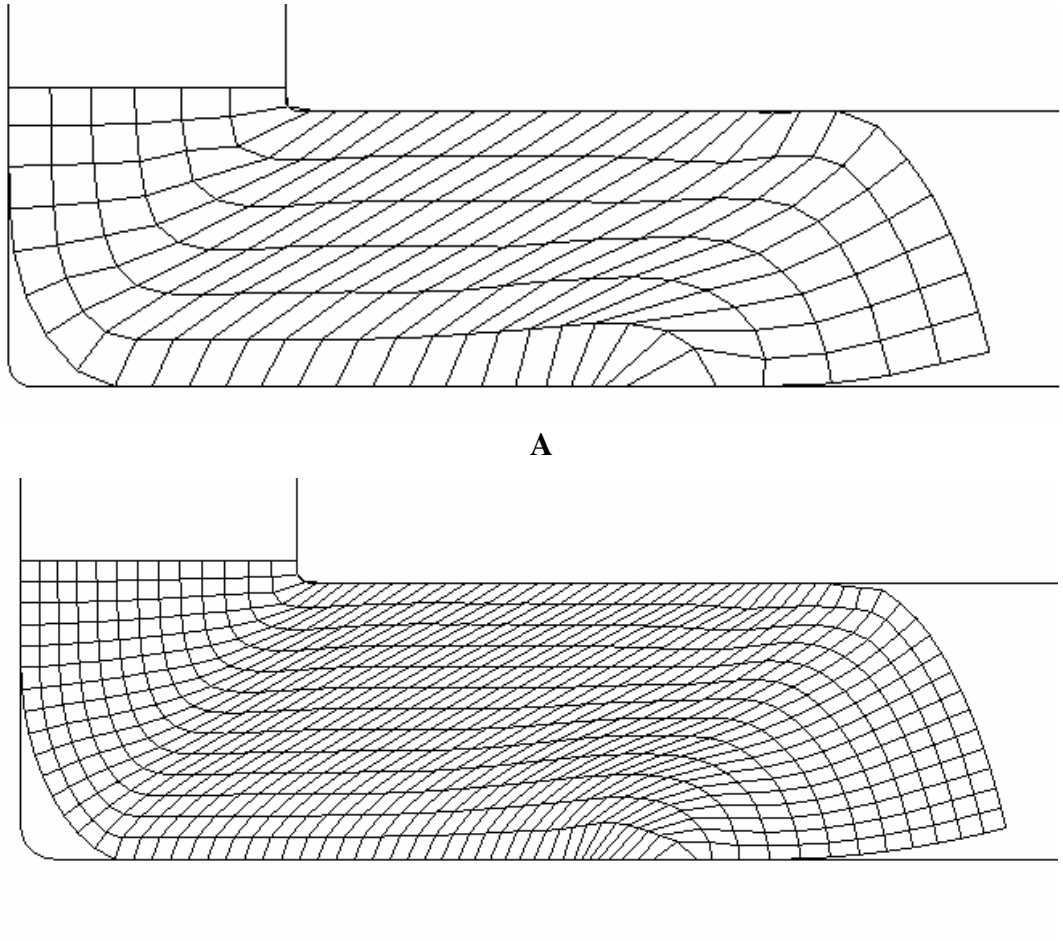

A

B

Fig 27. Deformed shape of the workpiece for A) mesh density 6x25 and B) mesh density 12x50.

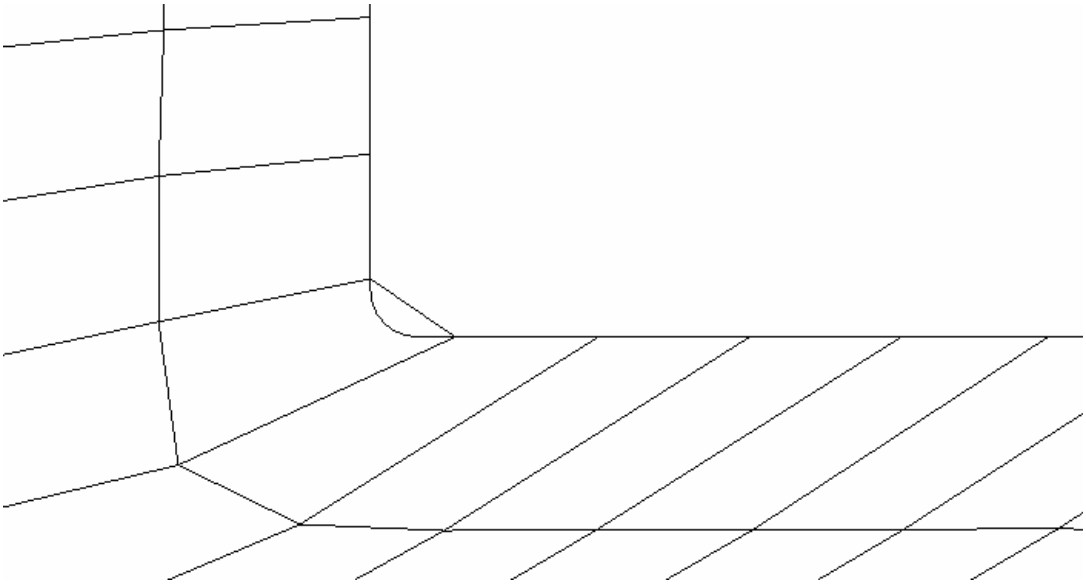

A

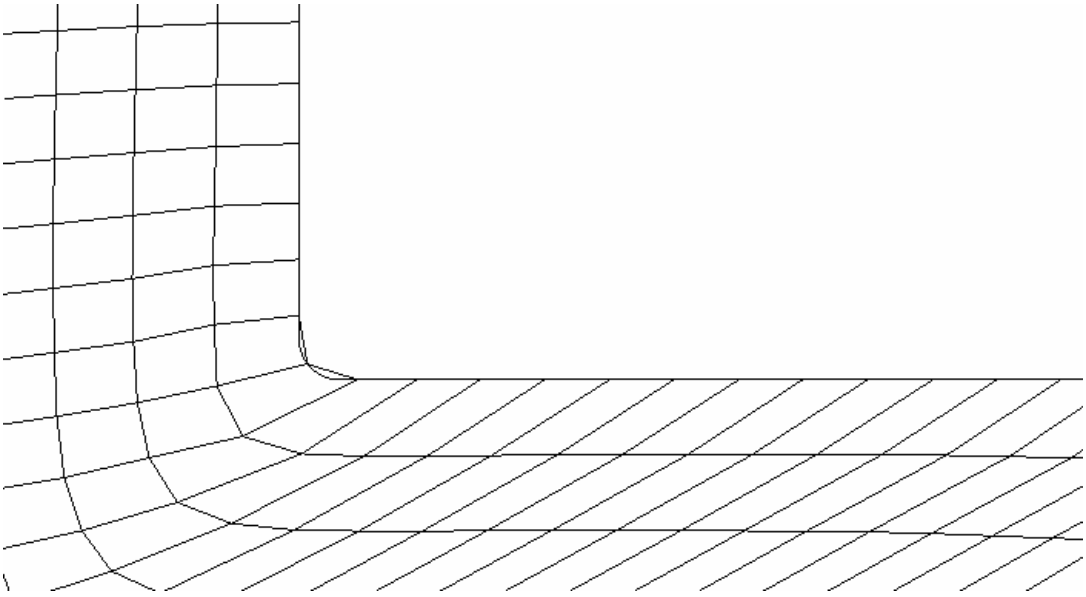

B

Fig 28. The effect of mesh size on penetration of the die nodes into the work piece. A) mesh density 6x25 and B) mesh density 12x50.

Figure 29 shows the maximum percentage difference in the relative density after extrusion when compared to the simulation with finest mesh plotted against the mesh density. It can be seen that for the coarsest mesh used here, the solution remains within 2% of the solution using the fine mesh. Also, it can be seen that the total computation time using the finest mesh is approximately 8 times the total computation time using the coarsest mesh.

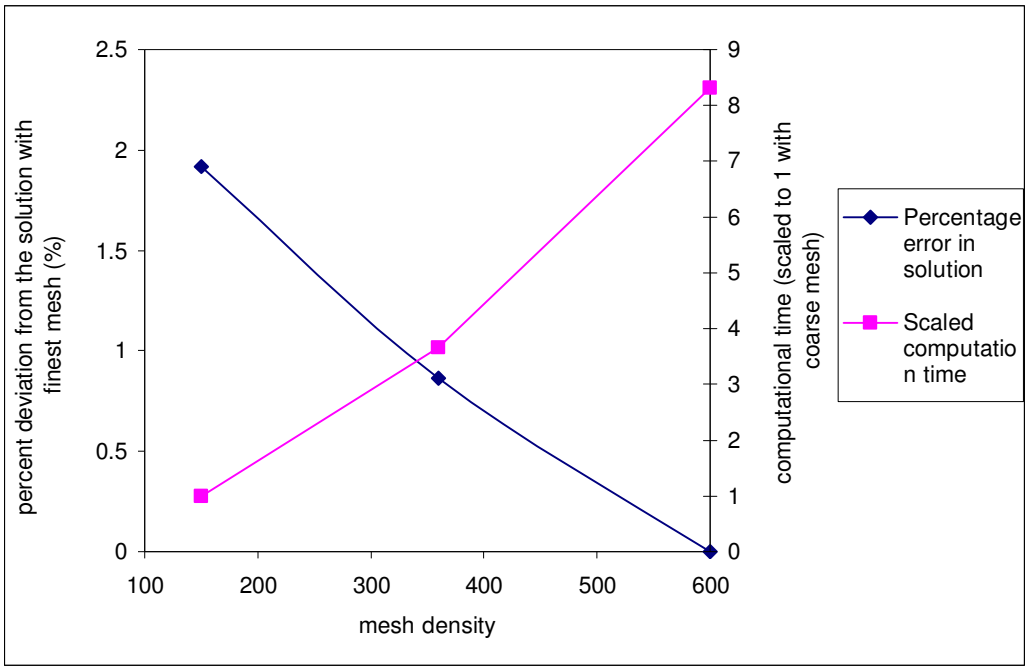

Fig 29. Percent deviation from the solution using the finest mesh and computation time scaled to 1 using the coarsest mesh, plotted against mesh density.

V.1.2. Effect of mass scaling

A naïve simulation using the explicit integration scheme revealed that the time steps of the order of 10^{-8} s are required for convergence. Considering that the

process of extruding a billet takes approximately 30 seconds, the simulation run for this process time would take prohibitively large computational times. Thus, a scheme needs to be applied to reduce the computational times.

ABAQUS/explicit integration scheme works by implementing an Euler integration scheme to solve the dynamic equations of motion. The term explicit is used because the expression for the solution at the next time step is expresses explicitly in terms of the solution at the previous time step. These integration schemes are conditionally stable and a condition for stability is that the time increment be given by $\Delta t = \min\left(\frac{L_i}{c_i}\right)$ over all elements, where L_i is the characteristic length of an element in the mesh and c_i is the dilatational wave speed given by $c_i = \sqrt{\frac{\lambda + 2\mu}{\rho}}$ as explained in detail by Harewood and McHugh (2007). Thus we can see that increasing the density would result in a larger time increment for stability of the solution and thus reduced number of increments. This scheme would work in our scenario because the constitutive model does not depend on the absolute density of the material, but on the relative density.

Great care should be taken so that the inertial effects due to the time scaling do not greatly affect the solution. To study the effect of this mass scaling, mass scale factors of 1, 10, 100 and 1000 were used.

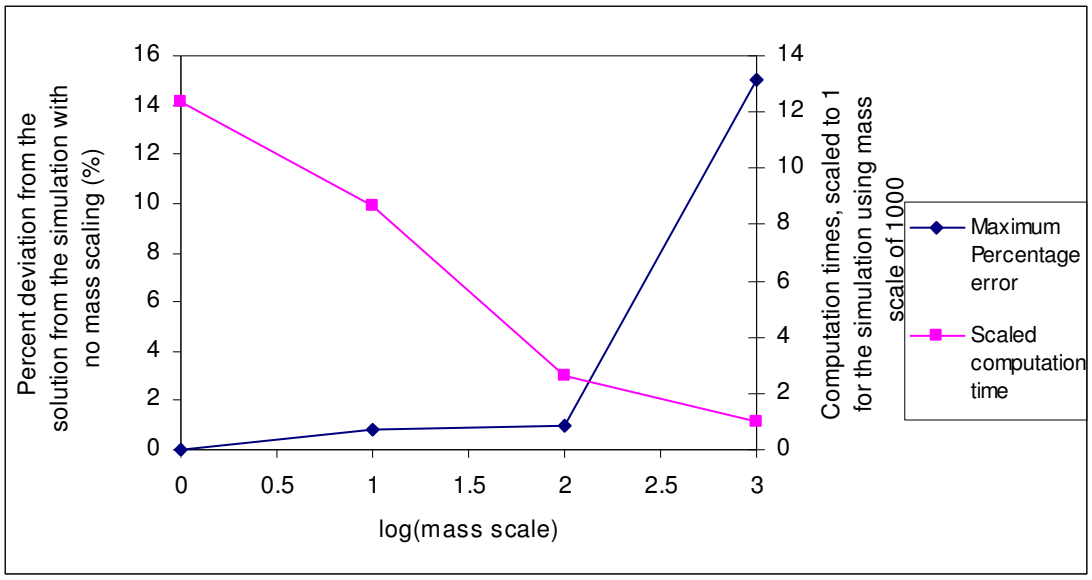

Fig 30. The maximum percentage difference in the relative density solution obtained from simulations with mass scaling and the total computation time, scaled to 1 with mass scaling of 1000 plotted against the log of mass scaling factor.

Figure 30 shows the maximum percentage difference in the relative density after extrusion when compared to the simulation at mass scaling factor of 1 plotted against log of the mass scaling factor. It can be seen that for mass scaling of up to 100, the difference in the deformation remains within 1% of the simulation with no mass scaling. Also the computation time with mass scale of 100 is reduced by 4.688 times when compared to simulation with mass scaling of 1.

V.1.3. Results for 2-pass ECAE

Figure 31-A shows the contours for the relative density obtained through a 2-D simulation starting with a relative density of 0.8. The contour after 1 pass is

shown in Figure 23-B. It can be seen that the whole region (except the two ends) is fully consolidated. Figure 31-B shows the deformed elements after 2-Pass ECAE. The elements (away from the ends) tend to go back to their original rectangular shape because of reversal of the shear strains, but the original rectangular grid is not obtained because of combined compression with the shear deformation. Figure 32 shows the deformation of the workpiece at an intermediate time step while undergoing the second pass. Notice that the shear in the elements is reversed in the shear deformation zone.

In Figure 33, the relative density of an element is plotted with respect to time. The element for which the relative density is plotted is marked in gray in Figure 31-B. It can be seen that the material in the element is only partially consolidated at the end of the first pass and then consolidates fully during the second pass. The first pass is represented by the first 30 seconds in the time scale and the second pass is on the 31-60 seconds. Notice that the during the second pass, the material in the element does not start consolidating immediately, which is unlike the first pass where the material start consolidating as soon as the workpiece starts extruding. The material consolidates only when the element passes through the shear zone.

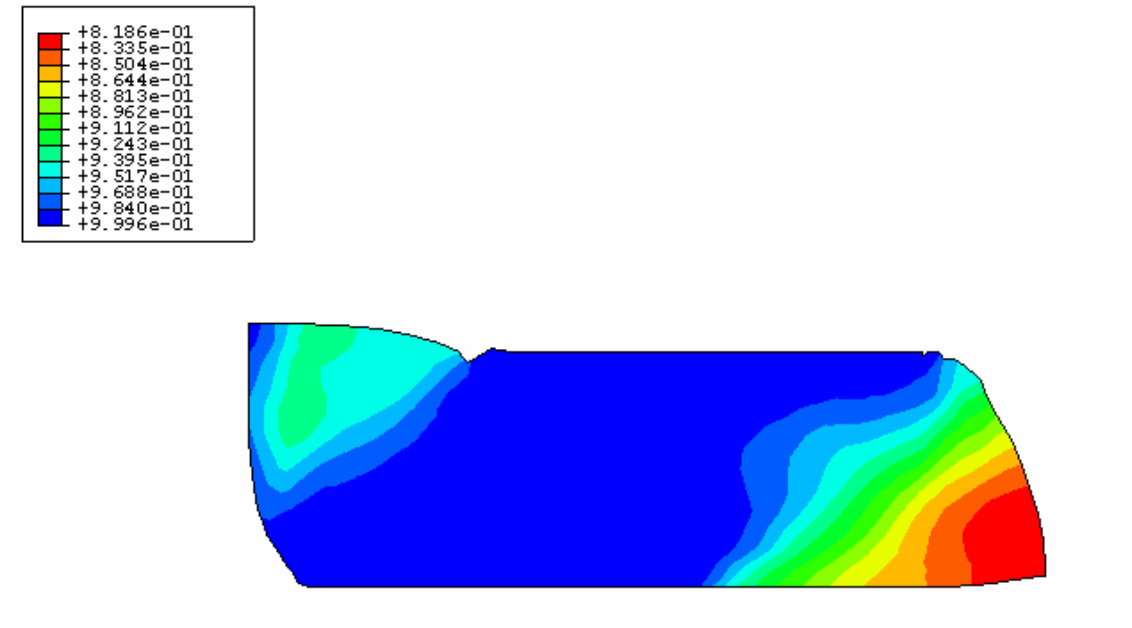

A

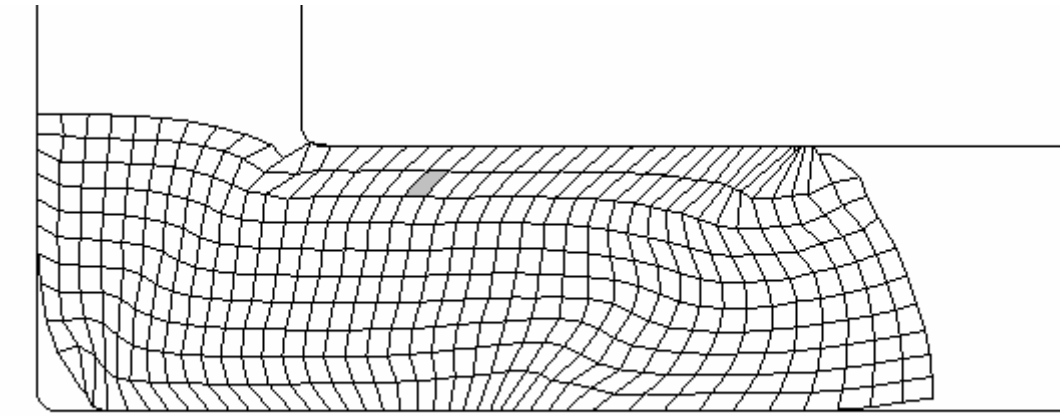

B

Fig 31. A- Relative density contours in the extruded workpiece after 2 passes. B- The deformed elements after 2 passes.

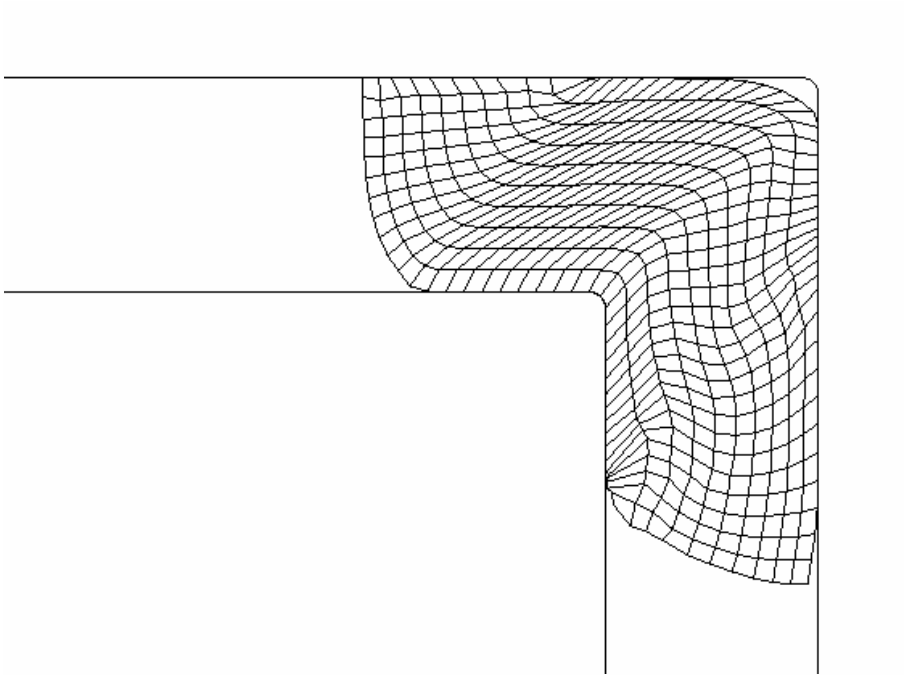

Fig 32. The extruded workpiece halfway through the second pass. Notice the reversal of shear in the shear zone.

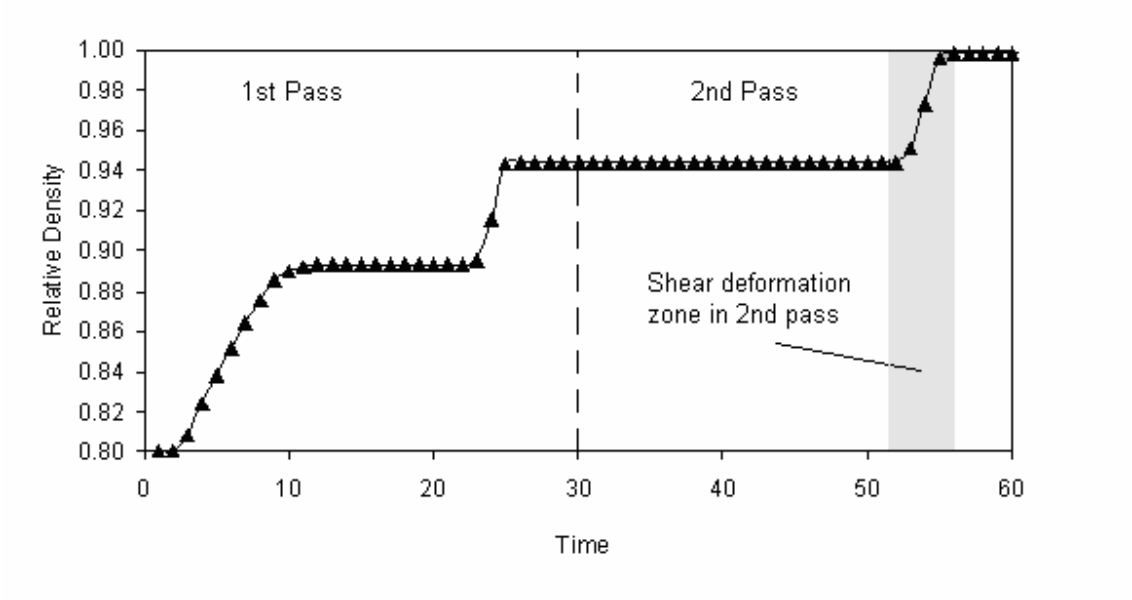

Fig 33. The relative density of a selected element (marked in gray in figure 31-B) during the extrusion. Notice in the second pass, the consolidation occurs only in the shear zone.

V.2. 3-D simulation results

To study the powder compaction process in detail, we first try to compare the 3-D simulations with the experiments for verification. For this we compare the distribution of the relative density of the compacted powder macroscopically and the angle by which the particle boundaries shear. After the validation, we try to explore the effects of changing various design parameters on the compaction behavior.

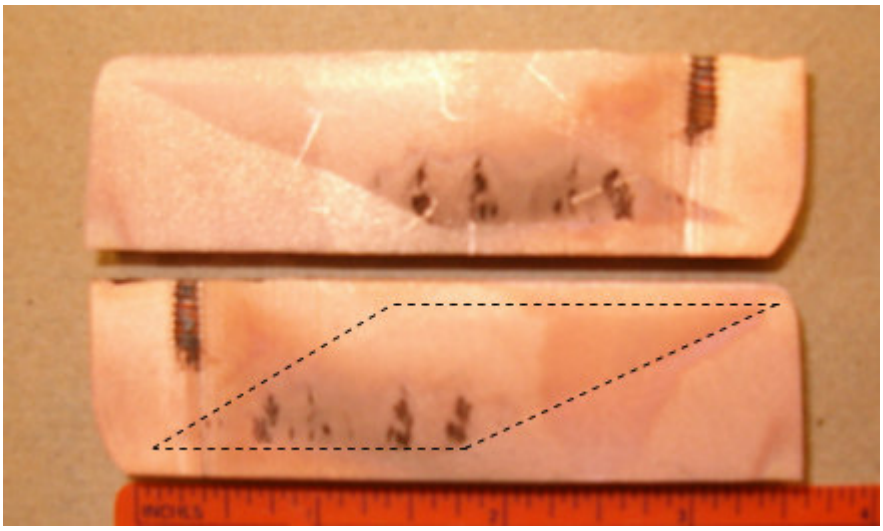

Fig 34. Middle section of extruded can with powder. The compacted powder is marked with the dotted outline.

Figure 34 shows the cross section of an extruded powder with can which showed voids on the lower region of the compacted powder. Figures 35 and 36 show contours for the void volume fraction and the relative density, respectively, at the middle section of the compacted powder. In these simulation results, we can see that the leading and the back corners of the powder core shows almost no

densification. This anomaly might be because of the type of boundary condition applied which requires that the powder stick to the walls of the can. Also in Figure 36 we can see that the Duva and Crow model predicts the location of the unconsolidated cavities more precisely. The angle measured from the OM pictures was 26.4 degrees. The angle obtained from the simulation using the Gurson model is 28.4 degrees and using the Duva and Crow model is 27.6 degrees.

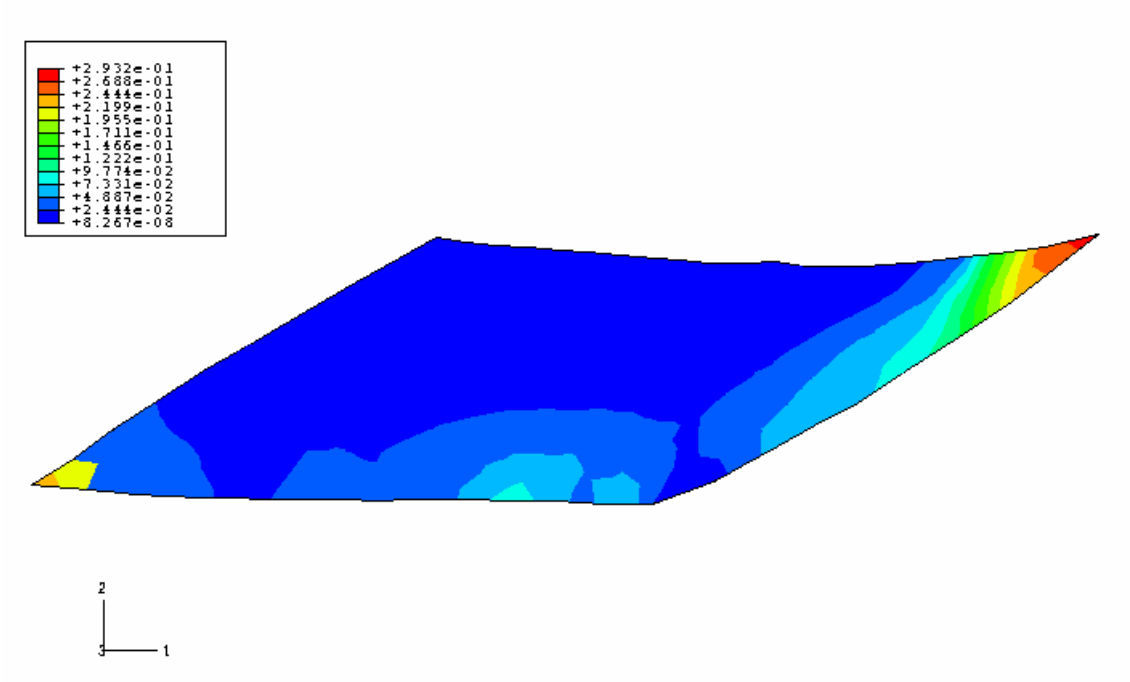

Fig 35. Void volume fraction predicted by Gurson model. The dark blue regions are fully consolidated and the red region shows least consolidation.

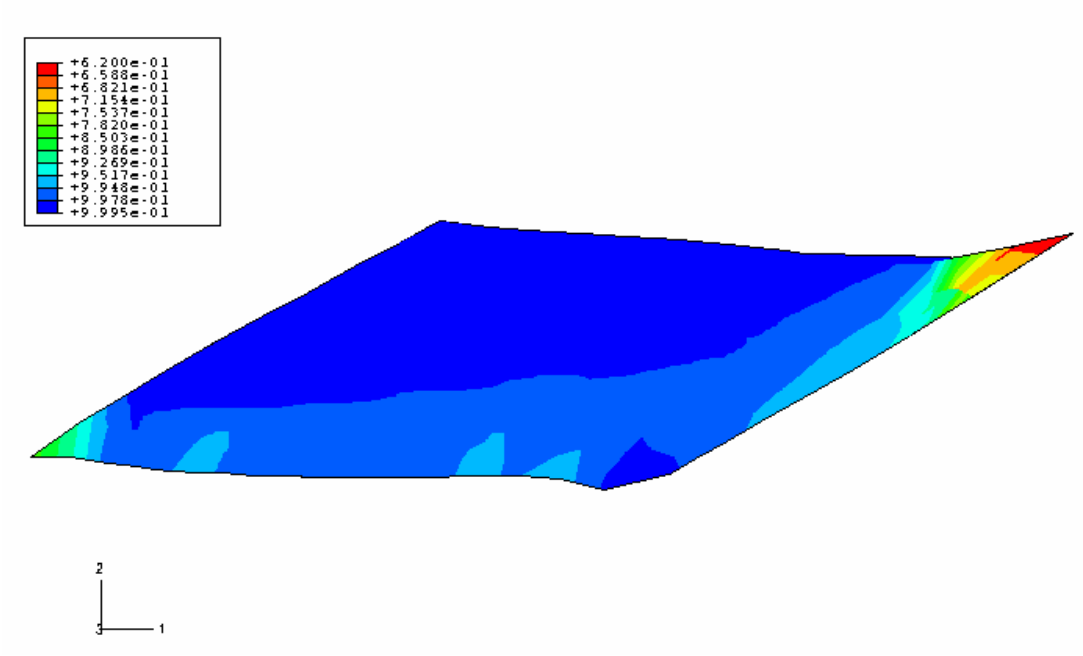

Fig 36. Relative density predicted by Duva and Crow model. The dark blue regions are fully consolidated and the red region shows least consolidation.

From the Figures 34, 35 and 36, it can be seen that the bottom portion of the powder does not fully consolidate. To further study this phenomenon and make comparisons of the stresses in the top and bottom parts of the powder in the can, we select two respective elements: one from the top (element A) and another from the bottom (element B) from the powder space, as shown in Figure 37. For these two elements, using the Duva and Crow model, we plot the stresses and the porosity evolution as they undergo the extrusion. The positions of the two elements at various process times are shown in Figure 38.

From Figures 39A and 39B, it is clear that the magnitude of hydrostatic pressure developed before passing through the corner in element A is much higher

than the hydrostatic pressure in element B (maximum of 550 MPa compared to 350 MPa). Thus the densification rate is higher in the element A. Also it can be seen that in element B, the powder undergoes very little densification even after it has passed through the corner. The difference in the hydrostatic pressure between elements A and B can be attributed to bending of the can when passing through the bend. Several strategies could be employed to reduce this difference, for example, use of a can of stiffer material, back pressure etc. This simulation will be used as a benchmark to evaluate the effect of changing the ECAE process parameters on the densification behavior.

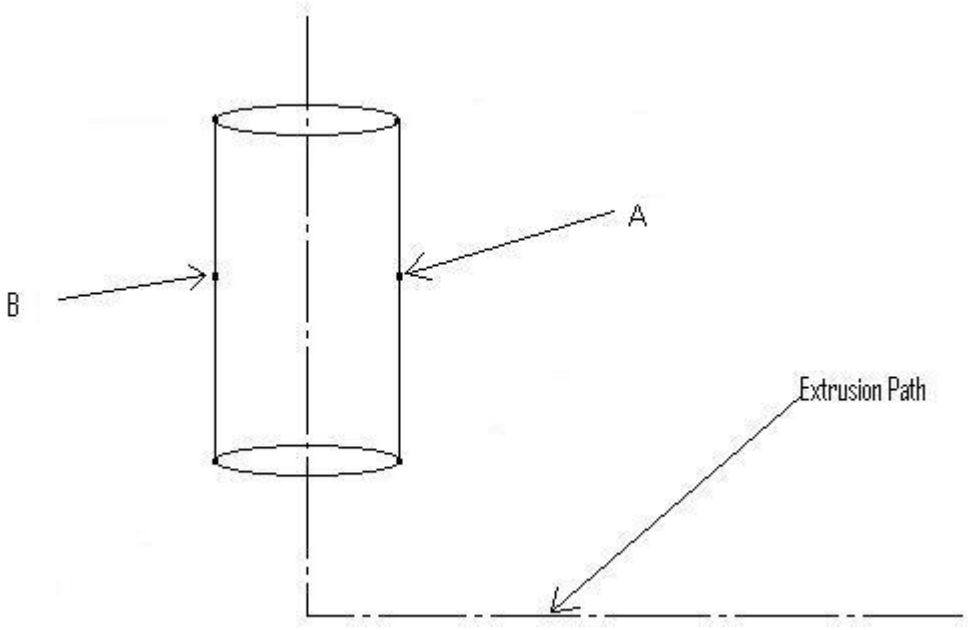

Fig 37. Elements A and B selected for studying the stresses developed in the lower and upper regions.

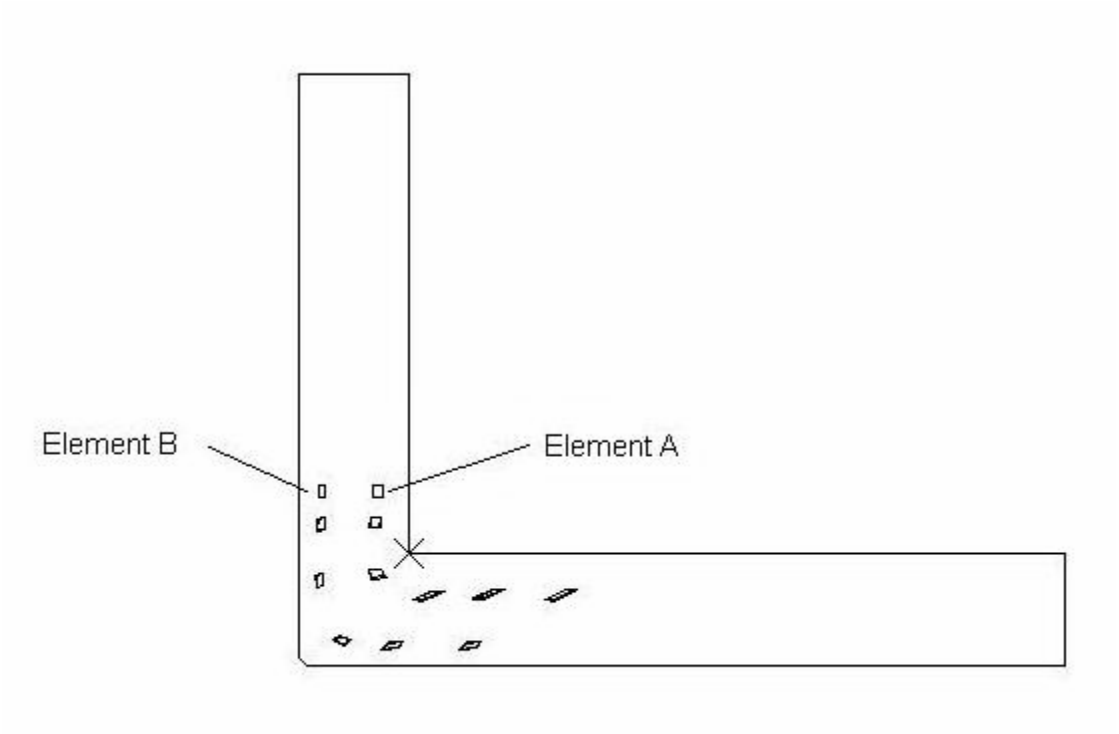

Fig 38. Position of elements A and B at scaled times 1, 6, 12, 18, 24, 30. T=1 shows the elements as the extrusion starts and T=30 shows the elements when the can is fully extruded.

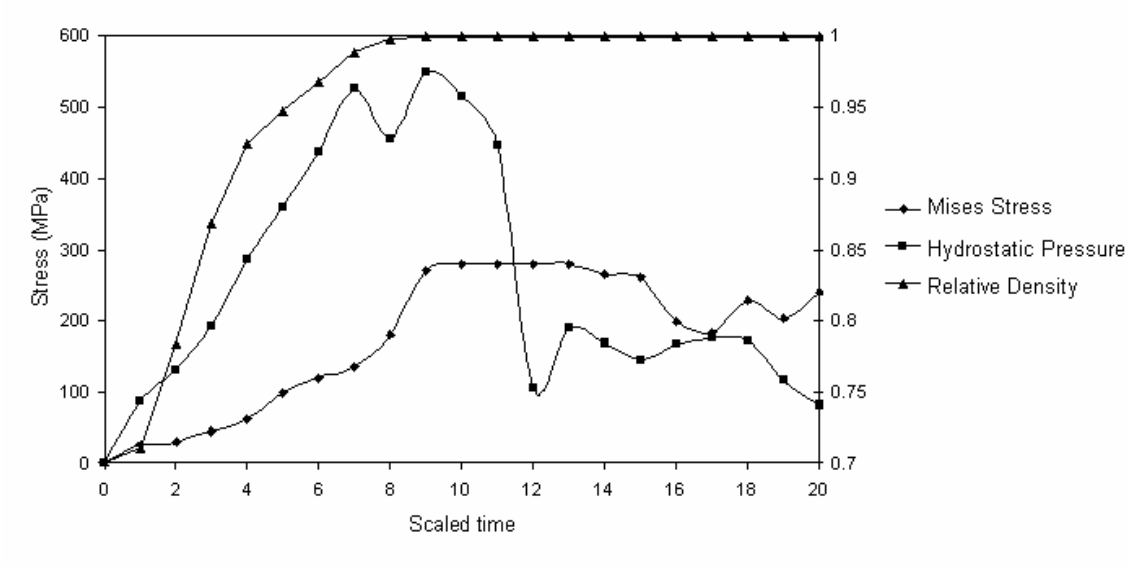

A

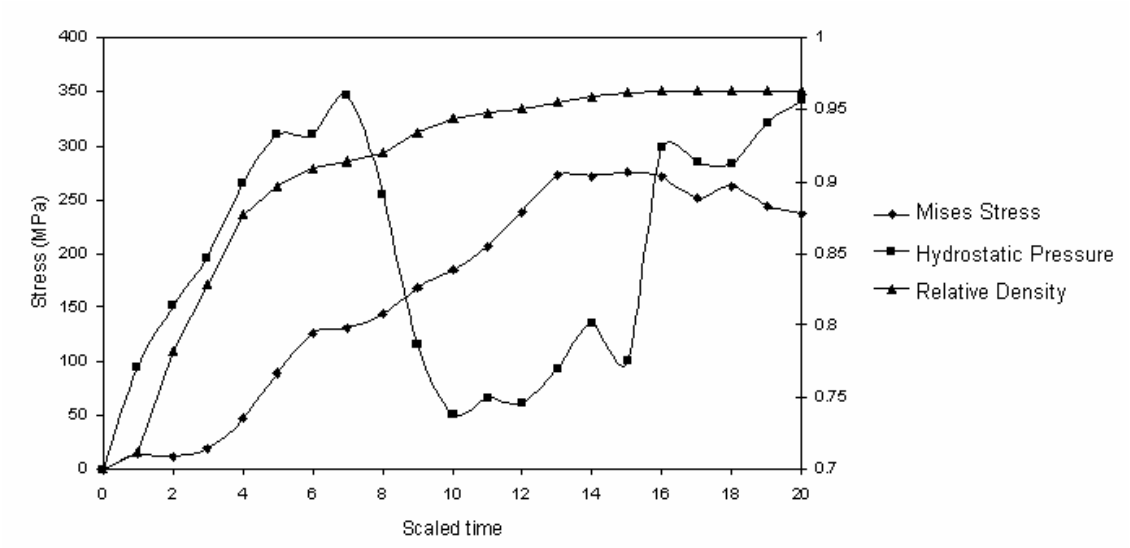

B

Fig 39. Mises stress, hydrostatic pressure (negative mean normal stress) and relative density for A) element A and B) element B. It can be seen that a high hydrostatic pressure is developed before the element passes through the bend, resulting in most of the consolidation.

At this stage, it would be appropriate to introduce a systematic method to measure the amount of densification and the variation in the densification over the powder compact. For this, we select four rows of elements in the powder region along the mid section, marked sections I, II, III and IV, as shown in Figure 40 and calculate the mean relative density over those elements as a measure of the extent of densification. To give an idea of the variation, we calculate the percentage of elements that are below the mean relative density. For the simulation presented in Figure 36, the mean RD over the 4 sections is shown in Figure 41.

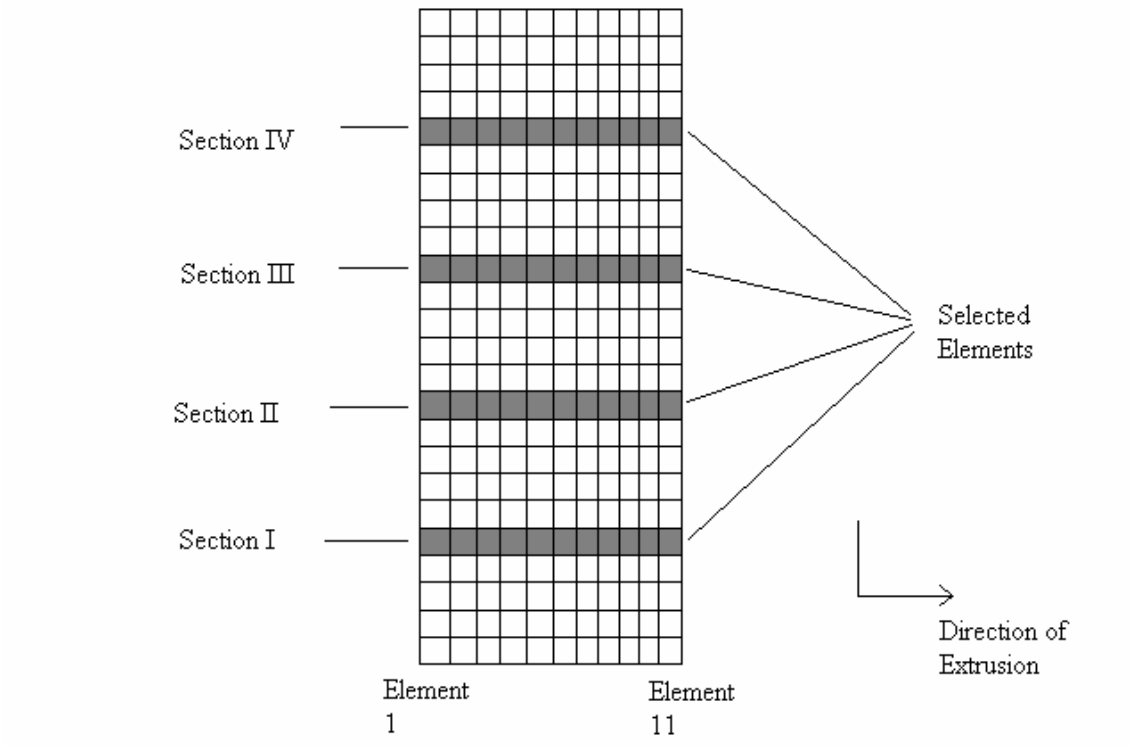

Fig 40. Figure showing the elements selected to study the uniformity and extent of densification over the compacted powder region.

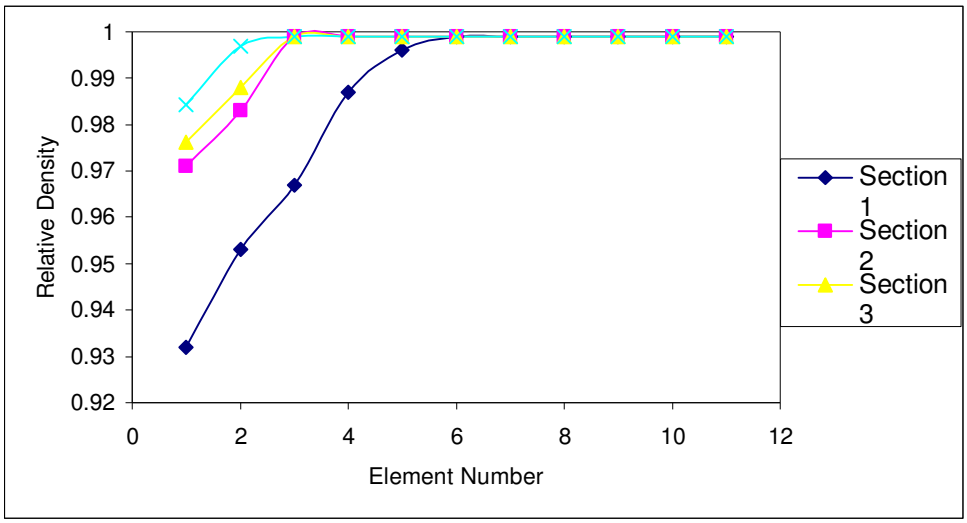

Fig 41. Variation of relative density after extrusion for elements shown in figure 40. The elements of the leading end at the bottom consolidate the least.

V.2.1. Simulations with back pressure on the lower half of exit channel

From the results discussed above, it is clear that the lack of compaction in the lower portion of the powder may be because of the lower hydrostatic pressure levels developed in this region. To overcome this, application of back pressure could give adequate hydrostatic pressure to the material in the lower region for complete compaction. The approach to apply back pressure should be chosen in such a way that it is experimentally feasible to apply and leads to the desired results. For this reason a constant back pressure of 200 MPa (which is equal to the difference in the hydrostatic pressure between elements A and B) is applied to the lower region of the workpiece which is schematically shown in Figure 42.

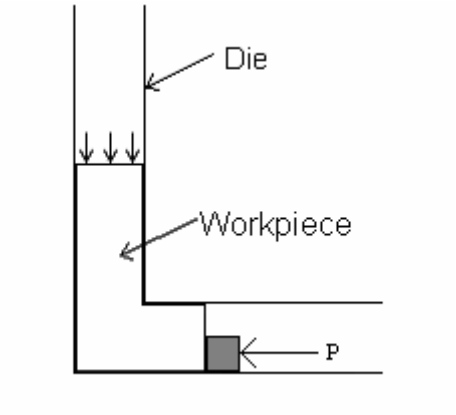

Fig 42. Schematic showing the application of a back pressure to the lower region of the workpiece during extrusion.

Figure 43 shows the result of the simulation performed using the Duva and Crow model with back pressure applied. It is clear that the powder at the bottom region is fully compacted now as compared to Figure 36, which is the simulation without back pressure. It can also be seen that the bottom portion of the leading edge of the compacted region is pushed back because of the back pressure as compared to the simulation without back pressure shown in Figure 36.

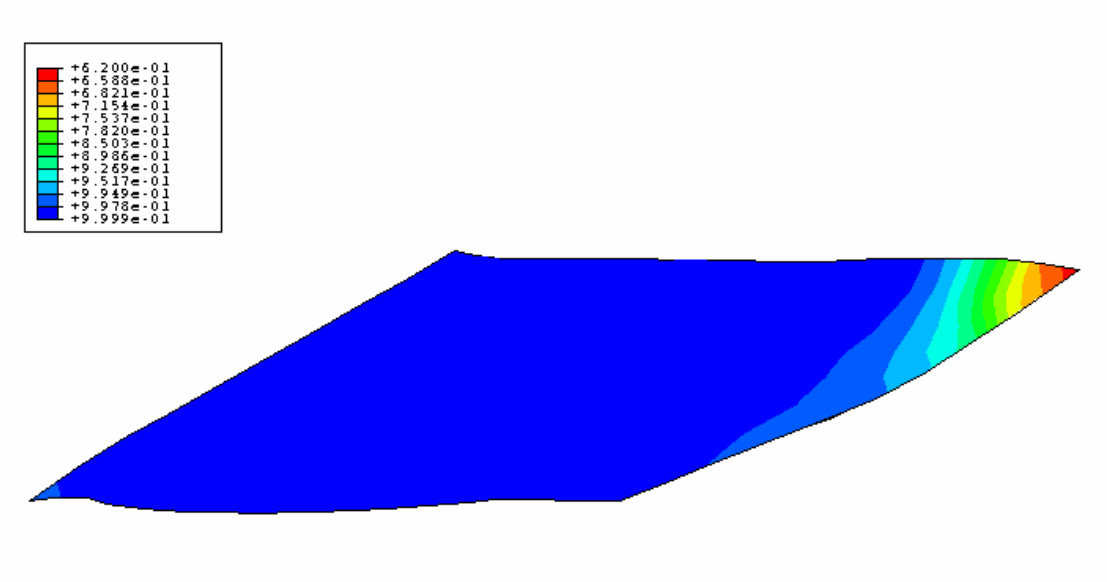

Fig 43. Relative density predicted by Duva and Crow model for ECAE with back pressure. The dark blue regions are fully consolidated and the red region shows least consolidation. It should be noted that we get improved consolidation in the bottom region.

To study the evolution of the stresses in the bottom region, the element B is selected and the stress components are plotted in Figure 44. The hydrostatic pressure developed is not significantly higher than the simulation without back pressure (Figure 36). But the drop in hydrostatic pressure after passing through the corner is significantly reduced, which results in continued compaction after passing through the corner zone.

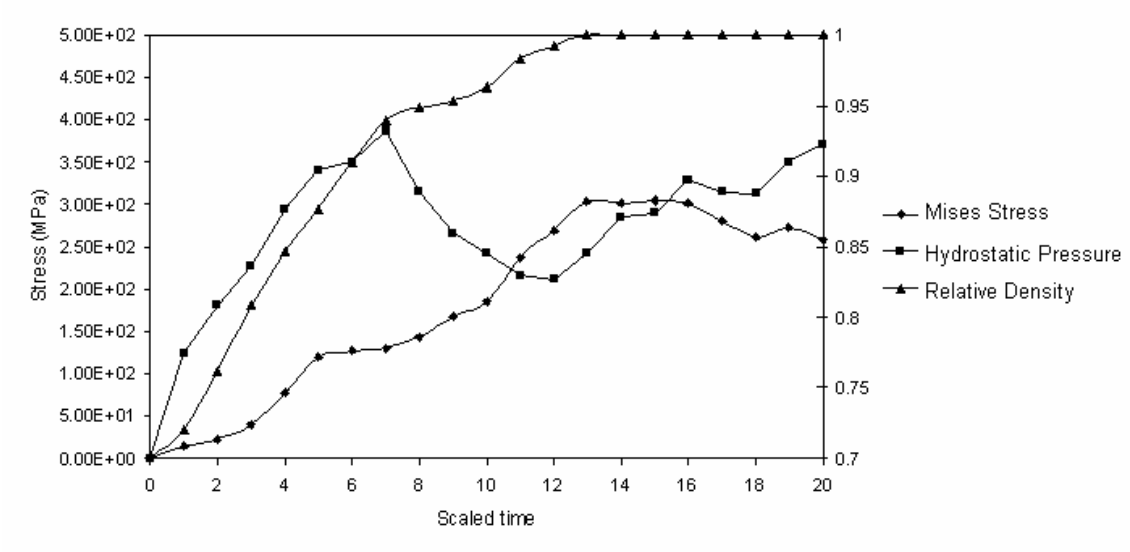

Fig 44. Mises stress, hydrostatic pressure (negative mean normal stress) and relative density for element B with back pressure. It can be seen that the drop in hydrostatic pressure after passing through the bend is not as significant here as it is without back pressure, resulting in better compaction.

V.2.2. Comparison of loads to compact the powder through ECAE vs. loads through pure compression

At this stage we would like to make a remark on the maximum loads required to carry out the compaction of the powder. In this section, maximum loads required for 3 methods are compared. 1) ECAE without back pressure, 2) ECAE with back pressure and 3) uniaxial compression. The loads required for the former 2 processes are readily available through the simulations carried out, as described in the previous sections. For the 3rd process, a routine simulation is carried out, using the Duva and Crow constitutive model for a powder material with the same dimensions as the powder extruded in the can during ECAE.

The maximum load required to carry out the ECAE without back pressure is 298.2 KN. The load during the ECAE with back pressure is 362.4 KN. The load required to compact the powder through compression is 478.7 KN. This shows that the loads required to compact the powder through ECAE are significantly lower than those required during compression.

V.2.3. Simulations with back pressure on the full face in the exit channel

The scheme adopted in the previous section is not feasible practically in the experiments. Thus a simulation was run to see the effect of a lower (70MPa) back pressure on the full face of the exit channel. Figure 45 shows the cross section of the extruded powder. From Figure 45, we can see that the powder compacts almost completely in the whole region on application of back pressure.

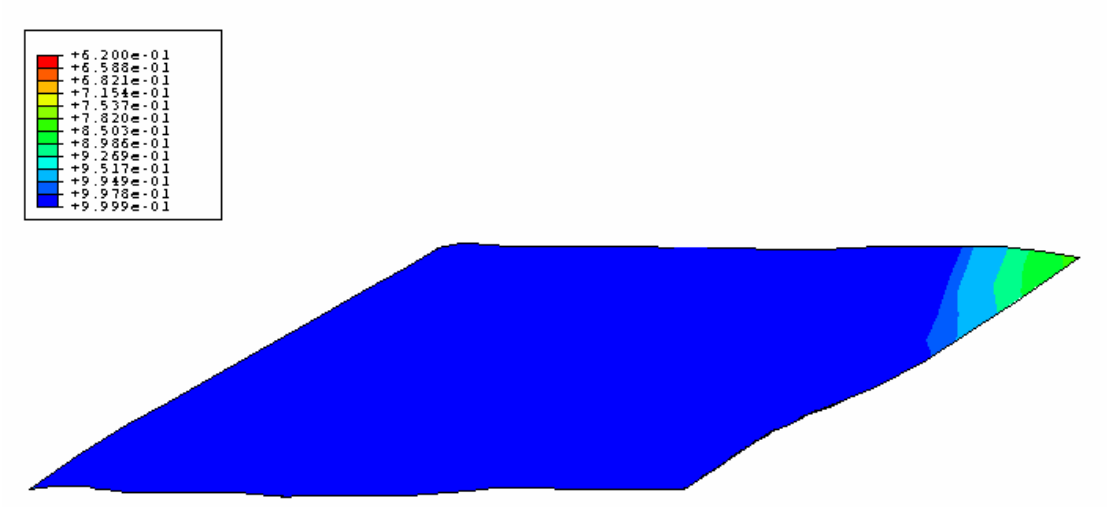

Fig 45. Relative density predicted by Duva and Crow model for ECAE with back pressure. The dark blue regions are fully consolidated and the red region shows least consolidation. It should be noted that we get improved consolidation in the bottom region.

V.2.4. Effect of friction

Simulations are carried out for four different coefficients of friction viz. 0, 0.03, 0.05 and 0.08 between the die and the can walls. These simulations reveal that the compaction behavior depends on the coefficient of friction. Figure 46 shows the minimum relative density among the selected elements plotted versus the friction coefficient used. This shows that the compaction achieved improves with higher friction values applied. Figures 47-A, B and C represent the variation of the relative density after extrusion for the elements selected in Figure 40.

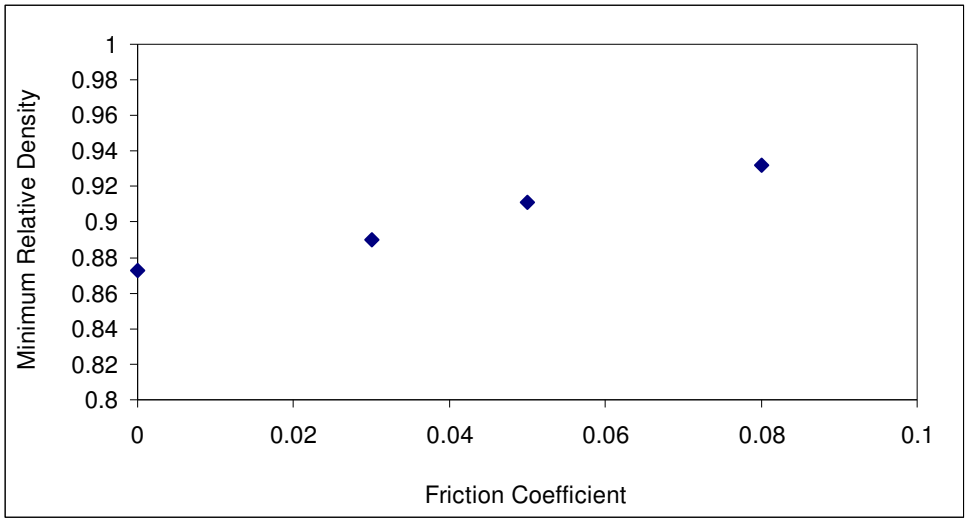

Fig 46. The minimum relative density over the selected elements plotted versus the coefficient of friction used for the simulations.

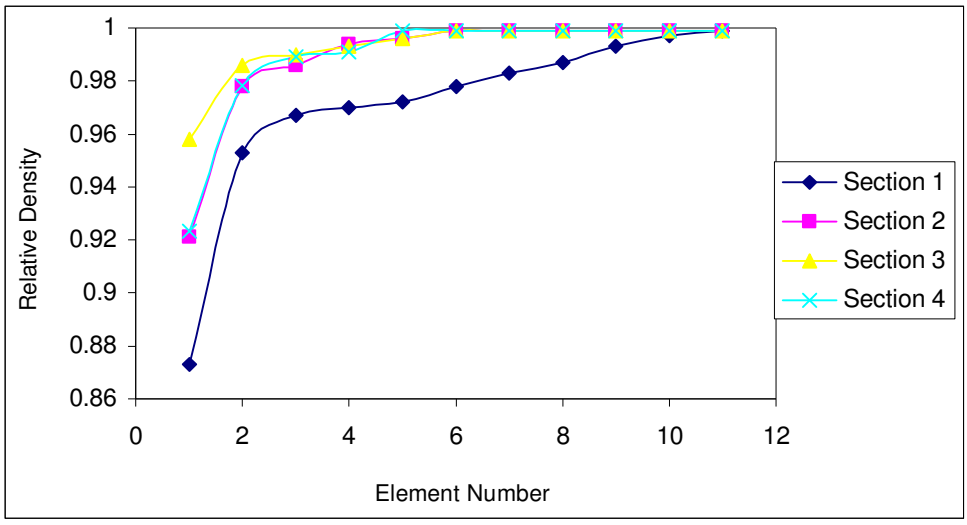

A

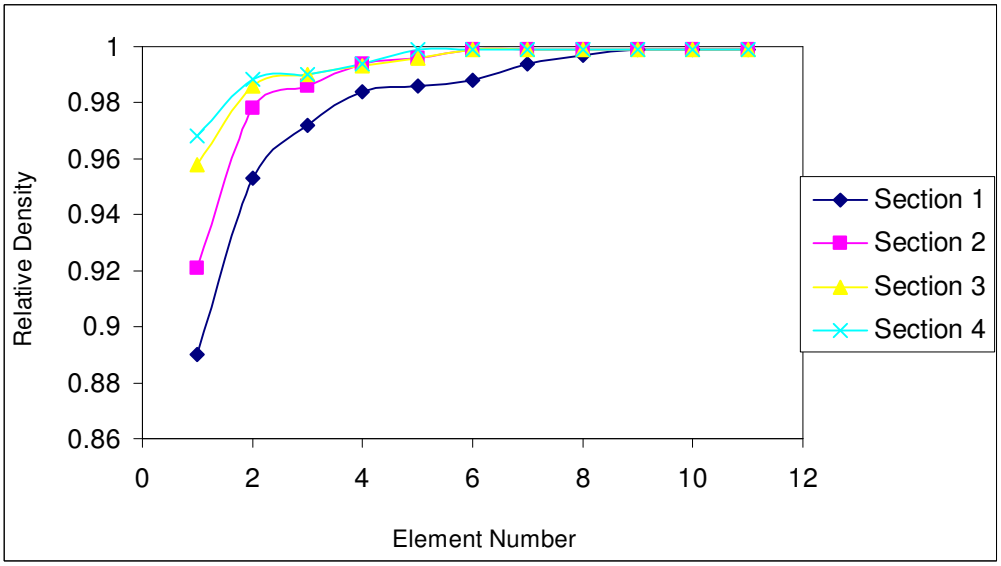

B

Fig 47. Variation of relative density after extrusion for elements shown in figure 40. A) friction coefficient= 0, B) friction coefficient= 0.03, C) friction coefficient= 0.05.

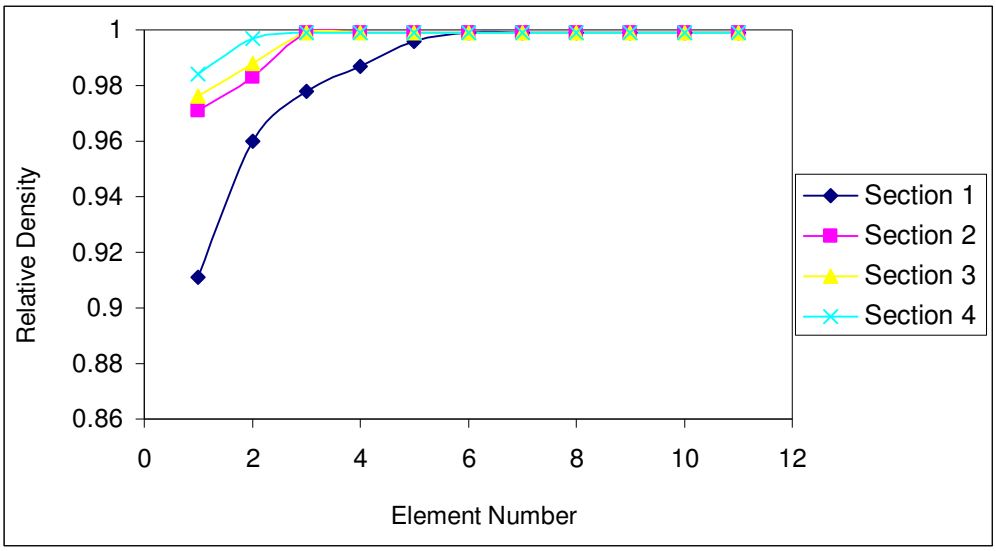

C

Fig 47. Continued.

V.2.5. Can with thicker base

The key idea behind having a thicker base for extruding powder is that the base would provide extra stiffness and thus could induce better compaction of the powder. Figure 48 shows the powder compacted with the thicker base. From Figure 48, we can see that the compaction behavior does not improve significantly by increasing the thickness of the base. To study this, we look at the compaction profiles using the method described earlier. The plots for relative density along the four rows of elements are shown in Figure 49, and it can be seen that the consolidation is not a significant improvement over extrusion through a regular can.

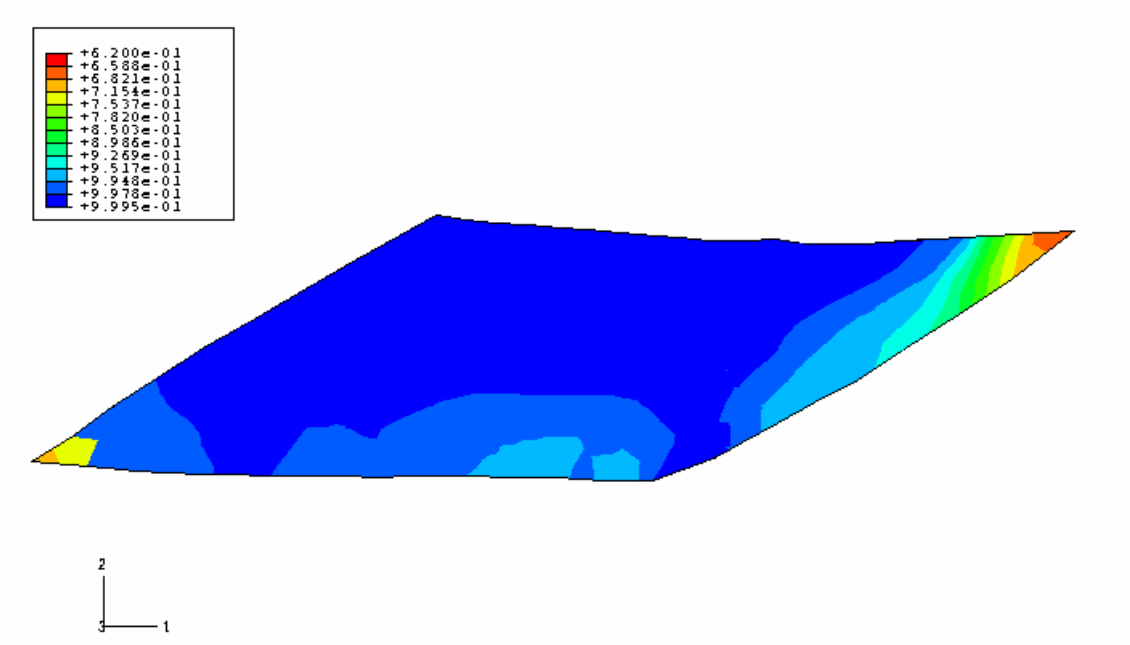

Fig 48. Relative density predicted by Duva and Crow model for ECAE using a can with a thicker base. The dark blue regions are fully consolidated and the red region shows least consolidation.

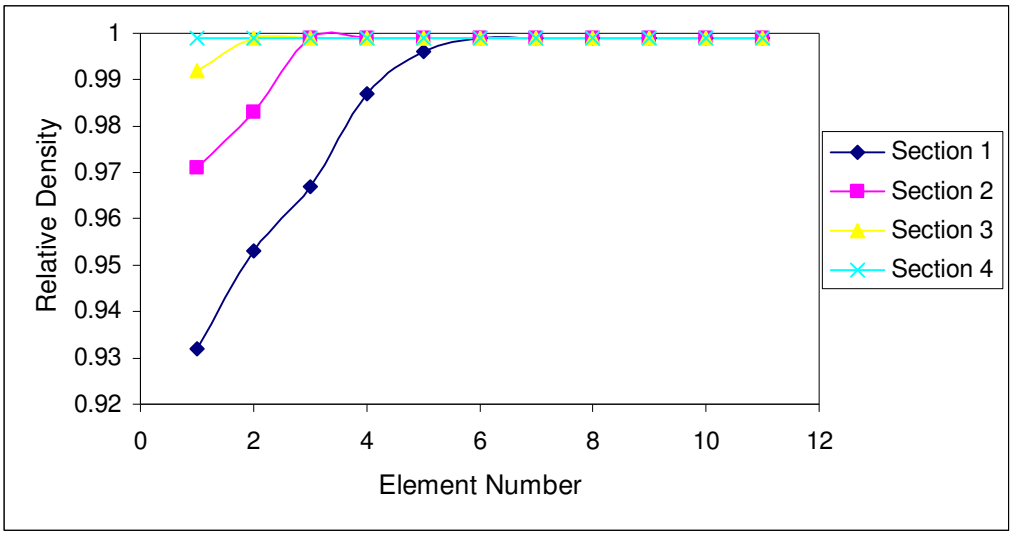

Fig 49. Variation of relative density after extrusion for elements shown in figure 40. for simulation with a can having thicker base. Series 1 corresponds to section 1, series 2 to section 2 and so on.

V.2.6. Can with thicker walls

The can is made of a square cross section with a circular hole in it. The square is of side 2.5 cm and the diameter of the hole is 2 cm. In this simulation, the diameter of the hole was kept at 1.5 cm. Figure 50 shows the cross section of the compacted powder. The Mean relative density over the selected elements is .998 and is a considerable improvement over the extrusion through the regular can.

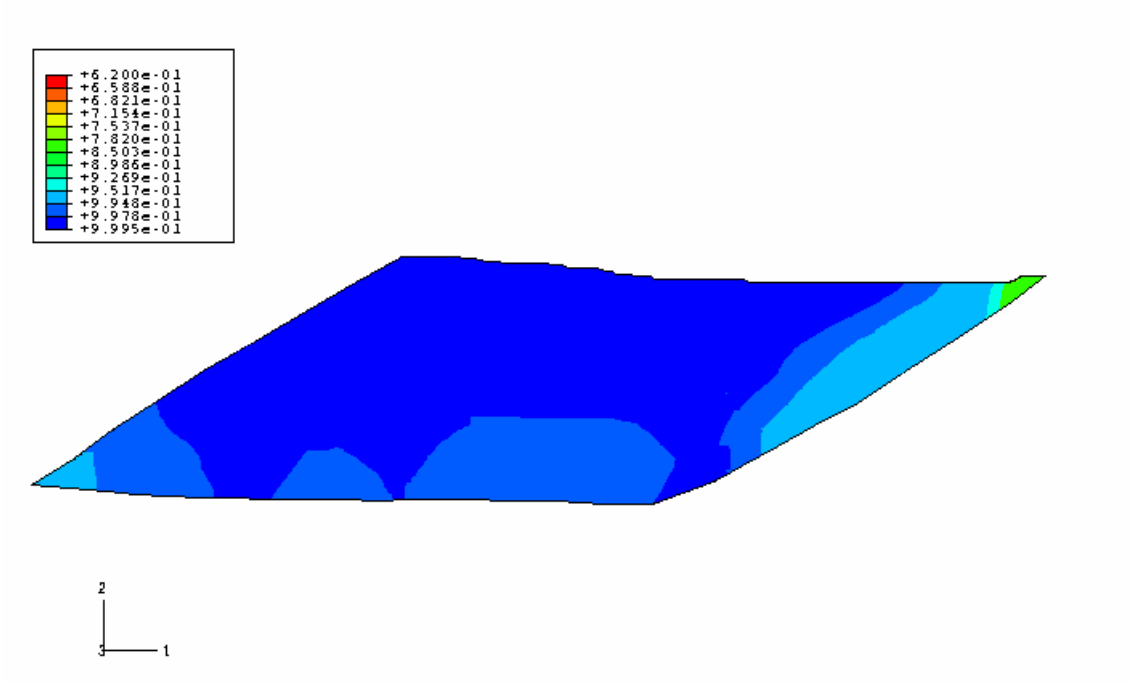

Fig 50. Relative density predicted by Duva and Crow model for ECAE using a can with thicker walls. The dark blue regions are fully consolidated and the red region shows least consolidation. It should be noted that we get improved consolidation in the bottom region.

V.2.7. Results for simulations run with Nickel can

Nickel was chosen as a second can material in this work because of its high yield strength. From Figure 51, we see that the powder extruded in a Nickel can compacts completely. The mean Relative density for the selected elements is 1.

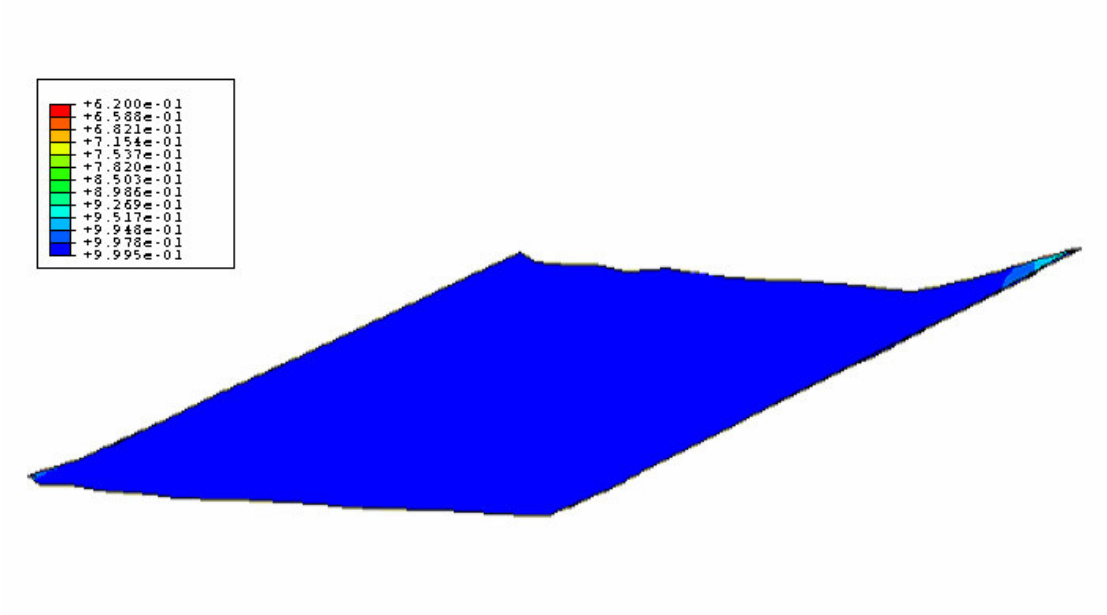

Fig 51. Relative density predicted by Duva and Crow model for ECAE with Nickel can. The dark blue regions are fully consolidated and the red region shows least consolidation. It should be noted that we get complete compaction over the whole powder region.

V.2.8. Simulations for long can

In this section, a long can of length 20 cm with a cylindrical hole of length 15 cm is simulated. This simulation can show the effect of the compression occurring in the entry channel before the powder passes through the corner. Figure 52 shows the cross section of the extruded powder material.

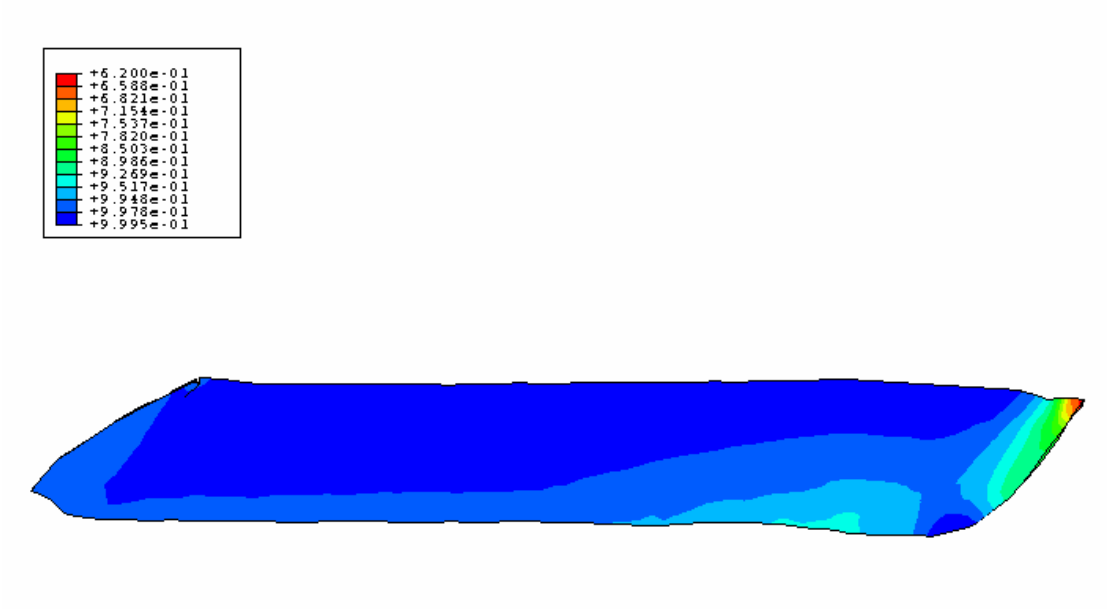

Fig 52. Contour for the distribution of relative density over the extruded powder predicted by Duva and Crow model. It can be seen that the powder in the trailing end compacts much better than the powder in the leading end.

V.2.9. Simulations with changing cross head velocity

Three cross head velocities were considered in the simulations viz. 10 mm/s, 2.5 mm/s and .5 mm/s. The effect of changing the cross head velocity is discussed here. Figure 53 shows the minimum relative density among the selected elements plotted versus the cross head velocity used. This shows that the compaction achieved improves with slower extrusion speeds. Also for the selected elements, the relative density distribution is shown in Figures 54-A and 54-B for velocities 10 mm/s, and .5 mm/s respectively.

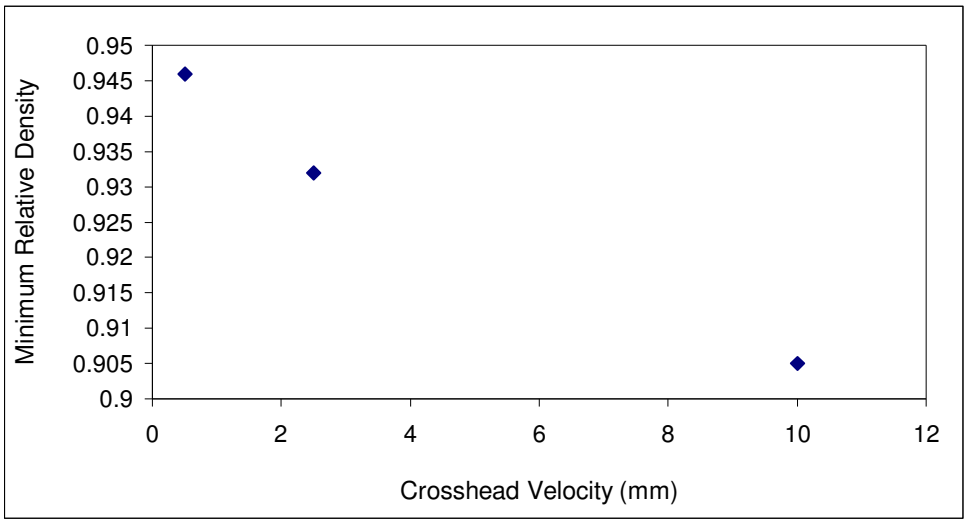

Fig 53. Minimum relative density after extrusion among the elements selection shown in figure 40. It can be seen that increasing the crosshead velocity causes a reduction in the overall compaction of the powder.

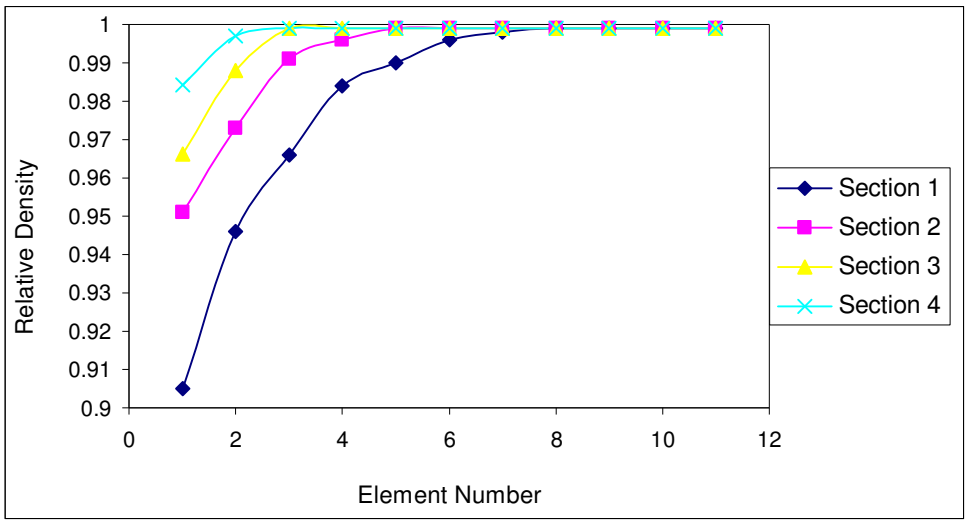

A

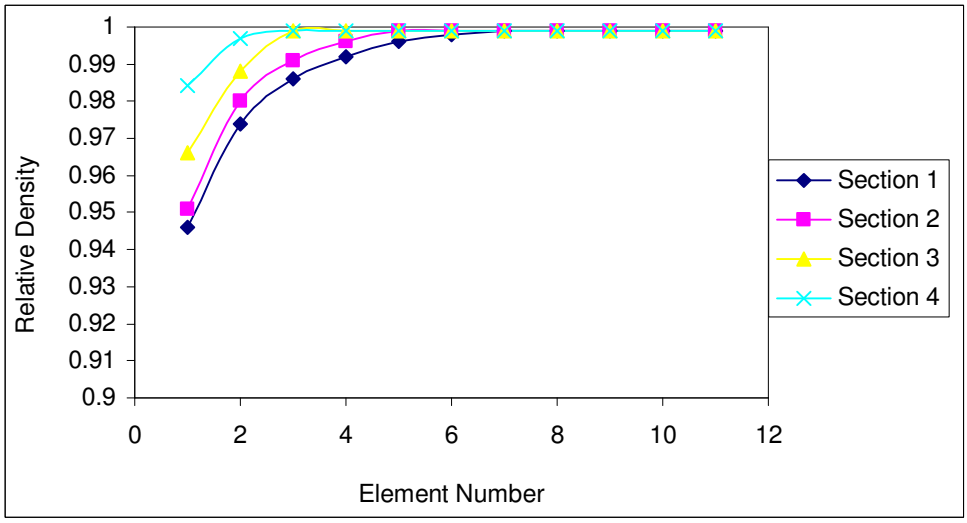

B

Fig 54. Variation of relative density after extrusion for elements shown in figure 40. A) cross head velocity of 10 mm/s and B) crosshead velocity of 0.5 mm/s.

V.2.10. Simulation with a circular can

In this simulation, a can of circular cross-section, instead of a square cross section is used. The outer diameter of the can is 2.5 cm with a hole of 2 cm diameter at the center, which is filled with the powder. Figure 55 shows the cross section of the extruded powder. To analyze the compaction behavior, the relative density of the selected elements is plotted in Figure 56. It can be seen that the circular can creates much more non-uniform densification in the powder material. Also the mean relative density over the selected elements is .9705, which is much lower than the average compaction achieved in the square can.

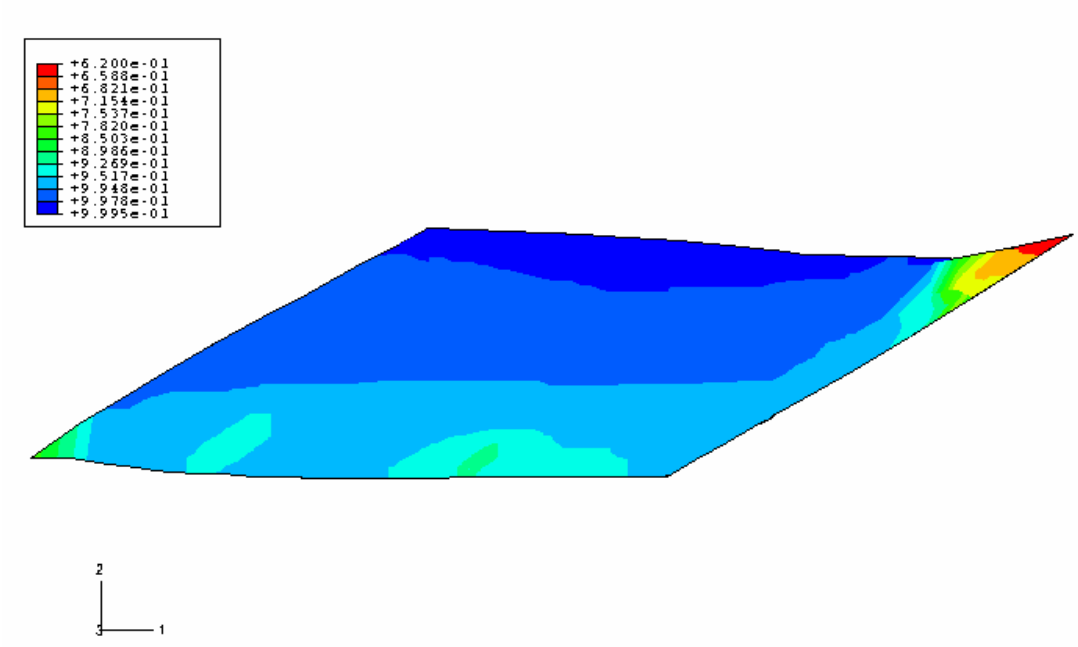

Fig 55. Contour for the compacted powder obtained through simulation using a circular can.

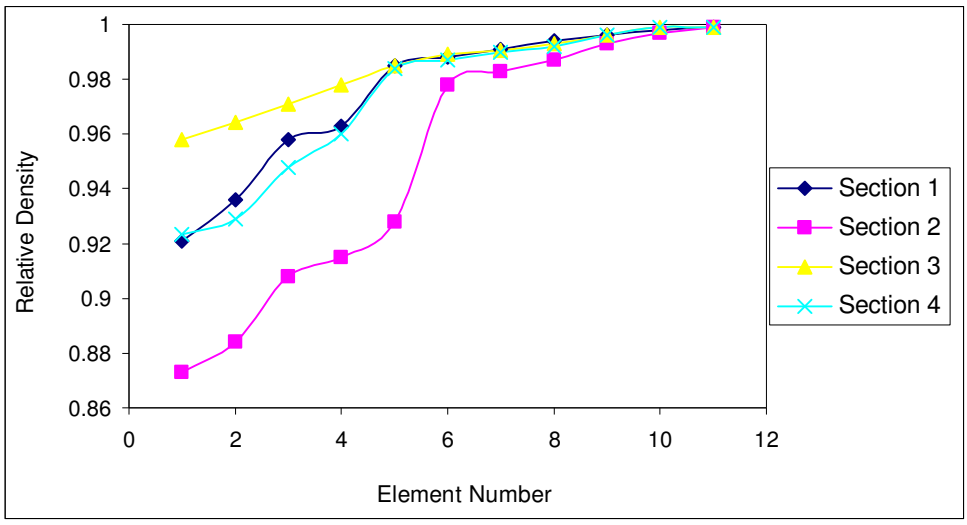

Fig 56. Variation of relative density after extrusion for elements shown in figure 40, obtained for simulation using a circular can. Notice that the minimum density is observed near the center of the can unlike the square can where it was at the leading edge.

CHAPTER VI

DISCUSSION AND CONCLUSIONS

The results discussed in chapter V are summarized here and a brief sensitivity analysis is carried out. The key results presented in table 3 are the extent of densification, the uniformity of densification and the loads required to carry out the extrusion. The minimum relative density observed over the chosen elements is selected as a measure for the extent of densification. The loads are computed directly from the simulation as the sum of loads applied on the elements on the top surface which is given the downward displacement for extrusion.

To compute a measure of the non-uniformity of extrusion, the difference between the maximum relative density and the minimum relative density observed over the selected elements is computed. Also the mean of the relative densities over these elements is computed. The number of elements that have final relative density that differ from the mean by more than 10% of the aforementioned maximum difference is counted and is represented as a percentage of the total number of selected elements, which is 44. As an example, for the case of frictionless extrusion with a square can, the mean relative density is .988, the maximum relative density is 1 and the minimum is .873. The elements with relative density either less than .9753 or greater than 1.0007 (which is impossible since the maximum relative density achievable is 1) are counted.

The number if such elements is 16, the percentage is computed as 36.36 and is presented here as the non-uniformity measure.

Using the data in table 3, sensitivity analysis is carried out. As a measure of the sensitivity, the value of $\frac{dy}{dx}\frac{x}{y}$ is computed at each data point for the curves drawn with the process parameter (for example the relative density) on the X-axis and the result parameter (for example the load) on the Y-axis. The computed sensitivity parameters are shown in table 4.

In the data representation, the parameters need to be quantified. Parameters like friction coefficient, cross head velocity, can dimensions, back pressure are already available as numbers. To characterize the material, its initial yield stress was used as the parameter.

To characterize the shape of the cross section of the can, the ratio of maximum distance of the can cross section to the minimum distance from the center was calculated. For example, for a square can if side 2.5 cm with center hole of diameter 2 cm, the maximum distance from the center is 1.25^2 = 1.5625 cm and the minimum distance is 1 cm. Therefore the computed ratio is 1.5625. For a circular can of outer diameter 2.5 cm with inner hole of diameter 2 cm, the ratio is 1.25.

Table 3. Data from extrusions for extent of densification, uniformity of densification and the loads for various parameters

Friction Coefficient	**Minimum RD**	**Load (Mpa)**	**Non-Uniformity measure**
0	0.873	239.8	36.36
0.03	0.89	251.3	25
0.05	0.911	272.9	15.9
0.08	0.932	298.2	13.63
Crosshead velocity (mm/s)			
0.5	0.946	302.1	9.09
2.5	0.932	298.2	13.63
10	0.905	293.8	15.9
Back Pressure (Mpa)			
0	0.932	298.2	13.63
70	1	349.7	0
Back pressure on lower half of exit channel (Mpa)			
0	0.932	298.2	13.63
200	1	362.4	0
Can material (Initial yield strength, MPa)			
Copper 80	0.932	298.2	13.63
Nickel 300	1	403.6	0
Can section (dmax/dmin)			
Circular Section 1.25	0.873	241.8	45.45
Square section – Thin wall 1.5625.	0.932	298.2	13.63
Square section - Thick Wall 2.0833.	0.992	303.6	4.54
Base Thickness (mm)			
2.5	0.932	298.2	13.63
5	0.938	300.1	11.36

Table 4. Sensitivity values for minimum relative density, non-uniformity of densification and the loads for various parameters

Friction Coefficient	**Minimum RD**	**Load**	**Non-Uniformity**
0	0	0	0
0.03	0.019101	0.045762	-0.4544
0.05	0.057629	0.197875	-1.43082
0.08	0.060086	0.226246	-0.44412
Crosshead velocity (mm/s)			
0.5	-0.0037	-0.00323	0.124862
2.5	-0.00966	-0.00492	0.055515
10	-0.03978	-0.01997	0.190356
Back Pressure (Mpa)			
0	0	0	0
70	0.068	0.147269	NA
Back pressure on lower half of exit channel (Mpa)			
0	0	0	0
200	0.068	0.177152	NA
Can material (Initial yield strength, MPa)			
80	0.026531	0.128529	-0.36364
300	0.092727	0.356113	NA
Can section (dmax/dmin)			
Circular Section 1.25	0.270332	0.933002	-2.80044
Square section – Thin wall 1.5625	0.193145	0.054329	-2.00086
Square section - Thick Wall 2.0833	0.241947	0.07115	-8.0092
Base Thickness			
2.5	0.006438	0.003916	-0.16654
5	0.012793	0.012662	-0.39965

From these tables some key conclusions can be drawn on the effect of the design parameters on the densification behavior of the extruded powder. It is seen that by increasing the friction coefficient, both the uniformity and the extent of densification improve. This improvement is seen maximum between friction coefficient values of .03 and .05. Also the loads remain within 25% of each other when friction is increased from 0 to 0.08.

The effects of changing the crosshead velocity are not as significant as the effect of changing friction, both on the densification and the loads.

Back pressure applied to the exit channel, either on the full face of the exiting workpiece or half the face, improves the consolidation. A back pressure of 70 MPa on full face of the exit channel is recommended for improved compaction.

Changing the can material from Copper to Nickel improved the compaction behavior immensely, but at the same time increased the extrusion loads by more than 35%. This method, though gives excellent results, is costly to implement (because of the cost of Nickel cans) and the increased load.

Using a can of circular section did not yield good results when compared to a square can. Both the extent of densification and the uniformity showed the least promise with the use of circular can of thin walls. It should be noted that no simulations were carried out for circular cans with thicker walls, which could have a detrimental effect on the densification. This is listed as a future work.

Changing the minimum thickness of the can from .25 cm to .5 cm improves the consolidation to almost perfect with the load increasing by only about 3%. This option

gave the best densification to load value but the yield of the compacted material decreases by 43.75%. Changing the thickness of the base had an almost negligible effect on the densification and the load.

To conclude, applying back pressure, changing the can wall thickness and using a can of stiffer material, all gave good results for the densification. But changing the can material is costly and increases the loads immensely. Changing the wall thickness decreases the material yield. Thus applying back pressure seems the optimal solution to achieve full densification, which is easy to implement and does not significantly increase the loads.

As future work, some key recommendations can be made. Development and implementation of a powder model involving diffusion would enable us to model the process at higher temperatures as the diffusion plays a major role at elevated temperatures. Also some other key design parameters like initial powder density and circular cans with varying thickness can be studied in further detail. A detailed parametric study by varying the back pressure conditions can be made to obtain the optimum back pressure which gives full densification. Full scale 3-D simulations for observing the effect of multiple passes on densification are another key goal to be achieved.

REFERENCES

Abaqus Inc., 2004. Abaqus Users Manual, Version 6.5: Abaqus Inc, Providence, RI.

Baik S.C., Estrin Y., Kim H.S., Hellmig R.J., 2003. Dislocation density-based modeling of deformation behavior of aluminium under equal channel angular pressing. Materials Science and Engineering a-Structural Materials Properties Microstructure and Processing 351 (1-2), 86-97.

Bakhshiani A., Khoei A.R., Mofid M., 2002. An endochronic plasticity model for powder compaction processes. Journal of Materials Processing Technology 125, 138-143.

Beyerlein I. J., Lebensohn R. A., Tome C. N., 2003. Modeling texture and microstructural evolution in the equal channel angular extrusion process. Materials Science and Engineering a-Structural Materials Properties Microstructure and Processing 345 (1-2), 122-138.

Beyerlein I. J., Li S., Necker C. T., Alexander D. J., Tome C. N., 2005. Non-uniform microstructure and texture evolution during equal channel angular extrusion. Philosophical Magazine 85 (13), 1359-1394.

Biswas K., 2005. Comparison of various plasticity models for metal powder compaction processes. Journal of Materials Processing Technology 166 (1), 107-115.

Bowen J.R., Gholinia A., Roberts S.M., Prangnell P.B., 2000. Analysis of the billet deformation behaviour in equal channel angular extrusion. Materials Science and

Engineering a-Structural Materials Properties Microstructure and Processing 287 (1), 87-99.

Carmai J., Dunne F. P. E. 2004. Generalised constitutive equations for densification of metal matrix coated fiber composites. Materials Science and Technology 20(4), 478-484.

Carmai J., Dunne F. P. E., 2005. A model for the consolidation of hexagonal array matrix coated fibre composites. Modelling and Simulation in Materials Science and Engineering 13(6), 1005-1014.

Carroll M. M., 1986. An empirical-model for hot isostatic pressing of metal powders. Metallurgical Transactions a-Physical Metallurgy and Materials Science 17 (11), 1977-1984.

Cocks A.C.F., 1989. Inelastic deformation of porous materials. Journal of the Mechanics and Physics of Solids 37 (6), 693-715.

Delo D. P., Piehler H. R., 1999. Early stage consolidation mechanisms during hot isostatic pressing of Ti-6Al-4V powder compacts. Acta Materialia 47 (9), 2841-2852.

Duva J. M., Crow P. D., 1992. The densification of powders by power-law creep during hot isostatic pressing. Acta Metallurgica Et Materialia 40 (1), 31-35.

Erb U., 1995. Electrodeposited Nanocrystals - synthesis, structure, properties and future applications. Canadian Metallurgical Quarterly 34 (3), 275-280.

Ferrasse S., Segal V. M., Hartwig K. T., Goforth R. E., 1997. Development of a submicrometer-grained microstructure in aluminum 6061 using equal channel angular extrusion. Journal of Materials Research 12 (5), 1253-1261.

Ferrasse S., Segal V. M., Hartwig K. T., Goforth R. E., 1997. Microstructure and properties of copper and aluminum alloy 3003 heavily worked by equal channel angular extrusion. Metallurgical and Materials Transactions a-Physical Metallurgy and Materials Science 28 (4), 1047-1057.

Flanagan D.P., Taylor L.M., 1987. An accurate numerical algorithm for stress integration with finite rotations. Computer Methods in Applied Mechanics and Engineering 62 (3), 305-320.

Gleiter H., 1989. Nanocrystalline materials. Progress in Materials Science 33 (4), 223-315.

Gurson A. L., 1977. Continuum theory of ductile rupture by void nucleation and growth: Part I—Yield criteria and flow rules for porous ductile materials. Journal of Engineering Materials and Technology 99, 2-15.

Haouaoui M., Karaman I., Maier H. J., Hartwig K. T., 2004. Microstructure evolution and mechanical behavior of bulk copper obtained by consolidation of micro- and nanopowders using equal-channel angular extrusion. Metallurgical and Materials Transactions a-Physical Metallurgy and Materials Science 35A (9), 2935-2949.

Harewood F.J., McHugh P.E., 2006. Investigation of finite element mesh independence in rate dependent materials. Computational Materials Science 37 (4), 442-453.

Hartwig K.T., Karaman I., Haouaoui M., Mathaundu S.N., 2003. Consolidation of Cu and amorphous Zr-based powders by severe plastic deformation. 2003 NATO Advanced Research Workshop on “Metallic Materials with High Structural Efficiency”, 6-13.

Hartwig K.T., Zapata H., Parasiris A., Mathaundu S.N., 2001. Consolidation of metallic powders by equal channel angular extrusion. Powder Materials: Current Research and Industrial Practices Symposium. 211-221.

Hughes T.J.R., Winget J., 1980. Finite rotation effects in numerical-integration of rate constitutive-equations arising in large-deformation analysis. International Journal for Numerical Methods in Engineering 15 (12) 1862-1867.

Iwahashi Y., Horita Z., Nemoto M., Langdon T. G., 1997. An investigation of microstructural evolution during equal-channel angular pressing. Acta Materialia 45 (11), 4733-4741.

Iwahashi Y., Horita Z., Nemoto M., Langdon T. G., 1998. The process of grain refinement in equal-channel angular pressing. Acta Materialia 46 (9), 3317-3331.

Kaculi X., Srinivasan. M.N., Hartwig K.T., 2003. Use of high intensity milling and ECAE to produce and consolidate nanostructured TiSi. 2003 ASME International Mechanical Engineering Congress and Exposition, Washington, DC. p 4229-4236.

Karaman I., Robertson J., Im J. T., Mathaudhu S. N., Luo Z. P., Hartwig K. T., 2004. The effect of temperature and extrusion speed on the consolidation of zirconium-based metallic glass powder using equal-channel angular extrusion. Metallurgical and Materials Transactions a-Physical Metallurgy and Materials Science 35A (1), 247-256.

Karaman I., Haouaoui M., Maier H. J., 2007. Nanoparticle consolidation using equal channel angular extrusion at room temperature. Journal of Materials Science 42 (5) ,1561-1576.

Kim H.S., Seo M.H., Hong S.I., 2000. On the die corner gap formation in equal channel angular pressing. Materials Science and Engineering a-Structural Materials Properties Microstructure and Processing 291 (1-2), 86-90.

Kim H.S., Seo M.H., Hong S.I., 2001. Plastic deformation analysis of metals during equal channel angular pressing. Journal of Materials Processing Technology 113 (1-3), 622-626.

Kim H.S., 2001. Finite element analysis of equal channel angular pressing using a round corner die. Materials Science and Engineering a-Structural Materials Properties Microstructure and Processing 315 (1-2), 122-128.

Kim H.S., Seo M.H., Hong S.I., 2002. Finite element analysis of equal channel angular pressing of strain rate sensitive metals. Journal of Materials Processing Technology 130, 497-503.

Kim H. S., Seo M. H., Oh C. S., Kim S. J., 2003. Equal channel angular pressing of metallic powders. Advanced Materials Processing Ii 437 (4), 89-92.

Kim K. T., Carroll M. M., 1987. Compaction equations for strain-hardening porous materials. International Journal of Plasticity 3 (1), 63-73.

Kim K. T., Suh J., 1990. Model for hot compaction of metal powders. Powder Metallurgy 33 (1), 40-44.

Li S., Bourke M. A. M., Beyerlein I. J., Alexander D. J., Clausen B., 2004. Finite element analysis of the plastic deformation zone and working load in equal channel angular extrusion. Materials Science and Engineering a-Structural Materials Properties Microstructure and Processing 382 (1-2), 217-236.

Liu Z.Y., Gang L., Wang Z.R., 2000. Finite element simulation of a new deformation type occurring in changing-channel extrusion. Journal of Materials Processing Technology 102 (1-3), 30-32.

Luis C.J., Garces Y., Gonzalez P., Berlanga C., 2002. FEM analysis of equal channel angular processes. Materials and Manufacturing Processes 17 (2), 223-250.

Luis-Perez C. J., Luri-Irigoyen R., Gaston-Ochoa D., 2004. Finite element modelling of an Al-Mn alloy by equal channel angular extrusion (ECAE). Journal of Materials Processing Technology 153 (54), 846-852.

Matsuki K., Aida T., Takeuchi T., Kusui J., Yokoe K., 2000. Microstructural characteristics and superplastic-like behavior in aluminum powder alloy consolidated by equal-channel angular pressing. Acta Materialia 48 (10), 2625-2632.

Meyers M.A., Mishra A., Benson D.J., 2006. Mechanical properties of nanocrystalline materials. Progress in Materials Science 51 (4), 427-556.

Nagasekhar A.V., Tick-Hon Y., 2004. Optimal tool angles for equal channel angular extrusion of strain hardening materials by finite element analysis. Computational Materials Science 30(3-4), 489-495.

Oh S. J., Kang S. B., 2003. Analysis of the billet deformation during equal channel angular pressing. Materials Science and Engineering a-Structural Materials Properties Microstructure and Processing 343 (1-2), 107-115.

Olovsson L., Simonsson K., Unosson M., 2005. Selective mass scaling for explicit finite element analyses. International Journal for Numerical Methods in Engineering 63 (10), 1436-1445.

Oruganti R. K., Subramanian P. R., Marte J. S., Gigliotti M. F., Amancherla S., 2005. Effect of friction, back pressure and strain rate sensitivity on material flow during equal channel angular extrusion. Materials Science and Engineering a-Structural Materials Properties Microstructure and Processing 406 (1-2), 102-109.

Parasiris A., Hartwig K. T., Srinivasan M. N., 2000. Formation/consolidation of WC-Co cermets by simple shear. Scripta Materialia 42 (9), 875-880.

Parasiris A., Hartwig K.T., 2000. Consolidation of advanced WC-Co powders. International Journal of Refractory Metals & Hard Materials 18 (1), 23-31.

Pei Q.X., Hu B.H., Lu C., Wang Y.Y., 2003. A finite element study of the temperature rise during equal channel angular pressing. Scripta Materialia 49 (4), 303-308.

Pearson J., 1997. Master's Thesis. Consolidation of Al 6061 powder by ECAE. Texas A&M University, College Station.

Perez C.J.L., Berlanga C., Perez-Ilzarbe J., 2003a. Processing of aluminium alloys by equal channel angular drawing at room temperature. Journal of Materials Processing Technology 143, 105-111.

Perez C.J.L., Gonzalez P., Garces Y., 2003b. Equal channel angular extrusion in a commercial Al-Mn alloy. Journal of Materials Processing Technology 143, 506-511.

Perez-Foguet A., Rodriguez-Ferran A., Huerta A., 2003. Efficient and accurate approach for powder compaction problems. Computational Mechanics 30 (3), 220-234.

Prangnell P.B., Harris C., Roberts S.M., 1997. Finite element modelling of equal channel angular extrusion. Scripta Materialia 37 (7), 983-989.

Rajagopal K.R., Srinivasa A.R., 2005. On the nature of constraints for continua undergoing dissipative processes. Proceedings of the Royal Society a-Mathematical Physical and Engineering Sciences 461 (2061), 2785-2795.

Robertson J., Im J. T., Karaman I. , Hartwig K. T., Anderson I. E., 2003. Consolidation of amorphous copper based powder by equal channel angular extrusion. Journal of Non-Crystalline Solids 317 (1-2), 144-151.

Rosochowski A., Olejnik L., 2002. Numerical and physical modelling of plastic deformation in 2-turn equal channel angular extrusion. Journal of Materials Processing Technology 125, 309-316.

Rubinstein R., Atluri S.N., 1983. Objectivity of incremental constitutive relations over finite-time steps in computational finite deformation analyses. Computer Methods in Applied Mechanics and Engineering 36 (3), 277-290.

Segal V. M., 1995. Materials processing by simple shear. Materials Science and Engineering A 197 (2), 157-164.

Semiatin S.L., DeLo D.P., 2000. Equal channel angular extrusion of difficult-to-work alloys. Materials & Design 21 (4), 311-322.

Semiatin S.L., Delo D.P., Shell E.B., 2000. The effect of material properties and tooling design on deformation and fracture during equal channel angular extrusion. Acta Materialia 48 (8), 1841-1851.

Senkov O. N., Miracle D. B., Scott J. M., Senkova S. V., 2004. Equal channel angular extrusion compaction of semi-amorphous Al85Ni10Y2.5La2.5 alloy powder. Journal of Alloys and Compounds 365 (1-2), 126-133.

Senkov O. N., Senkova S. V., Scott J. M., Miracle D. B., 2005. Compaction of amorphous aluminum alloy powder by direct extrusion and equal channel angular extrusion. Materials Science and Engineering a-Structural Materials Properties Microstructure and Processing 393 (1-2), 12-21.

Simo J.C., Pister K.S., 1984. Remarks on rate constitutive-equations for finite deformation problems - computational implications. Computer Methods in Applied Mechanics and Engineering 46 (2), 201-215.

Smith L. M., Ganeshmurthy N., Murty P., Chen C. C., Lim T., 2004. Finite element modeling of the tubular hydroforming process - Part 1. Strain rate-independent material model assumption. Journal of Materials Processing Technology 147 (1), 121-130.

Srinivasan R., 2001. Computer simulation of the equichannel angular extrusion (ECAE) process. Scripta Materialia 44 (1), 91-96.

Stoica G.M., Liaw P.K., 2001. Progress in equal-channel angular processing. Jom-Journal of the Minerals Metals & Materials Society 53 (3), 36-40.

Stolyarov V. V., Lapovok R., 2003. Effect of back pressure on the structure and properties of Al-based alloys processed by ECAP. Thermec'2003, Pts 1-5 426 (4), 2825-2830.

Stolyarov V.V., Lapovok R., Brodova I.G., Thomson P.F., 2003. Ultrafine-grained Al-5 wt.% Fe alloy processed by ECAP with back pressure. Materials Science and Engineering a-Structural Materials Properties Microstructure and Processing 357 (1-2), 159-167.

Subramanian S.J., Sofronis P., 2002. Calculation of a constitutive potential for isostatic powder compaction. International Journal of Mechanical Sciences 44 (11), 2239-2262.

Sue H.J., Dilan H., Li C.K.Y., 1999. Simple shear plastic deformation behavior of polycarbonate plate due to the equal channel angular extrusion process. I: Finite element methods modeling. Polymer Engineering and Science 39 (12), 2505-2515.

Suh J.Y., Kim H.S., Park J.W., Chang J.Y., 2001. Finite element analysis of material flow in equal channel angular pressing. Scripta Materialia 44 (4), 677-681.

Suryanarayana C., 2001. Mechanical alloying and milling. Progress in Materials Science 46 (1-2), 1-184.

Truesdell C., Noll W., 1992. The non-linear field theories of mechanics, second ed. Springer Verlag, Berlin.

Tvergaard V., 1981. Influence of voids on shear band instabilities under plane-strain conditions. International Journal of Fracture 17 (4), 389-407.

Valiev R. Z., Langdon T. G., 2006. Developments in the use of ECAP processing for grain refinement. Reviews on Advanced Materials Science 13 (1),15-26.

Wilkinson D. S., Ashby M. F., 1975. Pressure sintering by power law creep. Acta Metallurgica 23 (11), 1277-1285.

Xia K., Wu X., 2005. Back pressure equal channel angular consolidation of pure Al particles. Scripta Materialia 53 (11), 1225-1229.

Yang Y.L., Lee S., 2003. Finite element analysis of strain conditions after equal channel angular extrusion. Journal of Materials Processing Technology 140, 583-587.

Yoon S. C., Kim H. S., 2006. Equal channel angular pressing of metallic powders for nanostructured materials. Materials Science Forum 503, 221-226.

Yun S-J., 1996. PhD Dissertation. An analysis by the finite element method of material deformation in equal channel angular extrusion. Texas A&M University, College Station.

Zapata H., 1998. Master's Thesis. Application of ECAE to consolidate Al 6061 powder. Texas A&M University, College Station.

Zhilyaev A.P., Nurislamova GV, Kim BK, Baro MD, Szpunar JA, Langdon TG. 2003. Experimental parameters influencing grain refinement and microstructural evolution during high-pressure torsion. Acta Materialia 51 (3), 753-765.

Zhou X., Tamma K.K., 2003. On the applicability and stress update formulations for corotational stress rate hypoelasticity constitutive models. Finite Elements in Analysis and Design 39(8), 783-816.

Zhu Y. T., Lowe T. C., 2000. Observations and issues on mechanisms of grain refinement during ECAP process. Materials Science and Engineering a-Structural Materials Properties Microstructure and Processing 291 (1-2), 46-53.

APPENDIX

This appendix contains the details of the coding and the algorithms used for developing the VUMAT codes for the Duva and Crow constitutive model. This appendix draws information extensively from the ABAQUS user manual (Abaqus Inc., 2004). The reader can refer to the manual for other examples of implementation of constitutive equations and further explanations and details of the interface between the VUMAT and ABAQUS.

Variables defined by the VUMAT

In this section, the variables that are used with the VUMAT subroutine are explained with the physical quantity they represent. These variables appear in the interface designed specifically for the VUMAT subroutine and are passed at each computation step. The variables that are used in the user subroutine code later are marked with a * here.

Variables defining the size of different tensors stored in the VUMAT

NBLOCK *

Number of material points in the mesh to be processed.

NDIR *

The number of diagonal components in a symmetric tensor.

NSHR *

The number of independent off diagonal components in a symmetric tensor.

NSTATEV *

Number of user-defined state variables that are associated with the material type. The user defines this number through the input file.

NFIELDV

Number of user-defined external field variables. The user defines this number through the input file.

NPROPS *

User-specified number of user-defined material properties. The user defines this number through the input file.

Variables to be updated by the VUMAT

STRESSNEW (NBLOCK, NDIR+NSHR) *

Stress tensor at each material point at the end of the increment.

STATENEW (NBLOCK, NSTATEV) *

State variables at each material point at the end of the increment. The size of this array is defined by the user in the input file associated with the VUMAT. In the VUMAT presented later, this variable is of size (nblock,1) and stores the relative density at each integration point.

Variables that can be updated by the VUMAT

ENERINTERNNEW (NBLOCK)

Internal energy per unit mass at each material point at the end of the increment.

ENERINELASNEW (NBLOCK)

Dissipated inelastic energy per unit mass at each material point at the end of the increment.

Variables passed in for information

LANNEAL

Flag indicating whether the routine is being called during an annealing process. lanneal=0 indicates that the routine is being called during a normal mechanics increment. lanneal=1 indicates that this is an annealing process and you should re-initialize the internal state variables, stateNew, if necessary.

STEPTIME

Value of time when the step began.

TOTALTIME

Value of total time. The time at the beginning of the step is given by (totalTime - stepTime).

DT *

Time increment size.

CMNAME

User-specified material name, left justified. It is passed in as an upper-case character string. Some internal material models are given names starting with the “ABQ_” character string. To avoid conflict, you should not use “ABQ_” as the leading string for cmname.

COORDMP(NBLOCK,_)

Material point coordinates. It is the midplane material point for shell elements and the centroid for beam elements.

CHARLENGTH(NBLOCK)

Characteristic element length. This is a typical length of a line across an element. For beams and trusses, it is a characteristic length along the element axis. For membranes and shells, it is a characteristic length in the reference surface. For axisymmetric elements, it is a characteristic length in the r–z plane only. For cohesive elements it is equal to the constitutive thickness.

PROPS(NPROPS) *

User-supplied material properties. The quantities like Youngs Modulus, poisons ratio, yield stresses and hardening parameters etc. can be passed through this variable.

DENSITY(NBLOCK)

Current density at the material points in the midstep configuration. This value may be inaccurate in problems where the volumetric strain increment is very small. If an accurate value of the density is required in such cases, the analysis should be run in double precision. This value of the density is not affected by mass scaling.

STRAININC (NBLOCK, NDIR+NSHR)

Strain increment tensor at each material point.

TEMPOLD(NBLOCK)

Temperatures at each material point at the beginning of the increment.

STRETCHOLD (NBLOCK, NDIR+NSHR) *

Stretch tensor, $\underset{\sim}{U}$, at each material point at the beginning of the increment defined from the polar decomposition of the deformation gradient by $\underset{\sim}{F} = \underset{\sim}{R}\underset{\sim}{U}$.

DEFGRADOLD (NBLOCK,NDIR+2NSHR) *

Deformation gradient tensor at each material point at the beginning of the increment. Stored in 3-D as [$F_{11}, F_{22}, F_{33}, F_{12}, F_{23}, F_{31}, F_{21}, F_{32}, F_{13}$]

STRETCHNEW (NBLOCK, NDIR+NSHR) *

Stretch tensor, $\underset{\sim}{U}$, at each material point at the end of the increment defined from the polar decomposition of the deformation gradient by $\underset{\sim}{F} = \underset{\sim}{R}\underset{\sim}{U}$.

DEFGRADNEW (NBLOCK,NDIR+2NSHR) *

Deformation gradient tensor at each material point at the end of the increment. Stored in vector form in 3-D as [$F_{11}, F_{22}, F_{33}, F_{12}, F_{23}, F_{31}, F_{21}, F_{32}, F_{13}$]

FIELDOLD (NBLOCK, NFIELDV)

Values of the user-defined field variables at each material point at the beginning of the increment.

STRESSOLD (NBLOCK, NDIR+NSHR) *

Stress tensor at each material point at the beginning of the increment.

STATEOLD (NBLOCK, NSTATEV) *

State variables at each material point at the beginning of the increment. In out case the size of this variable is (nblock,1)

ENERINTERNOLD (NBLOCK)

Internal energy per unit mass at each material point at the beginning of the increment.

ENERINELASOLD (NBLOCK)

Dissipated inelastic energy per unit mass at each material point at the beginning of the increment.

TEMPNEW(NBLOCK)

Temperatures at each material point at the end of the increment.

FIELDNEW (NBLOCK, NFIELDV)

Values of the user-defined field variables at each material point at the end of the increment.

Organization of the VUMAT

The VUMAT code shown here is divided into seven main sections. Each section is marked clearly in the code. The part preceding the section 1 is the standard format of the interface between the VUMAT and ABAQUS, which contains the definition of all the variables discussed earlier. In section 1, the material characteristics are obtained from the input file. The user has to make sure that the number of material properties defined in the VUMAT is equal to the material properties given by the input file.

As the VUMAT stores the information at each integration point in a vectorized format, it is necessary to convert the same information into matrix forms which will be used all through the code. For this purpose, the stress, deformation gradient and the stretch tensors are stored into 3X3 tensors, as shown in section 2.

Section 3 shows a very basic way of computing the spin tensor Ω defined by $\underset{\sim}{\Omega} = \dot{\underset{\sim}{R}}\underset{\sim}{R}^T$. This quantity is required at later stages to update the stress using the objective stress rate (Green- Naghdi stress rate) computed by the code. This computation first computes the rotation tensor $\underset{\sim}{R}$ at both the time instances and then computes $\dot{\underset{\sim}{R}}$ through a first order differentiation. Section 4 shows the computation of the symmetric part of the velocity gradient, again by a first order numerical differentiation of the deformation gradient tensor. This algorithm of updating the stress rate is computationally inefficient and better stress rate update algorithms are discussed in various works by Hughes and Winget, (1980); Rubinstein and Alturi, (1983); Simo and Pister, (1984); Flanagan and Taylor (1987) and Zhou and Tamma (2003).

Section 5 contains the calculations of the plastic velocity gradient provided by the Duva and Crow model explained in chapter II, and given by the equation (3.4). For these computations, the relative density is stored from the state variable into the variable DCRD. After this computation is done, section 6 contains the steps to compute the objective stress rate given by the equations (3.1) and (3.2). The stress increment is then computed through the equation (3.3). In section 7, the stress and the relative density are updated to their new values and returned to the respective variables provided by ABAQUS.

```
**********************************************************************
** VUMAT, FOR ABAQUS/EXPLICIT FOR DUVA AND CROW MODEL USING THE     **
** LARGE DEFORMATION FORMULATION FOR 3D ELEMENTS                    **
**                                                                  **
**********************************************************************
**********************************************************************
**
**
*USER SUBROUTINE
       SUBROUTINE VUMAT(
     1  NBLOCK, NDIR, NSHR, NSTATEV, NFIELDV, NPROPS, LANNEAL,
     2  STEPTIME, TOTALTIME, DT, CMNAME, COORDMP, CHARLENGTH,
     3  PROPS, DENSITY, STRAININC, RELSPININC,
     4  TEMPOLD, STRETCHOLD, DEFGRADOLD, FIELDOLD,
     5  STRESSOLD, STATEOLD, ENERINTERNOLD, ENERINELASOLD,
     6  TEMPNEW, STRETCHNEW, DEFGRADNEW, FIELDNEW,
     7  STRESSNEW, STATENEW, ENERINTERNNEW, ENERINELASNEW )
C
      INCLUDE 'VABA_PARAM.INC'
C
C
C     THE STATE VARIABLES ARE STORED AS:
C     STATE(*,1) = RELATIVE DENSITY
C
C
C
      DIMENSION PROPS(NPROPS), DENSITY(NBLOCK),
     1  COORDMP(NBLOCK,*),
     2  CHARLENGTH(NBLOCK), STRAININC(NBLOCK,NDIR+NSHR),
     3  RELSPININC(NBLOCK), TEMPOLD(NBLOCK),
     4  STRETCHOLD(NBLOCK,NDIR+NSHR), DEFGRADOLD(NBLOCK,NDIR+NSHR),
     5  FIELDOLD(*), STRESSOLD(NBLOCK,NDIR+NSHR),
     6  STATEOLD(NBLOCK,NSTATEV), ENERINTERNOLD(NBLOCK),
     7  ENERINELASOLD(NBLOCK), TEMPNEW(*),
     8   STRETCHNEW(NBLOCK,NDIR+NSHR),DEFGRADNEW(NBLOCK,NDIR+NSHR+NSHR),
     9  FIELDNEW(*), STRESSNEW(NBLOCK,NDIR+NSHR),
     1  STATENEW(NBLOCK,NSTATEV), ENERINTERNNEW(NBLOCK),
     2  ENERINELASNEW(NBLOCK)
C
      CHARACTER*80 CMNAME
C
      PARAMETER(M=3,N=3,ID=3,ZERO=0.,ONE=1.,TWO=2.,THREE=3.,
     1  THIRD=ONE/THREE,HALF=.5,TWOTHIRDS=TWO/THREE,THREEHALFS=1.5
     2  COEFN = 2. , EPSDOTZ = 1.D-3 , SIGMAZERO = 1.D6 )
C
C
      DIMENSION  DFGI(M,N),DFGR(M,N),XIDEN(M,N),DFGRD0(M,N),DFGRD1(M,N),
     +          VEG(M,N),TVEG(M,N),DFRT(M,N),STRET0(M,N),STRET1(M,N),
     +           STR(M,N),STRR(M,N),DSTR(M,N),STRETI0(M,N),STRETI1(M,N),
     +          SPINW(M,N),WS(M,N),SW(M,N),XROT0(M,N),XROT1(M,N),
     +          XRDOT(M,N),XROT0TR(M,N),XOMEGA(M,N),DCD(M,N),DEL(M,N)
C
C
```

```
C-----------------------------------------------------------------------
C
C----SECTION I
C
C
C    OBTAIN THE MATERIAL PROPERTIES E AND NUE FROM THE INPUT FILE
C
      E      = PROPS(1)
      XNUE   = PROPS(2)
C
C    DEFINE THE LAMES CONSTANTS
C
      EBULK3 = E/(ONE-TWO*XNUE)
      EG     = E/(ONE+XNUE)
      ELAM   = (EBULK3-EG)/THREE
C
C-----------------------------------------------------------------------
C
C    START THE MATERIAL CONSTITUTIVE EQUATIONS AT EACH INTEGRATION
C    POINT
C
      D0 100 KM = 1,NBLOCK
C
C
C
C-----------------------------------------------------------------------
C
C----SECTION II
C
C
C    WRITE STRESSES FROM PREVIOUS TIME STEP IN TO ARRAY STR
C
      DO K=1,3
      STR(K,K) = STRESSOLD(KM,K)
      END DO
      STR(1,2) = STRESSOLD(KM,4)
      STR(2,1) = STRESSOLD(KM,4)
      IF(NTENS.GT.4)THEN
      STR(2,3) = STRESSOLD(KM,5)
      STR(3,2) = STRESSOLD(KM,5)
      STR(1,3) = STRESSOLD(KM,6)
      STR(3,1) = STRESSOLD(KM,6)
      END IF
C
C     DEFINE IDENTITY MATRIX
C
      DO 50 I=1,M
      DO 50 J=1,N
        IF(I .EQ. J) THEN
          XIDEN(I,J)=1.0D0
        ELSE
          XIDEN(I,J)=0.0D0
        END IF
50    CONTINUE
```

```
C
C
C     CALCULATE DEVIATORIC STRESS (DSTR) AND MEAN STRESS (1/3)*TR(SIGMA)
C
      CALL KDEVIA(STR,XIDEN,DSTR,MSTR)
C
C     CALCULATE EFFECTIVE STRESS AS SQRT((3/2)*DSTR:DSTR)
C
      CALL KEFFP(DSTR,EFFSTR)
C
C
C-----------------------------------------------------------------------
C
C     STORE THE DEFROMATION GRADIENT AND THE STRETCH TENSORS
C
C     WRITE THE DEFORMATION GRADIENT TENSOR AT PREVIOUS TIME STEP
C     INTO DFGRAD0
C
      DO K=1,3
      DFGRD0(K,K) = DEFGRADOLD(KM,K)
      END DO
      DFGRD0(1,2) = DEFGRADOLD(KM,4)
      DFGRD0(2,1) = DEFGRADOLD(KM,7)
      DFGRD0(2,3) = DEFGRADOLD(KM,5)
      DFGRD0(3,2) = DEFGRADOLD(KM,8)
      DFGRD0(1,3) = DEFGRADOLD(KM,6)
      DFGRD0(3,1) = DEFGRADOLD(KM,9)
C
C     WRITE THE DEFORMATION GRADIENT TENSOR AT NEXT TIME STEP
C     INTO DFGRAD1
C
      DO K=1,3
      DFGRD1(K,K) = DEFGRADNEW(KM,K)
      END DO
      DFGRD1(1,2) = DEFGRADNEW(KM,4)
      DFGRD1(2,1) = DEFGRADNEW(KM,7)
      DFGRD1(2,3) = DEFGRADNEW(KM,5)
      DFGRD1(3,2) = DEFGRADNEW(KM,8)
      DFGRD1(1,3) = DEFGRADNEW(KM,6)
      DFGRD1(3,1) = DEFGRADNEW(KM,9)
C
C
C     WRITE THE STRETCH TENSOR "U" DEFINED BY F=R*U AT PREVIOUS TIME
C     STEP INTO STRET0
C
      DO K=1,3
      STRET0(K,K) = STRETCHOLD(KM,K)
      END DO
      STRET0(1,2) = STRETCHOLD(KM,4)
      STRET0(2,1) = STRETCHOLD(KM,4)
      STRET0(2,3) = STRETCHOLD(KM,5)
      STRET0(3,2) = STRETCHOLD(KM,5)
      STRET0(1,3) = STRETCHOLD(KM,6)
      STRET0(3,1) = STRETCHOLD(KM,6)
```

```
C
C     WRITE THE STRETCH TENSOR "U" DEFINED BY F=R*U AT NEXT TIME STEP
C     INTO STRET1
C
      DO K=1,3
      STRET1(K,K) = STRETCHNEW(KM,K)
      END DO
      STRET1(1,2) = STRETCHNEW(KM,4)
      STRET1(2,1) = STRETCHNEW(KM,4)
      STRET1(2,3) = STRETCHNEW(KM,5)
      STRET1(3,2) = STRETCHNEW(KM,5)
      STRET1(1,3) = STRETCHNEW(KM,6)
      STRET1(3,1) = STRETCHNEW(KM,6)
C
C
C---------------------------------------------------------------------
C
C-----SECTION III
C
C     STEPS TO CALCULATE THE OMAGA TENSOR OMEGA = R_DOT*R_TRANSPOSE
C
C
C     TO DETERMINE THE "R" FROM THE POLAR DECOMPOSITION OF F=RU
C
C     FIRST DETERMINE THE INVERSE OF STRETCH TENSOR "U" AT BOTH TIME
C     INSTANCES
C
      CALL KINVER(STRET0,STRETI0)
      CALL KINVER(STRET1,STRETI1)
C
C     CALCULATE "R" AT BOTH THE TIME INSTANCES AS XROT0 AND XROT1
C
      CALL KMLT(DFGRD0,STRETI0,XROT0)
      CALL KMLT(DFGRD1,STRETI1,XROT1)
C
C
C     DETERMINE RDOT
C
      IF(DTIME.GT.0.) THEN
      DO 99 I=1,M
      DO 99 J=1,N
        XRDOT(I,J)=(XROT1(I,J)-XROT0(I,J))/DT
99    CONTINUE
      END IF
C
C
C     CALCULATE R_TRANSPOSE
C
      CALL KTRANS(XROT0,XROT0TR)
C
C
C     CALCULATE OMEGA = R_DOT*R_TRANSPOSE
C
      CALL KMLT(XRDOT,XROT0TR,XOMEGA)
```

```
C
C
C-----------------------------------------------------------------------
C
C----SECTION IV
C
C
C    STEPS TO DETERMINE THE SYMMETRIC PART OF VELOCITY GRADIENT
C
C
C    DETERMINE DEFORMATION GRADIENT RATE F_DOT
C
      IF(DTIME.GT.0.) THEN
      DO 110 I=1,M
      DO 110 J=1,N
        DFGR(I,J)=(DFGRD1(I,J)-DFGRD0(I,J))/DT
110   CONTINUE
      END IF
C
C     TO DETERMINE VELOCITY GRADIENT
C
C     FIRST DETERMINE THE INVERSE OF DEFORMATION GRADIENT
C
      CALL KINVER(DFGRD0,DFGI)
C
C     THEN CALCULATE L=FDOT*FINV
C
      CALL KMLT(DFGR,DFGI,VEG)
C
C     TO DETERMINE RATE OF DEFORMATION FROM VELOCITY GRADIENT
C
C     FIRST DETERMINE THE TRANSPOSE OF L
C
      CALL KTRANS(VEG,TVEG)
C
C
      DO 120 I=1,M
      DO 120 J=1,N
      DFRT(I,J)=(ONE/TWO)*(VEG(I,J)+TVEG(I,J))
120   CONTINUE
C
C
C-----------------------------------------------------------------------
C
C-----SECTION V
C
C
C     STEPS TO DETERMINE THE VARIABLE DP GIVEN BY THE DUVA AND CROW
C     MODEL
C
C
C     STORE THE CURRENT RELATIVE DENSITY IN THE VARIABLE DCRD
C
      DCRD = STATEOLD(KM,1)
```

```
C
C
C     CALCULATE THE COEFFICIENTS a AND b GIVEN BY DUVA AND CROW MODEL
C
C
C
      DCA = (ONE + (TWO/THREE)*(ONE-DCRD))/(DCRD**(2*COEFN/(COEFN+1)))
C
C
      DCB = (((COEFN*(ONE-DCRD))/(ONE-(ONE-DCRD)**(ONE/COEFN))
     +      **(COEFN))**(TWO/(COEFN+ONE)))*((THREE/(TWO*COEFN))**(TWO))
C
C
C
C     CALCULATE THE EFFECTIVE STRESS DEFINED BY DUVA AND CROW MODEL
C
      PJ2 = DCA*EFFSTR**TWO + DCB*MSTR**TWO
      PJ = SQRT(PJ2)
C
C     DEFINE A GIVEN BY EPSILON_ZERO_DOT/SIGMA_ZERO^N
C
      CONSTA = EPSDOTZ/(SIGMAZERO**COEFN)
C
C     CALCULATE THE D_P GIVEN BY THE DUVA AND CROW MODEL AND STORE IN
C     THE MATRIX DCD
C
      DO I = 1,3
      DO J = 1,3
        IF(I .EQ. J) THEN
        DCD(I,J) = CONSTA*(PJ**(COEFN-1))*(THREE*DCA*DSTR(I,J)/TWO
        +          + b*MSTR/THREE)
        ELSE

        DCD(I,J) = CONSTA*(PJ**(COEFN-1))*(THREE*a*DSTR(I,J)/TWO)
        END IF
      END DO
      END DO
C
C     CALCULATE THE DILATATION = TRACE (D_P) AS DCTRVAL
C
C
      CALL KTRACE(DCD,DCTRVAL)
C
C-----------------------------------------------------------------------
C
C-----SECTION VI
C
C
C     CALCULATE THE D_E, THE OBJECTIVE STRESS RATE AND STRESS RATE
C
C
C     CALCULATE D_E = D - D_P
C
      DO 150 I = 1,3
```

```
      DO 150 J = 1,3
       DEL(I,J) = DFRT(I,J) - DCD(I,J)
150   CONTINUE
C
C     CALCULATE THE TRACE OF D_E
C
      CALL KTRACE(DEL,TRVAL)
C
C    DETERMINE GREEN-NAGHDI STRESS RATE
C
      DO 160 I=1,M
      DO 160 J=1,N
        STRR(I,J)= EG * DEL(I,J) + ELAM * TRVAL * XIDEN(I,J)
160   CONTINUE
C
C
C    DETERMINE STRESS RATE WRT UNDEFORMED CONFIGURATION
C
      CALL KMLT(XOMEGA,STR,WS)
      CALL KMLT(STR,XOMEGA,SW)
C
C
      DO 231 I=1,M
      DO 231 J=1,N
      STRR(I,J)=STRR(I,J)+WS(I,J)-SW(I,J)
C
C     .... AND  INTEGRATE
C
      STR(I,J) = STR(I,J) + STRR(I,J)*DT
231   CONTINUE
C
C
C-----------------------------------------------------------------------
C
C-----SECTION VII
C
C
C     UPDATE THE STRESS AND THE RELATIVE DENSITY
C
C
C    WRITE UPDATED STRESSES IN TO ABAQUS ARRAY STRESSNEW
C
      DO I=1,3
      STRESSNEW(KM,I)=STR(I,I)
      END DO
      STRESSNEW(KM,4)=STR(1,2)
      STRESSNEW(KM,5)=STR(1,3)
      STRESSNEW(KM,6)=STR(2,3)
C
C
C    UPDATE THE RELATIVE DENSITY
C
      DCRDDOT = -1*DCRD*DCTRVAL
      DCRD = DCRD + DCRDDOT*DT
```

```
      STATENEW(KM,1)=DCRD
C
C
100   continue
C
      RETURN
      END
C
C-----------------------------------------------------------------------
C
**
**********************************************
**           UTILITY    SUBROUTINES           *
**********************************************
************************************
**           INVERSE MATRIX          *
************************************
*USER SUBROUTINE
      SUBROUTINE KINVER(DF,A)
C
      INCLUDE 'VABA_PARAM.INC'
C
      PARAMETER (M=3,N=3)
      DIMENSION DF(M,N),A(M,N)
C
      DO 5 I=1,M
      DO 5 J=1,N
      A(I,J)=DF(I,J)
5     CONTINUE
      DO 10 K=1,M
      P=A(K,K)
      A(K,K)=1.
      DO 20 J=1,N
      A(K,J)=A(K,J)/P
20    CONTINUE
      DO 10 I=1,M
      IF(I .EQ. K) GO TO 10
      P=A(I,K)
      A(I,K)=0.
      DO 30 J=1,N
      A(I,J)=A(I,J)-A(K,J)*P
30    CONTINUE
10    CONTINUE
      RETURN
      END
**
**
************************************
**         MULTIPLY MATRIX           *
************************************
*USER SUBROUTINE
      SUBROUTINE KMLT(DM1,DM2,DM)
C
      INCLUDE 'VABA_PARAM.INC'
```

```
C
      PARAMETER (M=3,N=3)
      DIMENSION DM1(M,N),DM2(M,N),DM(M,N)
C
      DO 10 I=1,M
      DO 10 J=1,N
      X=0.0
      DO 20 K=1,M
      X=X+DM1(I,K)*DM2(K,J)
20    CONTINUE
      DM(I,J)=X
10    CONTINUE
      RETURN
      END
**
**
**************************************
**          EFFECTIVE STRESS          *
**************************************
*USER SUBROUTINE
      SUBROUTINE KEFFP(EFF1,VAL1)
C
      INCLUDE 'VABA_PARAM.INC'
C
      PARAMETER (M=3,N=3)
      DIMENSION EFF1(M,N)
C
      X=0.0
      DO 10 I=1,M
      DO 10 J=1,N
       X=X+EFF1(I,J)*EFF1(I,J)
10    CONTINUE
      IF(X .LE. 0.0) GO TO 20
      VAL1=DSQRT((3.0/2.0)*X)
20    RETURN
      END
**
**
**
**************************************
**   TRACE OF MATRIX CALCULATION      *
**************************************
*USER SUBROUTINE
      SUBROUTINE KTRACE(DE,TVAL)
C
      INCLUDE 'VABA_PARAM.INC'
C
      PARAMETER (M=3,N=3)
      DIMENSION DE(M,N)
C
      X=0.0
      DO 10 I=1,M
      DO 10 J=1,N
      IF(I .EQ. J) THEN
```

```
      X=X+DE(I,J)
      ELSE
      END IF
10    CONTINUE
      TVAL=X
      RETURN
      END
**
**
*************************************************
**   DEVIATORIC AND MEAN STRESS CALCULATION    *
*************************************************
*USER SUBROUTINE
      SUBROUTINE KDEVIA(STRSS,XIDENTY,DEVITO,X)
C
      INCLUDE 'VABA_PARAM.INC'
C
      PARAMETER (M=3,N=3)
      DIMENSION STRSS(M,N),XIDENTY(M,N),DEVITO(M,N)
C
      X=0.0
      DO 10 I=1,M
      DO 10 J=1,N
      IF(I .EQ. J) THEN
      X=X+STRSS(I,J)
      ELSE
      END IF
10    CONTINUE
C
      X=(1./3.)*X
C
      DO 20 I=1,M
      DO 20 J=1,N
      IF(I .EQ. J) THEN
        DEVITO(I,J)=STRSS(I,J)-(X*XIDENTY(I,J))
      ELSE
        DEVITO(I,J)=STRSS(I,J)
      END IF
20    CONTINUE
      RETURN
      END
**
**
*************************************************
** TRANSPOSE OF MATRIX                          *
*************************************************
*USER SUBROUTINE
      SUBROUTINE KTRANS(ORIGN,TRAN)
C
      INCLUDE 'VABA_PARAM.INC'
C
      PARAMETER (M=3,N=3)
      DIMENSION ORIGN(M,N),TRAN(M,N)
C
```

```
      DO 10 I=1,M
      DO 10 J=1,N
      TRAN(J,I)=ORIGN(I,J)
10    CONTINUE
      RETURN
      END
**
**
**
```

VITA

Name:	Anshul Kaushik
Address:	8-9-65, Dhatunagar Midhani Enclave, Kanchanbagh Hyderabad Andhra Pradesh – 500058, India.
Date of birth:	Aug. 28, 1980.

Education:

2005-2007	Texas A&M University Doctor of Philosophy Mechanical Engineering, 2007
2002-2004	Texas A&M University Master of Science Mechanical Engineering, 2004.
1998-2002	M.V.S.R Engineering College Osmania University Hyderabad, India. Bachelor of Engineering, Mechanical Engineering, 2002.